ВІСНИК
КИЇВСЬКОГО НАЦІОНАЛЬНОГО УНІВЕРСИТЕТУ ІМЕНІ ТАРАСА ШЕВЧЕНКА

ISSN 1728-2306

РАДІОФІЗИКА ТА ЕЛЕКТРОНІКА 18/2012

Засновано 1999 року

УДК 517

Публікуються результати експериментальних та теоретичних досліджень у галузях фізичної електроніки, фізики плазми, фізики поверхні твердого тіла, емісійної електроніки, кріогенної та мікроелектроніки, нанофізики та наноелектроніки, високотемпературної надпровідності, квантової радіофізики, функціональної електроніки, твердотільної електроніки, мобільного зв'язку, медичної радіофізики, методів отримання діагностичної інформації та її комп'ютерної обробки.

Для науковців, викладачів вищої школи, студентів.

Experimental and theoretical contributions are published in the following fields: physical electronics, plasma physics, solid-state surface physics, emission electronics, cryogenic electronics, microelectronics, nanophysics and nanoelectronics, high-temperature supercondactive electronics, solid-state electronics, functional electronics, microwave electronics, quantum electronics, mobile communication, medical radiophysics, methods of receipt and computer processing of diagnosis information

Designed for researches, university teachers, students.

ЗМІСТ

CONTENTS

UDC 615.849

L. Aslamova, Ph.D., N. Melenevska, Ph.D.,
N. Miroshnichenko, Ph.D., E. Grabovska, Ph.D.

THE POSSIBILITIES TO AVOID ANTI-SCATTER GRID USAGE IN X-RAY DIAGNOSTIC PROCEDURES

У роботі запропоновано зменшення дозового навантаження на пацієнтів та одержання високоякісних знімків під час обстеження органів грудної клітини шляхом оптимального поєднання цифрового приймача рентгенівських зображень та їх цифрової обробки.

Ключові слова: цифровий приймач рентгенівського зображення, пацієнт, дозове навантаження.

This article studies high-quality images and reduction of x-ray dose on patient undergoing chest screening due to optimal combination of digital receiver and its further software processing.

Keywords: digital receiver, x-ray imaging, patient, dose reduction.

Abstract. Chest screening is the most frequent procedure not only in Ukraine (more than half of all x-ray examinations), but also in many other countries. It provides the most significant contribution to general exposure dose for ukrainian population. It is exceed 40% among all types of technological irradiation [8]. On one hand, chest organs (CO) examination is the most effective early diagnosis of tuberculosis, lung cancer and other diseases. On the other, dose exposure for chest screening is in few times higher than the international practice. Therefore, the analysis of international experience is needed concerning this type of examination to find the optimal approach to dose reduction for Ukrainian population. Examination conditions are limited by different parameters, in particular, by the diagnostic dose referent levels. Dose referent levels defined for entrance surface dose (ESD) delivered to a chest, according to NRPB (National Radiological Protection Board), are equal to 0,3 mGy [9,10]. In Ukraine this indicator is a little higher [11]. EC Commission recommends the range of tube potential for radiographic examination from 100 to 150 kVp with the use of anti-scatter grid and camera for automatic exposure control [4]. Such parameter values determine requirements that must be followed during CO examinations.

To obtain good diagnostic results in large patients undergoing CO examination the image contrast should be increased. In traditional medical practice it is usually provided with anti-scatter grid. The following experiments concerning the use of grids are known. For example, x-ray laboratory of Polytechnic university of Hon Kong used film x-ray device Toshiba with moving anti-scatter grid for their studies [1]. Measurements were performed using anthropometric phantom. Radiodiagnosis of chest was carried out at low voltage on tube (70 kVp), in standard posteroanterior projection without anti-scatter grid. The same procedures were done with application of high voltage potential technique on tube (120 kVp), with the use of moving anti-scatter grid ratio 12:1. Herewith, focus-source distance equals to 180 sm. Averaged experiments results showed that entrance surface dose at low voltage on tube (70kVp) without anti-scatter grid was in 1,7 times smaller than at 120 kVp with anti-scatter grid. Thus, the application of tube high voltage potential technique (with use of anti-scatter grid) improves image contrast of an object at slide, but at the same time it increases entrance surface dose (ESD) and effective dose in Bucky factor of 1.7 times.

The optimization of image Dose-Quality characteristics were researched in clinic experiments where the possibility of air gap instead of anti-scatter grid using was studied [6]. In these experiments film-screen x-ray device TUR D800-3 (VEB Hermann Mattern, Dresden, Germany) with 12-pulse generator, moving grid ratio 7:1 and line frequency 28mm^{-1}. A distance from focus to film was 150 sm. The radiography of chest organs was performed in vertical position. Quasi-anthropomorphic phantom was used in measurements [7]. Phantom's size was approached to standard parameters of patients in posteroanterior projection of the chest. Besides these, image optimization with additional filter of 1mm Cu+1mm Al was applied. The experiment results showed the reduce of ESD by 1,8 times in case of increase of the distance between focus and film from 150 to 300 sm and antiscatter-grid replacement by air gap of 25 sm, at constant voltage on tube of 120 kVp. After increase of the voltage from 70 to 120 kVp ESD decreases in 3,9 times.

Selection of optimal parameters of anti-scatter grids is a quite effective way to improve noise-to-signal ratio. Company "Smit Röntgen" recommended the use of new grid with 15:1 ratio and 25 pl/sm [3]. Measurements were done on water phantom with thickness of 20 sm, 30 sm and 40 sm which correspond to thin, average and large patient, correspondingly. X-ray device's parameters were following: tube voltage potential of 70-110 kV and current 50-160 mAs. It was noticed that noise-to-signal ratio improved significantly (by 68%) for the phantom with thickness of 40 sm (voltage potential of 110 kV and exposure of 160 mAs) with the use of anti-scatter grid (15:1). Under the same conditions (parameters of tube current and exposition) grid ratio 15:1 gave much better improvement of noise-to-signal ratio in comparison with grid ratio 12:1, 36 pl/mm without the increase of the exposure dose.

Thereby, it can be summarized that the primary ways to find the optimal balance between image quality and radiation exposure to patient are the use of air gap instead of anti-scatter grid, or improvement of noise-to-signal ratio by selection of optimal grid parameters.

The development of Ukrainian medical diagnostics of patients in 21 century can be characterized by gradual replacement of conventional film-screen radiography by digital technologies. The digital technology provide the decrease of not only the dose delivered to patient but also reduces the price of examinations and does the diagnosis work of radiologists and doctors within clinic comfortable and adjusted. Besides, the digital processing of x-ray images evokes the most interest. Latest software for x-ray images processing allows to improve contrast of chest organs image and to decrease noise level [2,5,12]. Noise-to-signal ratio stabilization in obtained images gives an opportunity to optimize x-ray exposure modes for visual revealing of pathologies at patient chest organs images.

Methods. A study was performed to decrease of entrance surface dose during replacement of anti-scatter grid by digital image processing with special software ContextVision CVIE – Teleoptic –XR2 – ADI. The research was performed at the base of LDT "Teleoptic PRA", Kyiv, Ukraine.

A contrast of the main test-object and possibility to visually observe of additional objects were chosen as the effec-

tiveness criterion of image transformation. The test-object was aluminum disk with thickness 0,5 mm. Additional objects were analogous disks with thickness 0,2 and 0,1 mm. Also indispensable condition was obtaining an image with resolution not less then 2,5 p.l./mm. Patient chest was simulated by the water phantom. The phantom overlapped the entrance of x-ray receiver. Aluminum disks were cited in front of phantom from the side of x-ray tube. Exposure dose was measured with dosimeter (Radcal Corporation, model 2026 Radiation Monitor). Dosimeter's ionizing chamber (20X–60) was positioned in front of phantom. General experimental scheme is represented on figure 1.

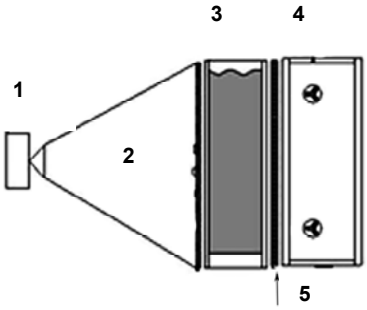

Fig.1. Experimental scheme: 1 – x-ray tube, 2 – test-object, 3 – water phantom, 4 – digital receiver of x-ray images, 5 – anti-scatter grid

The X-ray unit produced by Philips company was used in experiments. X-rays were generated by x-ray tube (Siemens Bi 125/30/52 R). Measurements were done at constant voltage on x-ray tube 81 kVp. Focus-source distance was equal to 125 sm.

Characteristics of anti-scatter grid (SOYEE 11104) were 10:1 ratio, frequency 51 p.l./sm, focus distance 120 sm. Images were obtained with digital receiver (Iona – R4000) produced by Ltd "Teleoptic PRA".

Measurements were performed in standard projection on water phantom with thickness 12, 15 sm. X-ray images were received with/without anti-scatter grid at different tube currents and exposures for each water layer.

Contrast threshold, K, was calculated by formula:

$$K = \frac{B_0 - B_b}{B_b} \cdot 100\%$$

were B_o – brightness of object on image, B_b – brightness of image's background.

Results and discussion. It is known that object identifying contrast threshold on image for a human eye is equal to 5%. Digital image processing allows to avoid using of anti-scatter grid in experiments with water phantom with thickness of 12 sm as it can be seen from items 1 an 2 in table 1. Since the grid decreases brightness and noise-to-signal ratio of image in general and does not approach to threshold contrast of 5 %. Further increase of x-ray tube current and exposition (item 3) leads to increase of ESD in 4,2 times, but do not allow get threshold contrast of test-object.

Measurements on water phantom with thickness 15 sm (see item 4,5,6) demonstrated further reduction of test-object contrast without anti-scatter grid, but sufficient improving of image quality after digital processing. The usage of anti-scatter grid increases image contrast to more than 5%, but digital processing provides much better results under the same conditions. As the same in experiments with phantom thickness of 12 sm, further increase of x-ray tube current and exposition time (see item 6) formed the higher entrance surface dose (ESD) but did not give significant improvement of test-object image.

Table 1

Measurement results of the test-object's contrast in frontal projection at U_a=81 kVp

No	*I*, (mA)	*t* (ms)	*d* (sm)	ESD (mGy)	*R* (p.l./mm)	*K* (%)	K_o (%)	Conditions	K/K_o
1	200	50	12	75,6	2,8	3,33	6,96	Water	2,09
2	200	50	12	75,6	2,8	3,43	3,79	Water and grid	1,21
3	500	80	12	319	2,8	4,30	7,86	Water and grid	1,83
4	250	63	15	125,1	2,8	2,80	7,24	Water	2,59
5	250	63	15	125	2,8	5,32	6,29	Water and grid	1,18
6	500	125	15	487	2,8	5,27	8,04	Water and grid	1,53

I – x-ray tube current, t – exposition time, d – thickness of water layer in phantom, ESD – entrance surface dose, R –resolution, K – the image contrast, Ko – the image contrast after digital processing.

Conclusion. The results of the investigation show decrease of the image contrast as the phantom thickness becomes wider. The use of anti-scatter grid leads to reduction of brightness and noise-to-signal ratio under the conditions of experiment. It is necessary to increase x-ray tube current and exposition time to achieve the threshold contras of 5%, but simultaneously this multiplies dose by Bucky coefficient (3 times).

At the same time the digital image processing allows to go beyond the image contrast of 5% in all cases. In return the processing gives an opportunity to refuse anti-scatter grid and decrease of entrance surface dose by 1,15…1,8 times.

Thereby, digital image processing is the most contemporary and successful method to refuse anti-scatter grid for chest organs examination. In return it leads to significant reduction of dose exposure on patient without increase of x-ray unit's cost. This is very important for state economy.

1. *Fung K.L., Gilboy W.B.* The effect of beam tube potential variation on gonad dose to patients during chest investigated using high sensitivity LiF:Mg,Cu,P thermoluminescent dosemeters // The British Journal of Radiology. – 2001. – 74. – P.358–367. 2. *Karimian A, Yazdami S, Askari M.A.* Reducing the absorbed dose in analogue radiography of infant chest images by improving the image quality, using image processing techniques // Radiat Prof Dosimetry. – 2011. – 147 (1-2). – P.176–179. 3. *Kok C.* / Improving digital image quality for larger patient sizes without compromises / Smit Rontgen White paper, February 2008. 4. Optimization of the radiological protection of patients undergoing radiography, fluoroscopy and computed tomography/ IAEA-TECDOC-1423/ December 2004. 5. *Prokop M., Neitzel U., Shaefer-Prokop C.* Principles of image processing in digital chest radiography // Journal of thoracic imaging, Symposium: Digital chest radiography. – 2003. – 18, No.3. – P.148–164. 6. *Vassileva J.* A phantom approach to find the optimal technical parameters for plain chest radiography // The British Journal of Radiology. – 2004. – 77. – P.648–653. 7. *Vassileva J.* A phantom for dose-image quality optimization in chest radiography // The British Journal of Radiology. – 2002. – 75. – P.837–842. 8. *Дыкан И.Н., Коваленко Ю.Н., Медведев В.Е., Мирошниченко С.И.* Основные пути снижения дозовых нагрузок при проведении рентгенологических исследований // у спец. випуску журналу "Екологічний вісник": "Антропогенно-змінене середовище України: ризики для здоров'я населення та екологічних систем" (матеріали міжнародної конференції). – К.: Чорнобиль-

інтерінформ. – 2003. – С.331–333. 9. Commission of the European Communities. Quality criteria for diagnostic images and patient exposure trial, Document XII/268/90. Brussels: CEC 1990. – 1990. 10. European commission. European guidelines on quality criteria for diagnostic radiographic images, EUR 16260 EN. Brussels: EC, – 1996. 11. Наказ від 18.07.2011р. № 295 Міністерства охорони здоров'я України. "Про створення системи контролю та обліку індивідуальних доз опромінення населення при рентгенорадіологічних процедурах". – 2011. 12. Режим доступу: www.contextvision.com.

Submitted on 22.05.12

UDC 533.9.08

A. Veklich, Ph.D.,
A. Lebid, post grad. stud.

TECHNIQUE OF ELECTRIC ARC DISCHARGE PLASMA DIAGNOSTIC: PECULIARITIES OF REGISTRATION AND TREATMENT OF SPECTRA

У роботі запропонована методика реєстрації та обробки спектрів випромінювання для діагностики плазми електродугового розряду. Методика дозволяє одночасно отримувати просторові розподіли інтенсивності випромінювання для кількох спектральних ліній. Реалізовано програмний інтерфейс користувача для обробки експериментальних даних. Запропонована методика апробована при визначенні радіальних профілів температури плазми електродугового розряду між мідними електродами. Виконано порівняння з результатами, отриманими за іншою методикою, зроблена оцінка похибки результуючої інтенсивності випромінювання, зумовленої процедурою перетворення даних.

Ключові слова: оптична емісійна спектроскопія, плазма електродугового розряду.

This article proposes technique for registration and treatment of emission spectra for diagnostic of electric discharge plasma. The technique allows to obtain the spatial profiles of emission intensity for several spectral lines simultaneously. The graphical user interface for experimental data treatment was realized. The proposed technique is approved by determination of plasma radial temperature profiles of arc discharge between copper electrodes. The results were compared with those obtained by other technique, the errors of final emission intensity due to data treatment were estimated.

Keywords: optical emission spectroscopy, plasma of electric arc discharge.

Introduction. Diagnostic of plasma is important part of numerous scientific investigations and industrial applications. The optical emission spectroscopy (OES) is the most widely used method for arc plasma diagnostic [8]. It allows to obtain such important characteristics of arc as temperature and electron density without disturbing of the object.

It is well known that plasma temperature can be obtained by absolute measurement or by comparison of relative intensities of spectral lines. Existence of local thermodynamic equilibrium (LTE) and axisymmetrical configuration of the arc are desirable in such kind of measurements.

As a rule, grating spectrometers are used for plasma diagnostic [4; 6]. But in aforementioned works the spatial distribution of emission intensity registered separately for each spectral line. It can lead to situation when parameters of the arc are changing between registrations of different spectral lines. Time dependent changing of spectral line intensities occurs in arcs between multicomponent electrodes due to irregular injection of electrode material into discharge gap. So, non-simultaneous registration of spectral lines can lead to inaccuracy results, especially in methods which are based on intensities comparison.

It is natural, that such type of inaccuracy can be avoided by simultaneous registration of several spectral lines.

Therefore, the main aim of this paper is the development of technique for simultaneous registration of spectral and spatial distribution of intensity. Additionally peculiarities of registration and treatment of spectra must be discussed, as well as the errors due to data transformations.

Peculiarities of spectra registration. Registration of spectra by light-sensitive film is out-of-date method, therefore digital camera on charge-coupled device (CCD) base was applied. In such approach the image as digital data can be properly treated by personal computer.

In Fig. 1 the proposed experimental setup on a base of grating spectrometer and digital photographic camera is shown.

Grating spectrometer consist of condenser, entrance slit, collimator, mirror and diffraction grating (see Fig. 1). The arc image on the entrance slit plane is focused by the condenser. Horizontal entrance slit cuts narrow slice of arc's image. Diffraction grating splits and diffracts collimated beams into spectra. The spectra image, which is focused by camera objective, is registered by CCD-matrix.

The spectrum is discrete in the case of arc discharge between non-cooled metallic electrodes. It is important, that in developed optical scheme every image of spectral line contains information about spatially distributed spectral brightness.

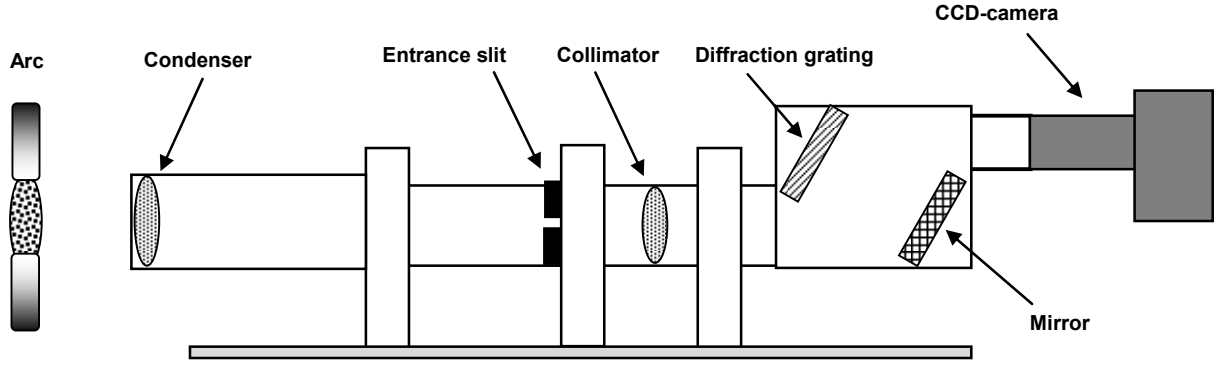

Fig. 1. Optical scheme of proposed experimental setup

In this paper the diffraction grating with 600 g/mm and the camera objective with focal length 100 mm and 4608 × 3072 pixels color CCD-matrix as well were used. The experimental setup in proposed configuration provides a reciprocal dispersion of 0.06 nm/pixel and a spatial resolution of 0.07 mm/pixel within 400 nm to 690 nm spectral range.

The color image of spectra is transformed into gray-scale for further data treatment simplifying.

The realized configuration of experimental setup permits simultaneous registration of the arc spectrum and calibration spectrum of tungsten ribbon lamp (see Fig. 2). Brightness of arc and tungsten ribbon lamp spectra must be in the same dynamic range, it can be attained by selection of exposure time.

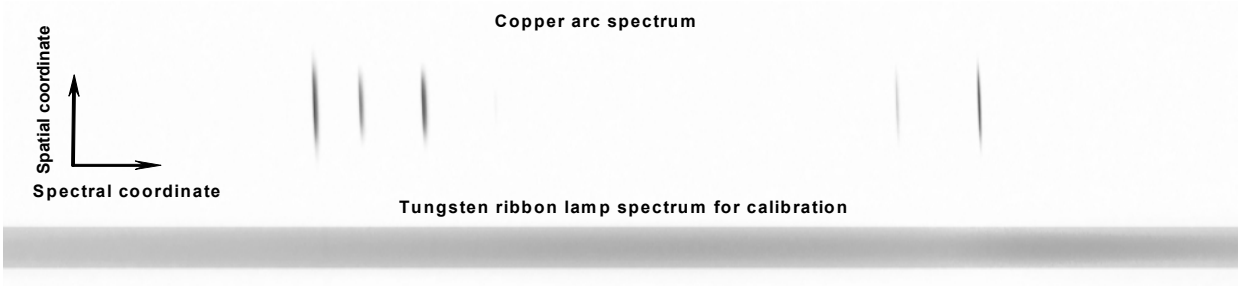

Fig. 2. Images of spectra obtained by experimental setup

Peculiarities of spectra treatment. Graphical user interface for treatment of image spectra was specially developed. The images of spectra in JPEG and BMP graphical formats are supported. The image of spectra obtained by other type of spectrometers with similar characteristics supported by the user interface as well.

The interface allows:

- interpretation of spectra;
- calibration of CCD-matrix sensitivity;
- determination of spatial intensity distribution;
- transformation of observed intensity of radiation into its local values.

The first stage of spectra interpretation is linkage of observed spectral lines positions to corresponding wavelengths. It can be carried out by using the precisely determined spectral lines or comparison spectrum as reference marks. For example CuI lines 510.5 and 515.3 nm can be used as such reference marks in investigation of electric arcs plasma with copper vapours. The realized graphical user interface includes interactive tool for such type of wavelengths linkage [5; 7].

The proposed experimental setup has small variation of reciprocal dispersion for different parts of spectral range (about 5%). The developed interactive tool for correction of the variation was included into the user interface.

Registration of continuous calibration spectrum of tungsten ribbon lamp was used for determination of CCD-matrix spectral sensitivity. Simultaneous registration of studied arc spectrum and tungsten ribbon lamp spectrum provides identical conditions of registration. The i nteractive tool for experimental setup calibration is built-in.

The spectral sensitivity of device can be given as:

$$S(\lambda) = \frac{b_{obs}(\lambda)}{b_{theor}(\lambda, T)}$$

where $b_{obs}(\lambda)$ is a spectral brightness registered by CCD, and $b_{theor}(\lambda)$ is theoretic value of spectral brightness. can be determined from Planck radiation formula:

$$b_{theor}(\lambda, T) = \frac{c_1}{\lambda^5}\left(\exp\left[\frac{c_2}{\lambda T}\right] - 1\right)^{-1}$$

where c_1 and c_2 are constants, λ is wavelengths, T is temperature of blackbody.

The coefficient c_1 determines the value of spectral brightness in absolute units, in the case of relative measurements it can be chosen arbitrary. The correction for greybody also can be determined by choosing of c_1. As far as $b_{obs}(\lambda)$ is measured by CCD-matrix in arbitrary units from 0 to 255, it is reasonable to fit $b_{theor}(\lambda, T)$ to comparable values by c_1 coefficient. The spectral sensitivity was normalized to one in its maximum by c_1 coefficient (see Fig. 3).

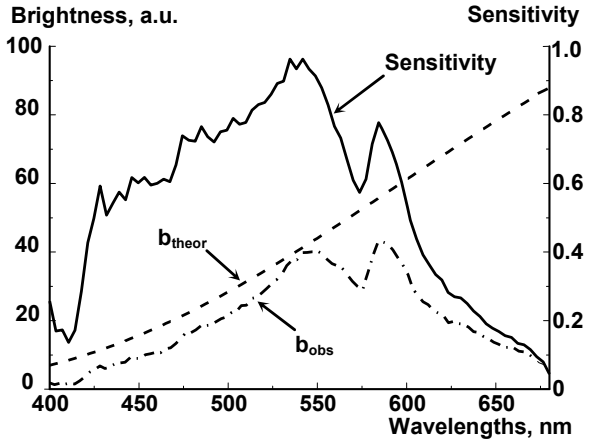

Fig. 3. Observed (b_{obs}) and theoretical (b_{theor}) brightness of tungsten ribbon lamp spectrum and spectral sensitivity of experimental setup

Due to noisy character of experimental data, the sensitivity was smoothed by method of sliding average.

Every image of spectral line contains information about spatially distributed spectral brightness $b_{obs}(\lambda)$. The spectral intensity $I_{obs}(\lambda)$ for each spatial point in a common case can be given as:

$$I_{obs}(\lambda) = \int_{-\Delta\lambda}^{+\Delta\lambda} b_{obs}(\lambda)\, d\lambda,$$

where $-\Delta\lambda$ to $\Delta\lambda$ is a spectral range around the spectral line. But in case of digital image it possible use summation of spectral brightness instead integration:

$$I_{obs}(\lambda) = \sum_n b_{obs}(n),$$

where n is number pixels in the appropriate range from $-\Delta\lambda$ to $\Delta\lambda$. Due to noisy character of experimental data, the sensitivity was smoothed by method of sliding average.

The images of spectral line have some tilt (about 3°) in proposed spectrometer configuration. The interactive tool for compensation of the tilt was included in the user interface.

Because of registration of side-on (lateral) intensity distribution was realized in proposed experimental setup, it is necessary to use Abel inversion for obtaining of local values of intensity. The Bockasten technique for Abel transformation [3] was used. The method requires axisymmetrical configuration of the plasma source. The distance from arc axis to arc edge divides into some equal parts. Number of the parts can be optional, in this paper it is chosen as ten. Values of side-on observed intensity (curve 1) and transformed into local values (curve 2) for each point are shown in Fig. 4.

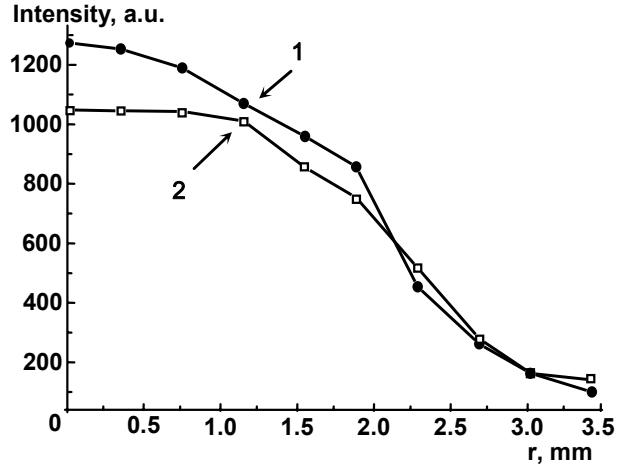

Fig. 4. Observed (1) and transformed (2) profiles CuI 521.8 line intensity

The interactive tool for Abel transformation by Bockasten technique was embedded into the graphical user interface. Some inaccuracy caused by insignificant departure of arc from axisymmetrical configuration.

Estimation of errors due to data treatment. The errors are caused by the treating of registered spectra. The operations that changed measured data are:

- smoothing of spectral sensitivity profile;
- smoothing of radial profiles of spectral brightness;
- Abel transformation.

It is reasonable to consider these errors.

Error due to smoothing of sensitivity can be estimated in assumption of slow variation of sensitivity within small spectral range (about 1 nm). So if $b_{obs}(\lambda) \approx$ const within small spectral range, the values of neighbor pixels are independent measurements of the same value. Therefore it is possible to calculate average value $\bar{S}$ and standard deviation ΔS of sensitivity near the each spectral line.

Error due to smoothing of radial profiles of spectral brightness can be estimated in followed way. As the method of sliding average was used for smoothing it can be assumed that smoothed profile is equivalent to profile of average values $\bar{I}_{obs}$. In this case the non-smoothed initial profile can be assumed as deviation from average profile. Standard deviation ΔI_{obs} caused by smoothing of radial profiles of spectral intensity can be estimated from smoothed and non-smoothed intensity profiles. The appropriate relative errors are shown as curve 1 in Fig. 5.

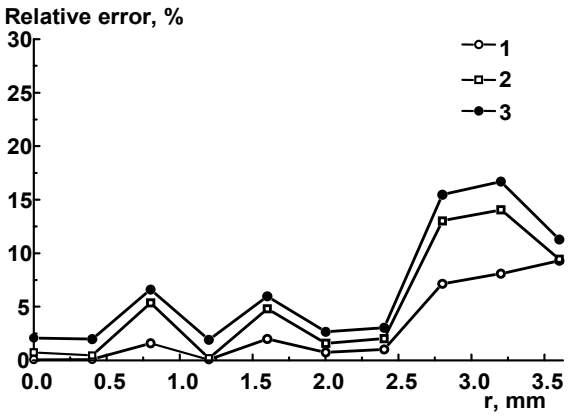

Fig. 5. Relative errors of intensity due to data treatment for CuI 521.8 line

Error of local intensity due to Abel transformation by Bockasten technique for each spectral line can be given as:

$$\Delta I_{local}(\lambda, x_j) = \Delta I_{obs}(\lambda, x_j) \cdot \sqrt{\sum_k a_{jk}^2} ,$$

where $\Delta I_{local}(\lambda, x_j)$ and $\Delta I_{obs}(\lambda, x_j)$ are standard deviations of local and observed spectral line intensity in each radial position x_j, a_{jk} is appropriate Bockasten's coefficients. The appropriate relative errors are shown as curve 2 in Fig. 5.

True local value of spectral line intensity $I_{true}(\lambda, x_j)$ can be given as:

$$I_{true}(\lambda, x_j) = \frac{I_{local}(\lambda, x_j)}{\bar{S}(\lambda)} ,$$

Thereby, standard deviation $\Delta I_{true}(\lambda, x_j)$ of true local intensity can be estimated as:

$$\Delta I_{true}(\lambda, x_j) = \left(\left(\frac{\partial I_{true}(\lambda, x_j)}{\partial I_{local}(\lambda, x_j)} \cdot \Delta I_{local}(\lambda, x_j) \right)^2 + \right.$$

$$\left. + \left(\frac{\partial I_{true}(\lambda, x_j)}{\partial S(\lambda)} \cdot \Delta S(\lambda) \right)^2 \right)^{\frac{1}{2}}$$

Or if express in explicit form:

$$\Delta I_{true}(\lambda, x_j) = \left(\left(\frac{1}{\bar{S}(\lambda)} \cdot \Delta I_{local}(\lambda, x_j) \right)^2 + \right.$$

$$\left. + \left(I_{local}(\lambda, x_j) \cdot \left(-\frac{2}{\bar{S}^2(\lambda)} \right) \cdot \Delta S(\lambda) \right)^2 \right)^{\frac{1}{2}}$$

The distribution of *total relative error due to data treatment* for CuI 521.8 nm line is shown as curve 3 in Fig. 5.

Example of temperature measurement. Obtained local values of intensity can be used for determination of radial temperature distribution by technique of the Boltzmann plot in assumption of LTE. The hypothesis of LTE was previously verified by laser absorption spectroscopy method, which is independent from LTE existence [1].

The atmospheric electric arc discharge is ignited between rod cooper electrodes. The arc current is of 3.5 A. The spectrum of plasma radiation from middle section of 8 mm discharge gap was studied.

Previously selected and examined atomic lines CuI 510.5, 515.3, 521.8 570, 578.2 nm and their spectroscopic data were used [2]. The Boltzmann plot for midpoint of discharge gap is shown in Fig. 6.

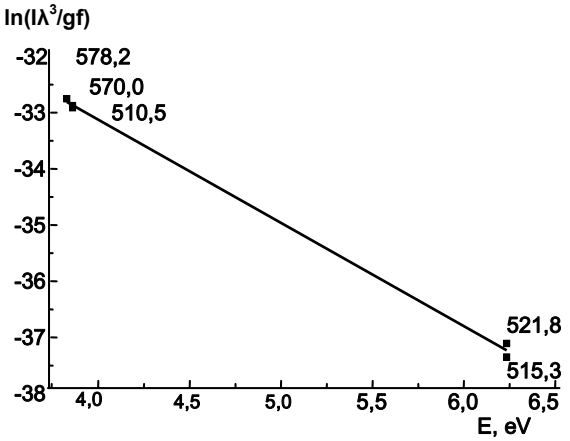

Fig. 6. Boltzmann plot for axial point of arc between copper electrodes

The obtained by such approach temperature profile is shown in Fig. 7 (see curve 1). Additional radial temperature profile (see curve 2) is plotted in Fig. 7. The last one is obtained by treating of another OES technique's [4] measurement data in a case of non-simultaneous spectral lines registration. The set of spectral lines and their spectroscopic data and conditions of experiments was the same. One can see that both profiles are in reasonable agreement.

Due to decreasing of radiation intensity in direction from arc axis to arc fringes and rising of error caused by data treatment in the same direction, the spatial scale in Fig. 7 was limited to 2 mm.

Conclusions. The diagnostic technique, namely measuring facilities and user interface for electric discharge plasma spectroscopic investigations was developed.

Uncertainty of spectral intensity caused by registration and data processing was estimated.

Developed user interface as component of proposed technique was approved by investigation of electric arc discharge between copper electrodes.

As far as results obtained by proposed technique are in a good agreement with those obtained by independent technique, therefore it reasonable to recommend the developed technique for investigation of wide range of plasma sources, particularly arc and glow discharges.

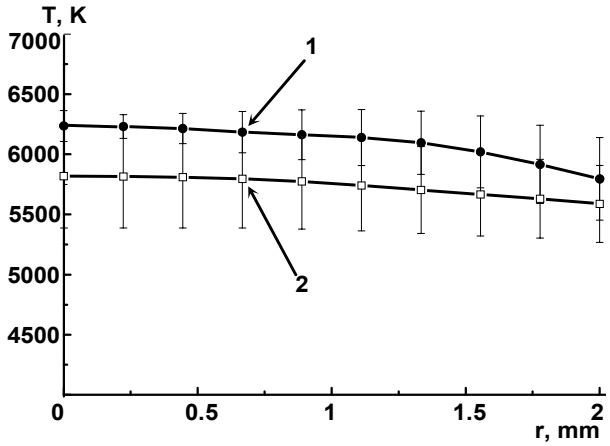

Fig. 7. Radial profile of temperature for arc between copper electrodes by different techniques

1. *Бабич И.Л., Борецкий В.Ф., Веклич А.Н., Иванисик А.И.* Спектроскопия плазмы электродугового разряда с примесями меди // Труды института проблем материаловедения им. И.Н. Францевича НАН Украины. Серия: Композиционные, слоистые и градиентные материалы и покрытия. Электрические контакты и электроды. – 2008. – С. 4–13. 2. Спектроскопія плазми електродугового розряду між композитними електродами Ag-CuO / Бабич И.Л., Борецький В.Ф., Веклич А.М. та ін. // Труды института проблем материаловедения им. И.Н. Францевича НАН Украины. Серия: Композиционные, слоистые и градиентные материалы и покрытия. Электрические контакты и электроды. – 2010. – С. 82–115. 3. *Bockasten K.* Transformation of observed radiances into radial distribution of the emission of a plasma // Journ. of Opt. Soc. of Am. – 1961. – Vol. 51, № 9 – P. 943–947. 4. *Веклич А.М., Осідач В.Є.* Методика діагностики плазми електричної дуги // Вісник Київського національного університета імені Тараса Шевченка. – 2003 – №. 5. – С. 12–14. 5. *Зайдель А.Н., Островская Г.В., Островский Г.Ю.* Техника и практика спектроскопии: – М., 1972. 6. Measurement of atomic Stark parameters of many MnI and FeI spectral lines using GMAW process / Zielinska S., Pellerin S., Dzierzega K. et.al. // J. Phys. D: Appl. Phys. – 2010. – 43, issue. 43. 7. *Lebid A.* The graphical user interface for interpretation of spectra // International interdisciplinary young scientists' conference : Proceedings, Kyiv, 2011. – K., 2011. 8. *Murphy A.* The effects of metal vapour in arc welding // J. Phys. D: Appl. Phys. – 2010. – 43, issue. 43.

Submitted on 30.03.12

UDC 53.082.5; 681.7.08

A. Goloborodko, Ph. D., V. Dan'ko, advanced engineer, N. Goloborodko, Ph. D.

DEVELOPMENT OF AUTOMATED UNIT FOR WAVEFRONT SCANNER

Розроблено та виготовлено двокоординатний скануючий пристрій для сканера хвильового фронту. Пристрій здійснює механічне переміщення діафрагми в горизонтальному та вертикальному напрямках з кроком 0,188 мм за допомогою лінійних крокових двигунів. Синхронізовано роботу сканера та CCD камери, що дозволило збільшити швидкодію побудови карти зміщень.

Ключові слова: CCD камери, сканер хвильового фронту, крокoвий двигун.

2D scanning device for wavefront scanner is designed and produced. The device provides mechanical movement of the diaphragm in horizontal and vertical directions with a step of 0.188 mm by means of linear stepping motors. The procedure of synchronization of 2D scanning device with CCD camera allows increasing the time of local slopes mapping.

Key words: CCD photodetector, wavefront scanner, stepping motor.

Introduction. Non-destructive diagnostic of surface became actual problem in modern metrology [9, 3]. It finds practical use for the control of surface substrates in the electronics industry, determining the aberrations of components of optical systems, determining deformations and stresses of mechanical structures. The most effective for such kind of investigations is the direct measuring of the wavefront by sensors that are widely used in adaptive optics [1]. It allows not only the direct measuring of the wavefront but also its adjusting in real time. However sensors do not determine the wavefront directly, usually they measure gradient of wavefront (i.e. the local slope) or wavefront second derivative (i.e. curvature). Among the wavefront sensors the Shack-Hartmann sensor should be mentioned as the most used. The principle of its work is well known [6]. A significant obstacle for the application of a Shack–Hartmann sensor to the precision monitoring of surfaces is a contradiction between its sensitivity and the spatial resolution. As a rule, the spatial resolution is defined by the dimensions of microlenses in the lenslet array. A reduction

of lenslets diameter results, in practice, in a reduction of their focal length; hence, it influences the accuracy of the wavefront reconstruction; namely, the accuracy decreases.

It is proposed to use wavefront scanner [5; 8], which consists of a high-quality lens, in the focal plane of which a CCD photodetector is placed. The separation of the investigated wavefront on the subapertures is realized by movable diaphragm. The diaphragm can be created using the LCD spatial light modulator, which provides wide possibilities to control its size and position [10]. In addition, an ordinary diaphragm of necessary size that mechanically moves within the investigated aperture can be used [8].

Certainly another modification of the scanner can be used for the characterization of optical elements, the modification, in which investigated elements are sequentially scanned by thin beam (ray-tracing method [7]), but this method is not considered in current paper.

The purpose of this work is the development and production of a scanning device with improved parameters for the optical wavefront scanner and its synchronization with the CCD photodetector.

2D scanning device. Two-coordinate device with next parameters:

- scan step (*X* and *Y*) 0.188mm;
- aperture 15×15mm;
- time of 1 step moving ~10 ms;
- time of relaxation after moving ~15ms

was developed for the diaphragm moving. Fig. 1 shows the design of a scanning device.

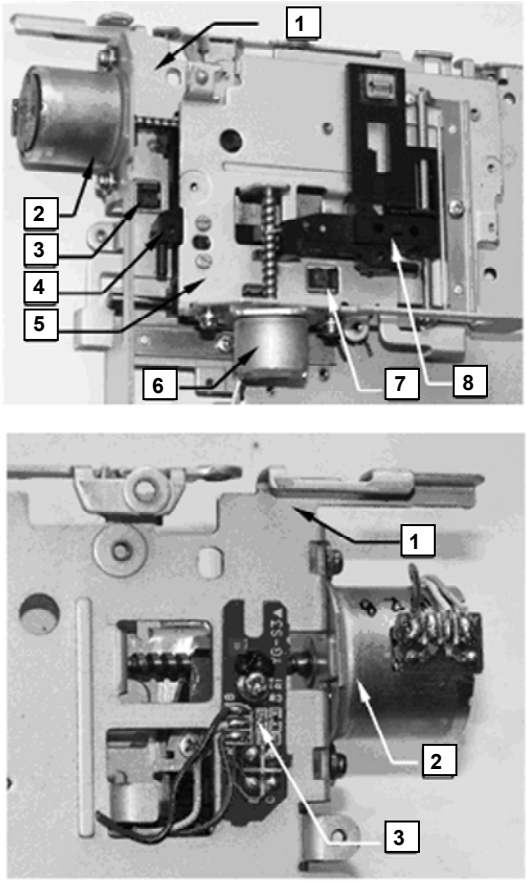

Fig.1. Photo of the two-coordinate device for the wavefront scanner aperture controlling: (a) front view, (b) rear view

It consists of two steel plates 1 and 5 on which the stepping motors 2 and 6 are mounted and with the help of spindles with screw thread they move carriages 4 and 8. The plate 1 is mounted on the experimental setup so that the moving carriage 4 could move horizontally. The 5 plate is fastened on the moving carriage 4 so that the stepping motors axes are orthogonal. Thus the moving carriage 8 can move horizontally (*X* axis) by the stepping motor 2 and can be moved vertically (*Y* axis) by the stepping motor 6. The diaphragm holder is mounted on the moving carriage 8. The carriages moving into the initial state is controlled by optoelectronic sensors 3 and 7. On the Fig.1.b one can see the method of optoelectronic sensors fixation to the steel plate.

Controller, which block diagram is shown on Fig.2, was designed to control the stepper motors of the scanning device via the parallel port of the personal computer (PC).

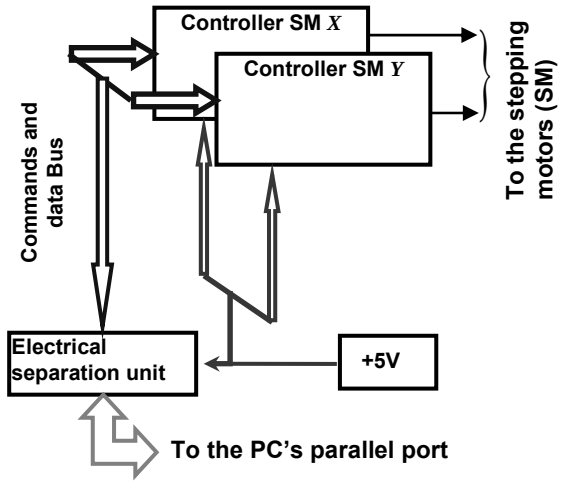

Fig.2. Block diagram of the two-coordinate device controller

The controller is made on the basis of two identical controllers of stepper motor, which are made on the basis of the integrated circuit NCL025 in a typical connection. Stepper motor controllers have a common commands and data bus, which are connected to the PC's parallel port via the node of electrical separation. Galvanic separation node isolates PC from the controllers of stepper motors and avoids damage of the PC in the case of problems in the scanning device controller.

The signals of commands and data bus are presented in Table 1.

Table 1

The signals of commands and data bus

Pin number	Signal	Description
1,3,5,…,31,33	GND	Electrical ground
12	SEL_Y\	Motor *Y* selection (controller's input: active state is low)
14	SEL_X\	Motor *X* selection (controller's input: active state is low)
18	DIR\	Direction of movement (controller's input: low signal level is for coordinate increasing)
20	STEP\/	Step (controller's input: negative pulse)
26	START	Indication of the initial position of stepper motor (output controller: opened collector)

Signals **SEL_X**, **SEL_Y** are used for "*X*" or "*Y*" motor selection, in the case of selection logical signal "0" is generated. One have to note that these signals simultaneously must not have a low signal level (logical "0").

Signal **DIR** provides direction of stepper motor moving. In the case of low signal level (logical "0") stepper motor moves in the direction from the initial position (carriage coordinate is increasing), at high level of the signal (logical "1") SM moves to the initial position (carriage coordinate is decreasing).

STEP/ signal is a negative pulse with continuance longer than 500μs. Leading front of the pulse forces SM moving along the axis *X* or *Y* (it depends on the signals **SEL_X** and **SEL_Y**), in direction, which is determined by signal **DIR**. Time between the pulses must be longer than 500 μs to avoid step skips.

Incoming signal **START** have low level (logical "0"), when one of SM moves the carriage into the initial position. It is a combination of signals that are formed by NCL025 circuits of both controllers, which are combined into logical "OR" scheme, during operation of optoelectronic sensors. The control program should analyze this signal together with signals **SEL_X\, SEL_Y** and **DIR**, to correctly identify the SM, which is in the initial position.

The final position of SM sensors are not provided in this structure, so control program have to be organized with the counters of both stepper motors.

Streams synchronization. In the construction of automated control systems a problem of control signals generating and timing parameters appears quite often. Such control signals and timing parameters could be changed during the experiment and must have very high accuracy. In particular, this problem appears in the time of constructing the SM control unit to synchronize with CCD photodetector.

There are three main methods that are used to generate control and synchronization impulses:

- circuits, which are built on the logical chips;
- circuits, which are built with integral timers;
- PC using to generate control and synchronization pulses.

The main disadvantage of the first two methods are the low flexibility of the scheme (it needs additional adaptation unit in the case of changing the experimental conditions), and constructive complexity of the electrical circuit. PC using don't have such drawbacks, but has low accuracy of the generated pulse. This is due to the fact that the response time of the interrupt is not rigidly fixed and is determined by the operating system or hardware.

Solving of this problem was made by using frame grabber internal clock generator. It allowed synchronizing the work of CCD photodetector and 2-axis scanning device simultaneously without additional circuits. Synchronization pulses, generated by such scheme, are shown on Fig. 3.

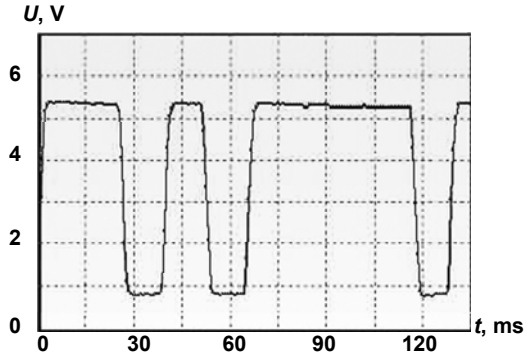

Fig.3. Oscillogram of the synchronization pulses with length of 25 ms, 15 ms and 50 ms

As one can see from the oscillogram (Fig. 3) the pulse front is less than 5ms.

Software development is made by the Borland Delphi [2] development framework with libraries ImageEn (it allows working with the clock generator of frame grabber board and video streams capture). Block diagram of the program is shown on Fig. 4.

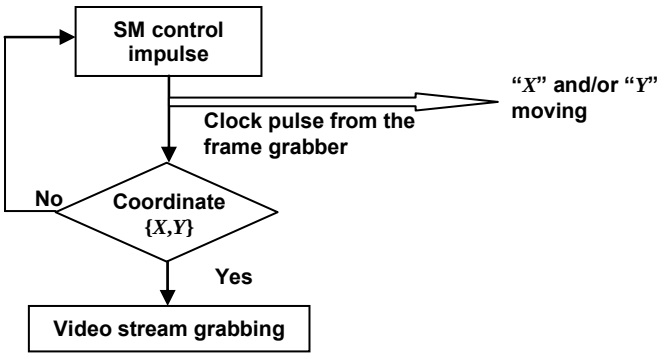

Fig.4. Block diagram of the SM and photodetector synchronization program

To provide the lowest possible delays, improve the accuracy of pulse control generation and synchronization the program basic blocks are implemented as hardware interrupt handlers with blocking re-entry parts. This procedure is repeated until PC receives stop command or new values of coordinates. After downloading the SM moving commands program checks coordinate of the carriage with internal counter. Video capture and processing starts on the command **VIDEO_START**.

Results and discussion. Verification of the wavefront scanner work was made using computer generated images with pre-known positions of the focused spot. Coordinate of the spot was calculated as resulting image center of mass [11]:

$$\langle x \rangle = \frac{\sum_{i=1}^{X_{MAX}} RGB_i x_i}{\sum_{i=1}^{X_{MAX}} RGB_i} \qquad \langle y \rangle = \frac{\sum_{i=1}^{Y_{MAX}} RGB_i y_i}{\sum_{i=1}^{Y_{MAX}} RGB_i}, \qquad (1)$$

where RGB_i is average brightness of the *i*-th row or column. The error, which was defined as the standard de-

viation of obtained coordinate from the pre-known, did not exceed 0.1 pixel.

Local slopes of the wave front, which can be measured with such scanner, can be determined by the following formula [4]:

$$\frac{\partial\phi(x,y)}{\partial x} = -\frac{\Delta x}{f} = -\frac{\langle x\rangle_{ref} - \langle x\rangle_{tes}}{f}, \qquad \frac{\partial\phi(x,y)}{\partial y} = \frac{\Delta y}{f} = \frac{\langle y\rangle_{ref} - \langle y\rangle_{tes}}{f} \qquad (2)$$

where $\phi(x, y)$ is local phase distribution on input lens and f is input lens focal length, Δx and Δy are spot shifts, which are calculated as the difference between coordinate of reference spot ($\langle x\rangle_{ref}$, $\langle y\rangle_{ref}$) and tested one ($\langle x\rangle_{tes}$, $\langle y\rangle_{tes}$).

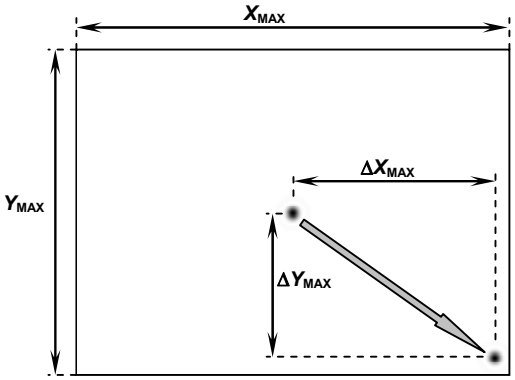

Fig.5. Maximal shift of scanner test focused spot relatively to the reference spot

Fig. 5 shows the maximal focused spot shift of the wavefront scanner for specific position of the aperture. Thus the estimated value of the maximum local slope of the phase of the wavefront (for the optical system with next parameters: input lens focal length f=200 mm, pixel width/height a=6,25 μm, image size 640×480pix) is $\partial\phi(x,y)/\partial x|_{MAX}$=0.01 for X axis and $\partial\phi(x,y)/\partial x|_{MAX}$=0.0075 for Y axis with the step $\Delta\partial\phi(x,y)/\partial x=\Delta\partial\phi(x,y)/\partial y=3.125\cdot10^{-6}$. One has to understand that angular dynamic range can be extended by adjustment of reference beam (it depends on the conditions of the experiment).

Conclusions. 2D scanning device for wavefront scanner with the following parameters was designed and produced: scan range is 15mm along the axis X and 15mm along the axis Y; minimal step of scanning is 0,188 mm. CCD camera and 2D scanning device are synchronized and wavefront angle range that can be measured by this device is evaluated. Synchronization of the CCD photodetector and 2D scanning device allow decreasing the time of defining the focused point mass center and automating the process of shifts map constructing.

1. *Alloin D. M.* Adaptive Optics for Astronomy / D. M. Alloin, J.-M. Mariotti. NATO ASI Series: Kluwer Academic Publ., 1994. – .423 p. 2. ER/Studio Data Architect / http://www.embarcadero.com/ products/er-studio-data-architect 3. *Greivenkamp J.E.* Optical testing using Shack-Hartmann wavefront sensors / J. E. Greivenkamp, D. G. Smith, R. O. Gappinger. // Proceedings SPIE. – 2001. – Vol. 4416. – P. 260–263. 4. *Kovalenko A.V.* Centroids estimation in Shack-Hartman sensor / A.V. Kovalenko, O.V. Kisil, O.V. Borkivets // Bulletin of Kiev National Taras Shevchenko University, Series: Physics & Mathematics. – 2005. – No. 3. – P. 396–402. 5. *Laude V.* Hartmann wave-front scanner. / V. Laude, S. Oliver, C. Dirson [at al.] // Optics Letters. – 1999. – Vol. 24, № 24. – P. 1796–1798. 6. *Mansuripur M.* The Shack-Hartmann Wavefront Sensor. / Optics & Photonics News. – 1999. – P 48–51. 7. *Molebny V.V.* Retina ray-tracing technique for eye-refraction mapping/ V.V. Molebny, I.G. Pallikaris, L.P. Naoumidis [et al.] // Proc SPIE. – 1997. – Vol. 2971. – P. 175–183. 8. *Podanchuk D.* Wavefront scanner for detecting surface inhomogeneities/ D. Podanchuk, V. Dan'ko, A. Goloborodko [et al.] // Bulletin of Kiev National Taras Shevchenko University, Series: Radiophysics and Electronics. – 2010. – Vol. 13. – P.24–28. 9. *Riviere J.C.* Handbook of Surface and Interface Analysis: methods for Problem–Solving. / Edited by J.C. Riviere, S. Myhra. – Marcel Dekker, Inc, New York – Basel – Hong Kong, 1998 – 997 p. 10. *Segolene O.* Liquid-crystal Hartmann wave-front scanner / O. Segolene, V. Laude, J.-P. Huignard // Applied Optics .– 2000. – Vol. 39, No. 22. – P. 3838–3845. 11. *Sutyagina N. S.* Two-channeled wavefront scanner for determining surface features. / N. S. Sutyagina, M. M. Kotov, V. A. Nikirin // Bulletin of Kiev National Taras Shevchenko University, Series: Physics & Mathematics. – 2009 – No. 2. – P. 200–203.

Submitted on 10.09.12

UDC 535.5:621.029.7

V. Grygoruk, Dr. Sci., Y. Onysko, pr. eng., Y. Slinchenko, Ph. D.

THE MODE COMPOSITION AND FIELD DISTRIBUTION INSIDE AND OUTSIDE OF THE SILICA-BASED SUB–WAVELENGTH FIBERS WITH AN AIR OPTICAL CLADDING

З аналізу результатів числового розв'язку відповідних характеристичних рівнянь для кварцового волокна з повітряною оболонкою на довжині хвилі 0,63 мкм отримано значення сталих поширення мод для діаметрів волокна до 2,5 мкм. Також було визначено просторовий розподіл інтенсивності оптичного поля у поперечному перерізі цих світловодів з урахуванням усіх існуючих у волокні мод. Наведено графічні розподіли отриманих залежностей. Встановлено наявність значного зовнішнього еванесцентного поля.

Ключові слова: оптичне волокно, спеціальні волоконні світловоди, субхвильові світловоди.

From the analysis of the numerical solution results of the corresponding characteristic equations for the quartz fiber with an air cover at the wavelength of 0.63 μm it has been obtained the values of the modes propagation constants for the fiber diameters up to 2.5 μm. It was also determined the spatial distribution of the optical field intensity in the cross section of these light guides including all of the fiber modes in it. It has shown the graphical distributions of the obtained dependencies. The significant external evanescent field is present.

Keywords: optical fiber, special fibers, sub-wavelength fibers.

Introduction. The substantial progress in the fiber optics resulted to arise a new trend with development of special fiber light guides (SFLG). The ability to get light guides with required physical parameters detected its wide using as in the fundamental researches so in the practical applications. Last time through the development of the near field optics the considerable scientific and applied interest is paid to such varieties SFLG as sub-wavelength fiber light guides (SWFLG). So pressing issue is the need to study the fields' distribution of specific types SWFLG.

The work purpose is to identify and analyze the mode structures and the field distributions inside and outside of the sub-wavelength quartz fibers with an air cover for the optical wavelength of 0.63 μm.

Development and discussion. To analyze the field structure near the surface SWFLG were used analytical solutions of Maxwell's equations for the step type fiber light guides (FLG) [1] and executed numerical calculations to find the waveguide parameters SWFLG and building cross-field distribution inside and outside the fiber.

Usually, in the works by SWFLG [3,4] the single-mode regime is considered or weak fiber light guides (WFLG) (where the difference of refractive indices is less than one percent). In the real conditions production SWFLG is rather difficult to ensure the exact transverse dimensions corresponding to the single-mode regime of propagation in the fiber light guides (FLG) [3]. Also, it is in doubt the possibility of applying the theory of WFLG to SWFLG where the core role plays the quartz fiber (the refractive index (RI) ~ 1,45), and cover - air (RI = 1).

Therefore, the work takes account of the actual thickness of the light guide and, accordingly, the modes fields that propagate.

The conditions were found for cutoff modes that exist in FLG with diameter d from 0 to 2,56 μm by using the implicit expression for U (V) at cutoff described in [1]. The number and types of modes that exist in SWFLG with step RI, with a specific diameter, and their value (modes) propagation constants β can be determined from the corresponding characteristic equations for HE_{vm}-, EH_{vm}-, TE_{0m}-and TM_{0m}-modes [1].

The results of numerical solution of the corresponding characteristic equations for the quartz fiber with an air cover for the wavelength of 0.63 μm: the values of modes propagation constants and their dependence on the diameter d or fiber parameter V are presented in Fig. 1 graphically.

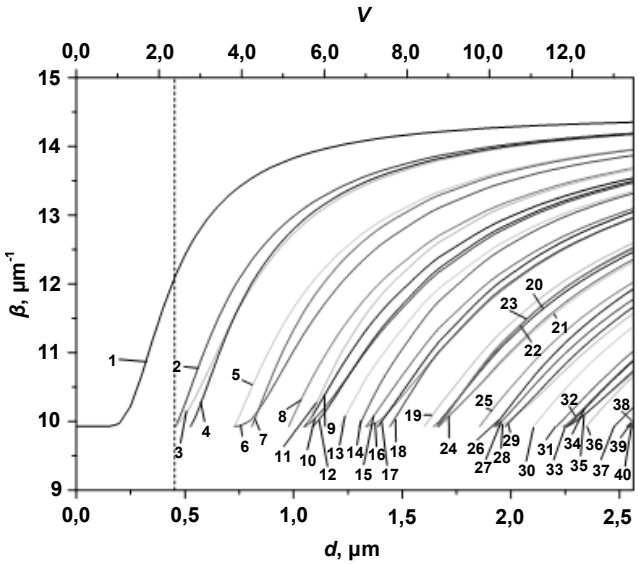

Fig.1. The values and the dependence of modes propagation constants β stepwise SWFLG (quartz-air) of diameter d or V for λ=0,63 μm. Dashed line indicates the single-mode regime - with d <0,46 μm.
The modes are denoted by numbers in order of appearance: 1 - HE_{11}, 2 - TE_{01}, 3 - TM_{01}, 4 - HE_{21}, 5 - EH_{11}, 6 - HE_{12}, 7 - HE_{31}, 8 - EH_{21}, 9 - TE_{02}, 10 - TM_{02}, 11 - HE_{41}, 12 - HE_{22}, 13 - EH_{31}, 14 - HE_{51}, 15 - EH_{12}, 16 - HE_{13}, 17 - HE_{32}, 18 - EH_{41}, 19 - EH_{22}, 20 - TE_{03}, 21 - TM_{03}, 22 - HE_{42}, 23 - EH_{51}, 24 - HE_{23}, 25 - EH_{32}, 26 - HE_{52}, 27 - EH_{13}, 28 - HE_{14}, 29 - HE_{33}, 30 - EH_{42}, 31 - EH_{23}, 32 - TE_{04}, 33 - TM_{04}, 34 - HE_{43}, 35 - HE_{24}, 36 - EH_{52}, 37 - EH_{33}, 38 - HE_{53}, 39 - EH_{14}, 40 - HE_{15}.

The spatial distribution of intensity or density of the radiation in the cross section of the SWFLG is determined by the axial component of the Umov-Pointing vector S_z [1], taking into account all of the FLG modes (Fig. 1). Graphically, in the conventional units, the distribution S_z inside and outside of the SWFLG, considering all existing modes, in particular its diameter is shown in Fig. 2.

As it is shown in Fig. 2, for almost all fiber diameters there is a significant external field (area 2), which rapidly fades to sub-wavelength distances from the surface of the light guide. There is also the dependence of the maximum value of the external evanescent field of the FLG diameter.

The optical field that propagates in FLG, that gets narrow, has a nonlinear character. This is due to smallness of the effective diameter D_{ef} of the guided mode and the significant evanescent field near the outer surface of fiber. D_{ef} - the size of the transverse intensity distribution of radiation where it is concentrated ~ 86.5% ($1/e^2$) [2,5]

$$\frac{\int_0^{D_{ef}}\int_0^{2\pi} S_{z2}a^2RdRd\phi}{\int_0^{a}\int_0^{2\pi} S_{z2}a^2RdRd\phi+\int_a^{\infty}\int_0^{2\pi} S_{z1}a^2RdRd\phi}=0{,}865,\ D_{ef}\le a;\quad \frac{\int_0^{a}\int_0^{2\pi} S_{z2}a^2RdRd\phi+\int_a^{D_{ef}}\int_0^{2\pi} S_{z1}a^2RdRd\phi}{\int_0^{a}\int_0^{2\pi} S_{z2}a^2RdRd\phi+\int_a^{\infty}\int_0^{2\pi} S_{z1}a^2RdRd\phi}=0{,}865,\ D_{ef}\ge a\,, \quad (1)$$

where S_{z1} and S_{z2} is defined in [1] for the fundamental mode.

The radiation power inside of the FLG η is

$$\eta=\frac{\int_0^{a}\int_0^{2\pi} S_{z2}a^2RdRd\phi}{\int_0^{a}\int_0^{2\pi} S_{z2}a^2RdRd\phi+\int_a^{\infty}\int_0^{2\pi} S_{z1}a^2RdRd\phi}\,. \quad (2)$$

Dependence D_{ef} and η of the diameter FLG are shown in Fig. 3 *a* and *b*, respectively. For simplicity, only the fundamental mode was taken into consideration.

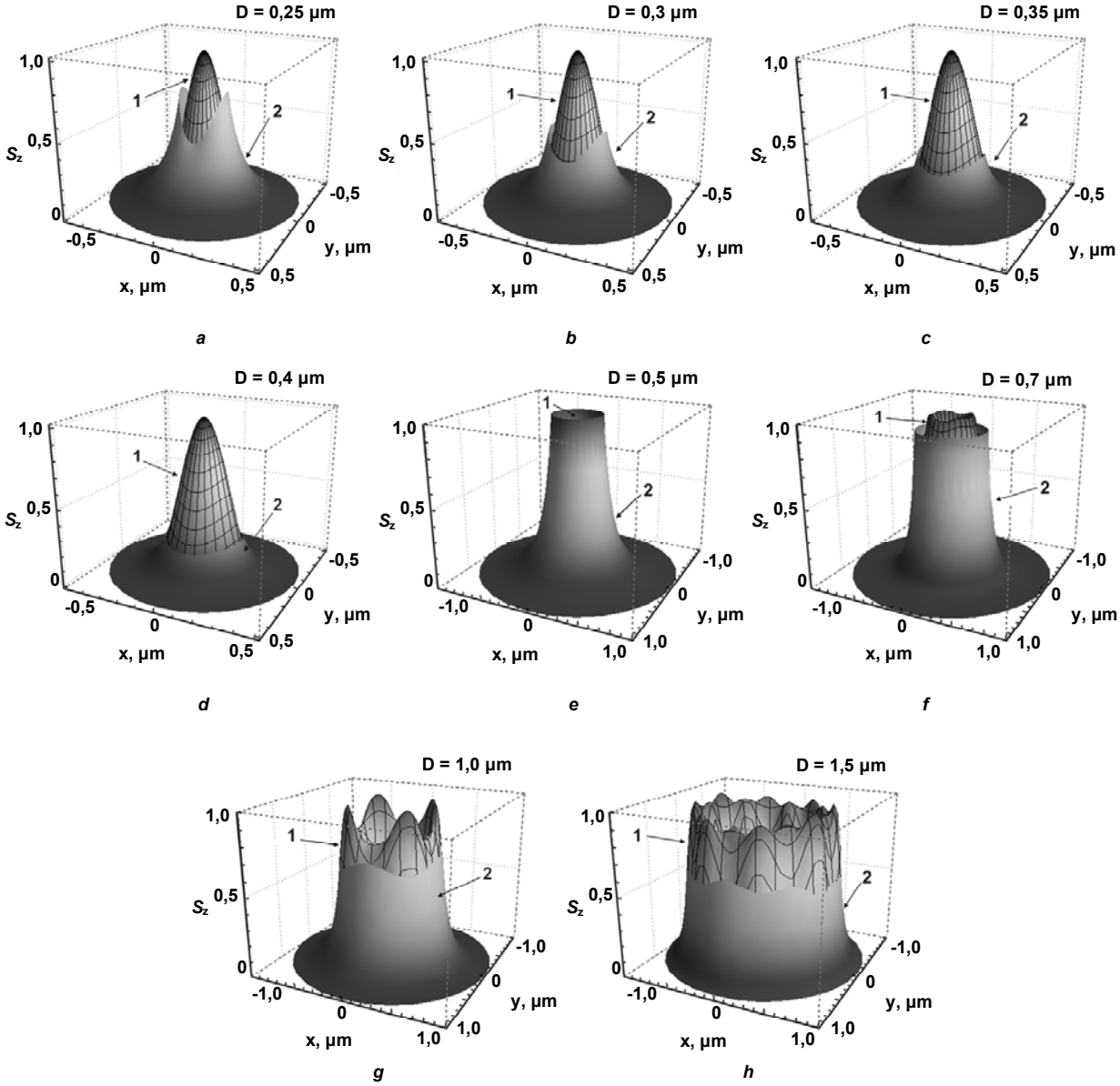

Fig. 2. The spatial distribution of axial component of the Umov-Pointing vector in the core – 1, in the cladding (outside fiber) – 2 for all modes that exist in the FLG with the diameter of: *a* – 0.25 μm, *b* – 0.3 μm, *c* – 0, 35 μm, *d* – 0.4 μm, *e* – 0.5 μm, *f* – 0.7 μm, *g* – 1.0 μm, *h* – 1.5 μm. The wavelength is 0.63 μm; the fiber core – quartz, cladding – air

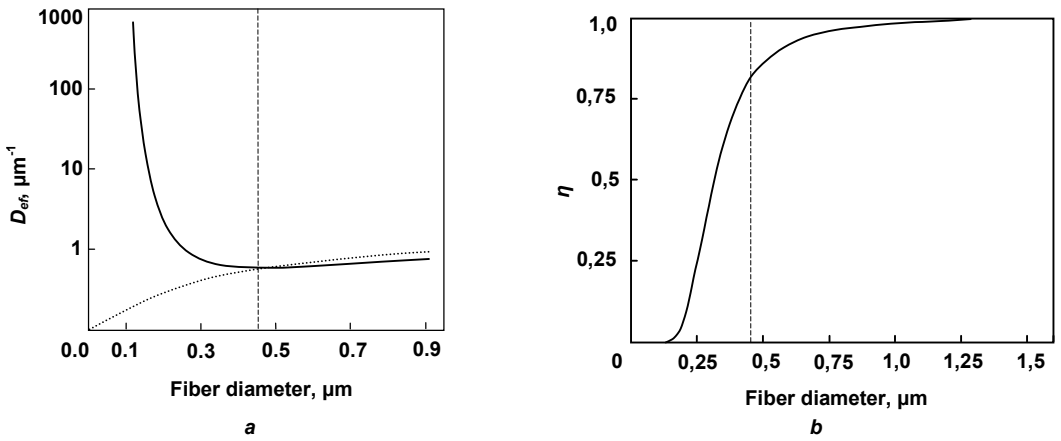

Fig. 3. *a* – depending on diameter of the FLG: by the dotted line is shown for comparison the diameter of the FLG, dashed line– single-mode regime; *b* – the power of the fundamental mode HE_{11} in the quartz fiber core (cladding – air) for the wavelength of 0,63 μm, at the fiber diameter <0,46 μm – single-mode regime (dashed line)

Conclusions. One can see that some of the guided optical power as an evanescent field extends from the outside, near the surface of the fiber. At small diameters FLG (<1 μm) D_{ef} exceeds the diameter of the FLG and therefore most of the power extends from the outside.

It should be noted that the obtained above the fields distribution for the quartz-air SWFLG can be used for qualitative analysis of fields in the FLG that adiabatic tapering, and with less accuracy, for those that quickly get narrow. In these cases, the fiber that narrowing should be introduced as a FLG with a hopping diameter. The smaller the sampling increment of the diameter, the better received fields structure will respond more exactly to existing fields in the fiber probes.

1. *Снайдер А., Лав Дж.* Теория оптических волноводов / пер. с англ. под ред. Е. М. Дианова, В. В. Шевченко. – М., 1987. 2. *Artiglia M., Coppa G., Di Vita P.* [et al.] Mode field diameter measurements in single-mode optical fibres // IEEE J. Lightwave Technol. – 1989. – Vol. 7, № 8. – P. 1139–1152. 3. *Bures J., Ghosh R.* Power density of the evanescent field in the vicinity of a tapered fiber // J. Opt.Soc. Am. A. – 1999. – Vol. 16, № 8. – P. 1992–1996. 4. *Foster M. A., Turner A. C., Lipson M., Gaeta A. L.* Nonlinear optics in photonic nanowire // Opt. Express 2008, Vol.16, N. 2, P. 1300–1320. 5. *Tong L., Lou J., Mazur E.* Single-mode guiding properties of subwavelength-diameter silica and silicon wire waveguides // Opt. Express. – 2004. – Vol. 12, № 6. – P. 1025–1035.

Submitted on 21.05.12

UDC 535. 375

M. Dyriv, post grad. stud., P. Korotkov, Dr. Sci., G. Felinskyi, Dr. Sci.

RAMAN GAIN PROFILE SIMULATION IN SINGLE-MODE FIBERS USING SPECTRAL DECOMPOSITION

Проведено моделювання профілю підсилення на основі вимушеного комбінаційного розсіювання (ВКР) у волокнах DCF і TrueWaveRS™ з багатьма коливальними модами. Використано 4 набори стандартних функцій розподілу: Гауса, Лоренца, їхнього поєднання, функції фононного осцилятора. Застосування процедури нелінійної апроксимації профілю ВКР підсилення за алгоритмом Левенберга-Марквардта дозволяє отримати розрахований ВКР спектр практично ідентичний експериментальному. Показано, що для волокна з компенсованою дисперсією (DCF) середньоквадратична похибка апроксимації реальних профілів підсилення не перевищує допустимий рівень $5\cdot10^{-3}$ для кількості гаусових спектральних компонент від 7-ми до 10-ти.

Ключові слова: нелінійна волоконна оптика, вимушене комбінаційне розсіювання, профіль підсилення.

The simulation of experimental Raman gain profile in DCF and TrueWaveRS™ fibers with multiple vibrational modes is realized. Four standard distribution function sets are used: Gaussian, Lorentzian, combination of these functions and oscillator function. Nonlinear procedure of fitting of Raman gain profile with using the Levenberg-Marquardt algorithm was applied and it gives the computed Raman spectra, which practically repeats the experimental one. It's shown that the mean-square error of real gain profile reproduction doesn't exceed the value of $5\cdot10^{-3}$ for the range of Gaussian spectral components from 7 to 10 in DCF.

Keywords: nonlinear fiber optics, stimulated Raman scattering, gain profile.

Introduction. Nowadays, the development of fiber optic telecommunication systems using the fiber Raman amplifiers (FRAs) are the most urgent task in nonlinear optics according to increasing of universal dataflow amount. The improvement of FRAs parameters is related to analysis of fundamental nonlinear characteristics of photon-phonon interaction such as Raman gain profile (RGP). Complexity of RGP arises due to the existing of a lot of overlapping spectral components. As a result, in previous years the problem of experimental RGP approximation acquired fundamental nature. The solution of this task meant realizing of accurate modeling [5]. For example, in [3] an analytic concept of RGP form with 13 Gauss and Lorentz functions in silica fiber is received. It's easy to get precision not worse than $\Delta I/I_0 = 2\cdot10^{-4}$ within 0-900 cm^{-1} using only 10 components. The optimal set of parameters for $N_m = 8$ oscillating modes within 25–750 cm^{-1} in DCF is found [1]. The spectral decomposition on 8 components in the range of 200–1400 cm^{-1} is made in fibers TeO_2–PbO–P_2O_5–Sb_2O_3 and $(100 - x)\cdot NaPO_3$–$x\cdot Nb_2O_5$, where x – is a dopant concentration, % [4].

We accent on applied character of RGP spectral decomposition in this paper. The purpose of work is the most accurate reproduction of real Raman spectrum for further calculation of FRAs parameters. Our modeling of experimental data was carried out based on the minimal set of standard distribution functions, especially 7-, 6- and 5- component analytical profiles. Obtained computation results prove the appropriateness of models with only 7 and more components because merely they give completely satisfactory fitting precision.

Problem formulation. Usually, for rough imaging of some analytical or tabular function, one can choose an approximate polynomial function with unknown coefficients. However, the question is complex profile of function and that's why polynomial fitting is not correct. The complexity of RGP, as stated above, affirms existence of many oscillating modes in the stimulated Raman scattering process. To get more quantitative information about these modes we make spectral decomposition [4].

The aim of our simulation is to research the influence of spectral component amount and type of chosen function upon the approximation accuracy. The experimental data, namely RGP in DCF and TrueWaveRS™ are taken from [1] and digitized. We used four function sets: Gaussian, Lorentz, oscillator function, which is derived from phonon oscillator equation [2] and Gauss-Lorentz superposition. For each function sets within 25–750 cm^{-1} seven components are chosen; in the case of "Gauss-Lorentz" mixture we took 4 Gauss and 3 Lorentz components. Corresponding analytical expression of described functions are following [5]:

$$g_R(\omega) = \sum_{i=1}^{N_m} A_i \exp[-\frac{(\omega - \omega_{v,i})^2}{\Gamma_i^2}, \quad (1)$$

$$g_R(\omega) = \sum_{i=1}^{N_m} A_i \frac{(\frac{\gamma_i}{2})^2}{(\omega - \omega_{v,i})^2 + (\frac{\gamma_i}{2})^2}, \quad (2)$$

$$g_R(\omega) = \sum_{i=1}^{N_m} A_i \frac{\omega\gamma_i{}^2\omega_{v,i}}{(\omega^2 - \omega_{v,i}{}^2)^2 + (\omega\gamma_i)^2}, \quad (3)$$

$$g_R(\omega) = \sum_{i=1}^{n} A_i \exp\left[-\frac{(\omega - \omega_{v,i})^2}{\Gamma_i^2}\right] + \sum_{i=1}^{k} A_i \frac{(\frac{\gamma_i}{2})^2}{(\omega - \omega_{v,i})^2 + (\frac{\gamma_i}{2})^2}, \quad (4)$$

where A_i - the i-th component amplitude; $\omega_{v,i}$ - i-th component peak frequency; Γ_i, γ_i - the half width of Gauss

and Lorentz components respectively; $N_m = 7$, $n = 4$, $k = 3$.

In papers [5;2] the measure of decomposition relevance is relative error of integral intensity, which is often used in spectroscopy. But utilization of relative error has essential shortcoming: the accuracy of approximation depends on experimental intensity value or in other words on spectrum domain and it thereafterby leads to discrepancy between accuracy and visual approaching of calculated profile to experimental one. In present article to remove this fault we use mean-square error (MSE) of intensity, which is normalized on its maximum value:

$$\delta = \sqrt{\frac{\sum_{i=1}^{p}\left(\frac{I_i}{I_{i\max}} - \frac{I_{0i}}{I_{0i\max}}\right)^2}{p}}, \qquad (5)$$

where I_i and I_{0i} are calculated and experimental intensities of RGP, p - number of approximating points.

The Levenberg-Marquardt iterative algorithm [6] is the best tool for RGP approximation in each particular fiber and it allows obtaining of the optimal spectrum distribution as like as experimental one. Though it is worth to notice that number of iterations for fitting approximation must be ≥ 1000. Moreover, the criterion of approximation usefulness is following: functions (1)–(4) are applicable for RGP spectral decomposition if their MSE is $\le 5\cdot10^{-3}$.

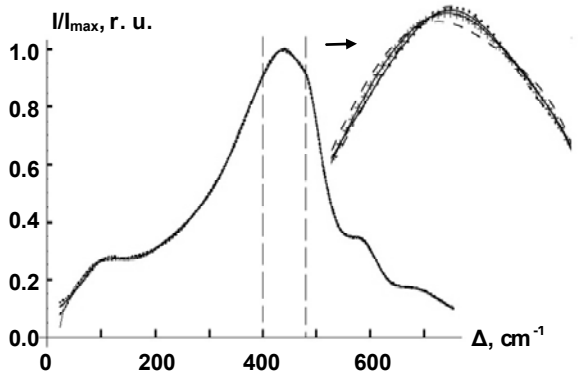

Fig. 1. Approximation of experimental RGP in DCF (——) with 7 function sets of: Gaussian(-----), Lorentz(-·-·-), Gaussian-Lorentz combination (++++), oscillator function (·····); left – the range from 24 cm^{-1} to 754 cm^{-1}; right – the range from 400 cm^{-1} to 480 cm^{-1}

Results and discussion. Graphic performance of computed models of experimental RGP in DCF is presented in Fig.1. As shown, Lorentz approximation is worse than oscillator approximation more than twice: MSEs are $9.1\cdot10^{-3}$ against $4.3\cdot10^{-3}$ respectively. Set of Gauss profiles visually is almost such as oscillator one and quantitatively its approximation error is larger a bit: $4.9\cdot10^{-3}$. Finally, as was to be expected, the mix "Gauss-Lorentz" gives the intermediate error value of $7.2\cdot10^{-3}$. Calculated profiles are also obtained for TrueWaveRS^{TM} fiber. Errors of modeling are $6.9\cdot10^{-3}$, $13.2\cdot10^{-3}$, $9.7\cdot10^{-3}$, $7.2\cdot10^{-3}$ for Gauss, Lorentz, Gauss-Lorentz and oscillator functions respectively. Such results indicate that oscillator function approximation with 7 components is the most suitable for RGP reproduction. But none of functions (1)–(4) is adequate in the case of TrueWaveRS^{TM}.

The comparison of dependences of relative errors on Gauss component number for given fibers is presented in Fig. 2. Levels of 5- and 6-component approximation MSEs locate above $5\cdot10^{-3}$ for DCF. It means the insufficiency of 5- or 6-component Gauss approximation from practical viewpoint. For TrueWaveRS^{TM} besides 5- and 6-, 7- and 8-component approximation MSEs values also are above critical line as shown in Fig. 2, in other words using of Gauss approximation with less than 9 components is vain. In our opinion, these facts are explained by the RGP shape which is more flowing in DCF than in TrueWaveRS^{TM}.

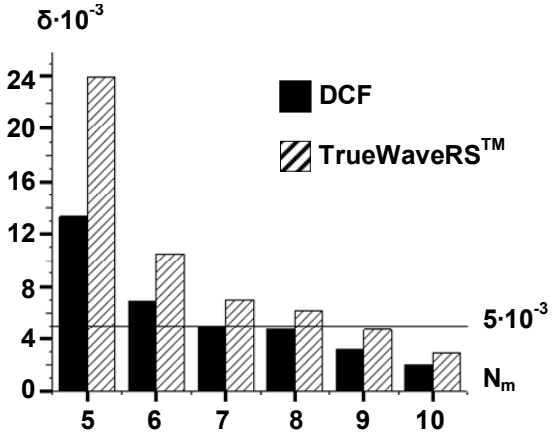

Fig. 2. Dependence of mean-square error of RGP intensity on number of Gauss components for DCF and fiber TrueWaveRS^{TM}

Superposition of 10 Gauss components gives us the best $g_R(\omega)$ approximation accuracy in fibers under investigation. In Fig. 3 Gauss 5- and 10-component RGPs in fiber TrueWaveRS^{TM} are shown within 380–520 cm^{-1}. Properly speaking in given part of spectrum one can clearly observe the difference between both of calculated profiles. Initial parameters of 5- and 10-components RGP approximation are given in Table 1.

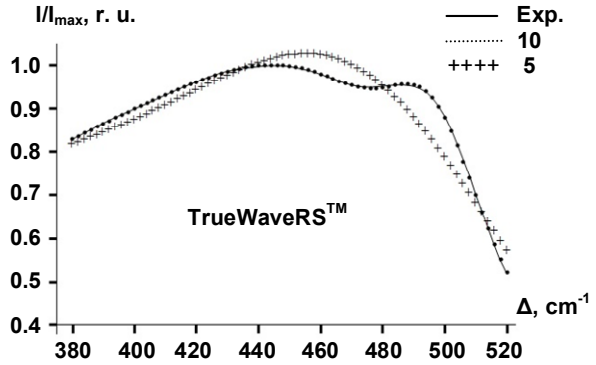

Fig. 3. Comparison of 5-component and 10-component Gauss approximation of RGP with experimental one in TrueWaveRS^{TM} in maximum amplification domain

Conclusions. As much as possible exact simulation of Raman gain profiles in fibers is preceding design phase of creating and optimization of Raman amplifiers as a part of terabit optical fiber communication lines. The method of spectral decomposition of RGP is a powerful tool for nonlinear approximation, especially:

1. This method gives numerical modeling of experimental RGP in compact analytical form. So one can optimize quantity of group delay in multiwave Raman amplifier.

2. For adequate approximation of RGP it should be used at least 7 Gauss distribution functions in dispersion compensated fiber and 9 – in fiber TrueWaveRS^{TM}.

3. Utilizing of 10 Gauss spectral component provides the smallest mean-square error: $2\cdot10^{-3}$ – in DCF, $1.9\cdot10^{-3}$ – in fiber TrueWaveRS^{TM}.

Table 1

Initial parameters of 5- and 10-components RGP approximation for TrueWaveRS^{TM}

№	5-component approximation		
	A_i	$\omega_{v,i}$,cm^{-1}	Γ_i ,cm^{-1}
1	0.274	154.8	128.44
2	0.752	384.84	125.54
3	0.532	476.31	63.86
4	0.239	600.73	34.37
5	0.123	689.56	89.24
№	10-component approximation		
	A_i	$\omega_{v,i}$,cm^{-1}	Γ_i ,cm^{-1}
1	0.083	56.22	27.86
2	0.140	95.77	43.22
3	0.165	154.05	65.82
4	0.627	422.73	87.32
5	0.443	299.40	115.69
6	0.324	472.97	53.45
7	0.213	497.02	18.07
8	0.109	583.64	54.28
9	0.108	604.42	19.22
10	0.130	611.91	228.33

1. *Bromage J.*, *Rottwitt K.* and *Lines M.E.* // IEEE Photonics Techn. Lett. – 2002. – Vol.14, №1. – P.24–26. 2. *Felinskyi G.S.* Spectroscopic multiple-vibrational-modeling of Raman gain for FRA design // Proc SPIE/Ukraine. – 2006. – Vol. 6, №1–6. – P.418–426. 3. *Hollenbeck D., Cantrell C.D.* // J. Opt. Soc. Am. – 2002. – Vol. 19, №12. – P.2886–2892. 4. *Rivero C.* High gain/broadband oxide glasses for next generation RAs: Abstract of diss. for scientific degree of Ph.D. – Univ. of Central Florida, 2005. – 142 p. 5. *Коротков П.А., Фелінський Г.С.* // Укр. Фіз. Журн. – 2009. – Т. 5, №2. – С.103–169. 6. *Ловецкий К.П., Севастьянов Л.А., Бикеев О.Н., Паукшто М.В.* Математический синтез оптических наноструктур: Учеб. пособие. – М., 2008.

Submitted on 18.09.12

UDC 535.375

A. Ivanisik, PhD, O., O. Isaienko, post grad. student

SPECTRAL DISTRIBUTION OF CHERENKOV RADIATION ENERGY AND STIMULATED RAMAN SCATTERING

У роботі запропоновано новий метод обрахунку спектрального розподілу енергії випромінювання Вавілова-Черенкова. Цей метод базується на міркуваннях, споріднених із розрахунками густини енергії випромінювання антистоксової компоненти вимушеного комбінаційного розсіювання, які потребують меншого використання математичного апарату. Отримані вирази розподілу енергії співпадають з існуючими виразами, що є додатковим доказом вірності розрахунків.

Ключові слова: випромінювання Вавілова-Черенкова, вимушене комбінаційне розсіювання, спектральний розподіл енергії випромінювання.

The new method of obtaining spectral distribution of Vavilov-Cherenkov radiation energy is proposed. This method is derived from considerations, based on obtaining energy density of stimulated Raman scattering anti-Stokes component, and in addition it requires less use of mathematical tools. The resulting expression of energy dependence is the same as the already existing one proving the method correctness.

Keywords: Vavilov-Cherenkov radiation, stimulated Raman scattering, spectral distribution of radiation energy.

Introduction. Vavilov-Cherenkov radiation is a well-studied method of charged particles detection, which in their turn are widely observed in nuclear reactions, biophysical diagnostics, astronomy etc. Mathematically this radiation is analyzed using simple geometrical considerations or complex models of radiation generation. The complex models apply fundamental considerations and provide rather detailed results, but require heavy usage of mathematical tools.

On the other hand Vavilov-Cherenkov radiation has several common features with stimulated Raman scattering (SRS), which through the past years has obtained its own mathematical approaches of energy calculation. Source of Vavilov-Cherenkov radiation is some charged particle, which moves at velocity more than speed of light in medium and causes polarization (volume density of dipole moment), which results in generation of conical radiation. When SRS is created by pulse laser beam with nanosecond duration range, its properties are influenced by non-linear effects of light propagation in medium. One of those effects is self-focusing that makes laser beam to focus at some point of medium, called focal area, where non-linear polarization of medium is induced. However, due to a change of laser pulse energy in time, this focal area moves, and at nanosecond duration of pulse it moves at velocity that is close to speed of light in the medium or even exceeds it. Observed anti-Stokes component radiation in this case is conically oriented, which is similar to Vavilov-Cherenkov radiation. As a result, source of SRS is an induced area of non-linear polarization, which moves at velocity close to speed of light in medium (and exceeds it), and creates conically oriented radiation. These common features are analyzed in more details in [2], while this paper is focused on possibilities to use mathematics

behind SRS to calculate spectral distribution of Vavilov-Cherenkov radiation energy.

Development and Discussion. Existing method is based on obtaining expressions of electrical and magnet fields of the moving particle using Maxwell's equations. After that using known field energy distribution $W \sim \int_{-\infty}^{\infty} [EH]dt$ the expression of Cherenkov radiation energy is obtained in [3] as

$$W = \frac{q^2 L}{c^2} \int_{\beta n>1} \omega \left(1 - \frac{1}{(\beta n)^2}\right) d\omega \qquad (1)$$

where q is a particle charge, L is its travel distance ($L \to \infty$ as we consider the movement of a particle along infinite path), c is a speed of light, ω is radiation frequency, β is a ratio of particle velocity to the speed of light in vacuum ($\beta = \upsilon / c$) and n is refractive index of light in medium.

However, this expression might be obtained using simpler mathematical considerations. Charge density of a single particle moving across axis z might be represented as

$$\rho = q\delta(x)\delta(y)\delta(z - t\upsilon), \qquad (2)$$

where δ is Dirac delta function. Using charge conservation law, which in our case is $\partial j / \partial z = -\partial\rho / \partial t$, we may obtain the value of the charged particle current density (along axis z):

$$j_z = -\int \frac{\partial \rho}{\partial t} dz = q\upsilon\delta(x)\delta(y)\delta(z - t\upsilon) \qquad (3)$$

On the other hand, $j_z = \partial p_z / \partial t$, where p_z is polarization. As a result

$$p_z = \int j_z dt = -q\delta(x)\delta(y)\left[U(z - t\upsilon) + const\right], \qquad (4)$$

where U is a unit step function (otherwise called Heaviside step function).

We should note that this function is found with accuracy of up to a constant. There's no polarization of a single charged particle. But to obtain it we can make an imaginary split of a particle into two particles each with half of the original charge ($q / 2$), shown on Fig. 1.

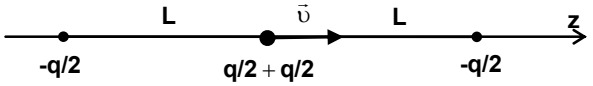

Fig. 1. Splitting of a moving charged particle into two charges at $L \to \infty$

Let's add two other charged particles with the same charge $-q/2$ at infinity distances on both sides of our moving particle. In this model the value of (4) should be proportional to $-1/2q$ behind the particle and $1/2q$ in front of it, meaning that constant should be equal to $-1/2$. However, we shall return to this issue later.

The expression of spectral-angle energy density might be taken from [1]:

$$W_{\omega\theta} = \frac{\omega^4 n}{4\pi^2 c^3} \left| \int_V d^3 r \int_{-\infty}^{+\infty} \prod \mathbf{P} \exp[i(\omega t - \mathbf{kr})] dt \right|^2, \qquad (5)$$

where r is a radius vector in a volume V, k is a wave vector of radiation, $\prod$ is a projection operator onto the plane, which is perpendicular to k, and P is a vector of polarization (in the considered model $\prod P = p_z \sin^2\theta$, where θ is an angle between axis z and the direction of radiation). The idea of (5) is based on decomposition of frequency spectrum into point sources of radiation and the following summation of secondary waves, generated by these point sources. The result of integrating (5) by time t is as follows:

$$p_{z\omega} = \int_{-\infty}^{+\infty} p_z \exp(i\omega t) dt = \frac{iq}{2\pi\omega} \exp\left(\frac{i\omega z}{\upsilon}\right). \qquad (6)$$

This is a frequency-spatial component of dipole moment. Let's return to (4). As stated above, the value of a constant should be $-1/2$. If we won't apply it and integrate (5) by t using expression (4) as is, the result would be:

$$p_{z\omega} = \int_{-\infty}^{+\infty} p_z \exp(i\omega t) dt = \frac{iq}{2\pi\omega} \exp\left(\frac{i\omega z}{\upsilon}\right) + \frac{\pi}{2}\delta(\omega). \qquad (7)$$

Summand $\frac{\pi}{2}\delta(\omega)$ is obviously redundant as we do not consider zero frequencies. So, even if we do not apply the value of a constant in (4) we shall still get the correct value by following these considerations.

Next step is integration of (5) by volume also using result (7). To do so we shall decompose vectors in (5) into components as follows:

$$kr = k_x x + k_y y + k_z z,$$

where $k_{x,y,z}$ are projections of a wave vector onto the corresponding axes (e.g. $k_z = |k| \cos\theta$). The result of integration is:

$$W_{\omega\theta} = \frac{\omega^4 n}{4\pi^2 c^3} \frac{q^2 L^2}{\omega^2} \operatorname{sinc}^2\left[\frac{L}{2}\left(k_z - \frac{\omega}{\upsilon}\right)\right] \sin^2\theta = \\ = \frac{\omega^2 q^2 L^2 n}{4\pi^2 c^3} \operatorname{sinc}^2\left[\frac{L}{2}\omega\frac{n}{c}\left(\cos\theta - \frac{1}{\beta n}\right)\right] \sin^2\theta. \qquad (8)$$

In order to obtain spectral density of energy, (8) should integrate by solid angle: $W_\omega = \int_0^\pi 2\pi \sin\theta W_{\omega\theta} d\theta$. To do this, we may introduce variable $\xi = \cos\theta$ (hence, $d\xi = -\sin\theta d\theta$) and substitute $a = (L\omega n)/(2c)$. The expression to be solved would be:

$$W_\omega = \frac{\omega^2 q^2 L^2 n}{2\pi c^3} \int_{-1}^{1} (1 - \xi^2) \operatorname{sinc}^2\left[a\left(\xi - \frac{1}{\beta n}\right)\right] d\xi. \qquad (9)$$

This expression is similar to Dirichlet integral, which has one known solution:

$$\lim_{a\to\infty} \int_{-\infty}^{\infty} f(x) \frac{a}{\pi} \operatorname{sinc}^2\left[a(x - b)\right] dx = f(b), \qquad (10)$$

where a and b are some parameters.Limits of integration can be changed to limited values, if we analyze the figure below.

In points where $|b| < m$ this solution might be used with finite limits of integration $\{-m; m\}$ ($m > 0$), otherwise the result would be 0. Based on such considerations we may use this solution to solve (10) as it also meets condition $a \to \infty$ (in our case $a = (L\omega n)/(2c)$ and $L \to \infty$). Therefore:

$$\frac{a}{\pi} \int_{-1}^{1} (1 - \xi^2) \operatorname{sinc}^2\left[a\left(\xi - \frac{1}{\beta n}\right)\right] d\xi = \left(1 - \frac{1}{(\beta n)^2}\right), \qquad (10)$$

if $1/(\beta n) < 1$ or $\beta n > 1$.

After substitution of old variables, we obtain:

$$W_\omega = \frac{\omega^2 q^2 L^2 n}{2\pi c^3} \frac{2\pi c}{L\omega n}\left(1 - \frac{1}{(\beta n)^2}\right) = \frac{\omega q^2 L}{c^2}\left(1 - \frac{1}{(\beta n)^2}\right), \qquad (11)$$

this is equal to (1).

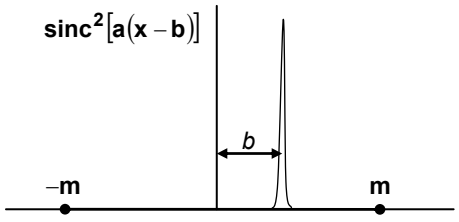

Fig. 2. Solution of a Dirichlet integral

Conclusions. Expression (11) is equal to (1) prior to integration. Results are the same though (11) is obtained using mathematical tools, originally developed for SRS analysis. It shows the correctness of provided method, and also allows us to consider similarities between Vavilov-Cherenkov radiation and stimulated Raman scattering in more detail.

Source of Vavilov-Cherenkov radiation is polarization created due to a change in location of a free charged particle moving at speed υ that is higher than speed of light in the medium. Polarization of the medium is not accounted in this case. Waves radiated by polarization on frequency ω propagate at phase speed $\upsilon_{ph}(\omega) = \omega / k$, while spectral components of polarization have phase velocity $\upsilon_{p_\omega}(\omega) = \omega / (\omega / \upsilon) = \upsilon$ on axis z, which obviously does not depend on frequency ω. As we can also see from (8), maximum energy is obtained under condition $k_z - (\omega / \upsilon) = 0$, meaning $k \cos\theta = \omega / \upsilon$ or

$$\cos\theta = \frac{\omega / k}{\upsilon} = \frac{\upsilon_{ph}(\omega)}{\upsilon}. \qquad (12)$$

The same expression for conical Vavilov-Cherenkov radiation can be also obtained using simple geometrical approach mentioned at the beginning of this paper.

Noting stated above, let us analyze stimulated Raman scattering. Source of SRS is non-linear polarization of medium that is found in focal area also called focal point.

This focal area appears due to self-focusing effect in medium. When exciting laser beam energy varies in time the focal area is created at different points in different moments of time causing it to move. When laser beam pulse has duration of nanosecond range, focal area speed can become higher than speed of light in medium. Phase velocity of radiated waves is the same as above and equals $\upsilon_{ph}(\omega) = \omega / k$. As it follows from [2], spectral components of polarization propagate at speed $\upsilon_{p_\omega}(\omega) = \omega / \upsilon_{ap} = \omega / \upsilon_{fp}$ in case of $\upsilon_{ap} = \upsilon_{fp} = \omega_a / k_{ap}$, where υ_{ap} is phase velocity of non-linear anti-Stokes polarization, k_{ap} is its wave vector, υ_{fp} is speed of focal point, ω_a is combinational anti-Stokes frequency. Radiation is directed at an angle

$$\cos\theta(\omega) = \frac{\upsilon_{ph}(\omega)}{\upsilon_{fp}}. \qquad (13)$$

It is also important to note that obtained considerations are acceptable only when polarization is dimensionally limited, meaning that only polarization from axis z can be taken into account.

As a result: mathematical tools developed for SRS analysis are applicable for Vavilov-Cherenkov radiation, radiation of both types propagates in direction that is described by equal expressions (12) and (13), and finally physical mechanism behind both types of radiation is similar.

1. *Иванисик А.И., Понежа Г.В.* Спектр антистоксового вынужденного комбинационного рассеяния из движущихся фокальных областей самофокусировки // Оптика и спектроскопия – 2001.–Т.90, №4. – С. 699–703. 2. *Іванісік А.І., Ісаєнко О.Ю., Коротков П.А., Понежа Г.В.* Випромінювання черенковського типу при антистоксовому вимушеному комбінаційному розсіюванні з рухомої фокальної області самофокусування // Вісник Київського національного університету імені Тараса Шевченка. Сер: фіз.-мат. науки. – 2011. – № 4. – С. 251–256. 3. *Франк И.М.* Излучение Вавилова-Черенкова. Вопросы теории. – М.: Наука, 1988. – С. 40–49.

Submitted on 28.05.12

UDC 546.26+539.24:621.315.59:519.17

O. Ivanyuta, Ph.D.

OPTICAL PROPERTIES OF CNTS IN BIO SYSTEMS

Комбінація молекул ДНК і вуглецевих нанотруб(CNTs) відкриває нову перспективу в агрегаті себе наноматеріалів і нанопристроїв. Схожі електронні властивості і коливальні моди CNT та системи ДНК/CNT досліджені за допомогою TEM і рамановської спектроскопії. З УФ-ІК-оптичного спектрів поглинання знайдені головні електронні групи поглинання та проаналізовані. Вплив ДНК виявлено існуванням піків 2.5–3 eV і 2 eV групи та зміщенням мінімумів в 2,96 eV, 3,05 eV, 3,34 eV. Користуючись цими результатами, ми заявляємо, що система електронних рівнів однорідно-формується в інтерфейсі ДНК/CNT.

Ключові слова: ДНК, CNT, UV-VIS-NIR спектр, рамановська спектроскопія, вольт-амперная характеристика.

The combination of DNA molecules and carbon nanotubes (CNTs) opens a new perspective in the self-assembly of nanomaterials and nanodevices. The electronic properties and vibration modes of CNT and DNA/CNT systems were investigated by TEM and Raman spectroscopy. From UV-VIS-NIR absorption spectra the principal electronic absorption bands have been evaluated. The role of the DNA is revealed by the existence of the 2.5–3 eV and 2 eV bands and shifting of the minima at 2,96 eV, 3.05 eV, 3.34 eV. Using these results we assert that system of electron levels is self-formed at the DNA/CNT interface.

Keywords: DNA, CNT, UV-VIS-NIR spectra, Raman spectroscopy, current-voltage characteristics.

Introduction. The new techniques allows scientists, for the first time, to use self-assembly techniques to develop nanoscale structures with specific dimensions and chemical properties.

Carbon nanotubes (CNT*)* have unique electrical and mechanical properties, with the potential for revolutionary applications. The grand is modifying of the ends of nanotubes and other types of nanowires with biomolecules and then using the nanotube as an electrical probe of biological interactions. The using the nanotube to interface between a single molecule and the macroscopic world, it may be possible to use electrical signals to study the behaviour of individual biomolecules [4, 5].

Problem formulation. This work aim was to study CNTs and their interaction with DNA biomolecular gel. Lengths of microcircuits reach several centimeters in many orders exceed their diameter which makes approximately 150 μm. Results of measurements *I-V* characteristics and the basic electronic parameters (specific resistance, energy of activation of a current of carry, the forbidden zone) must be measured. For the application of MWCNT in biomedical systems and to construct simple logic circuits, it is necessary to create their layers. These layers by DNA technology on *Au*, *Si* substrates you must create. For experiment I used MWCNT/(*Si* or *Au*) and MWCNT/DNA structures. Research has been focused on the application of *UV*-vis,

IR spectroscopy, *I-V* characteristics and surface microwave resonator methods to recognise and predict these molecular interactions based on primary structure and associated physic-chemical properties.

Results and discussion. The primary way is using DNA-nanotube hybrids as architectural elements, using the chemical selectivity of DNA to control the assembly of nanotubes, nanowires, and other nano-objects. That shows that area of nanotube research involves the use of biomolecules as a way of controlling the assembly of nanotubes and other nanoscale objects into larger functional structures. In the large internal space in single-walled CNT (SWCNT) results in interesting properties and applications. Medical solutions can be synthesized inside CNT [1, 5].

The method *IR*-spectrum for studying linear carbon "carbine' was used. *IR*-spectrum of passage of a sample to a range of wave numbers 300÷4000 of cm^{-1} was written down on Specord M-80 Care Zeiss Jena a spectrometer [5]. Identification of the revealed oscillatory mods in the field of 300÷2000 cm^{-1} was made on the basis of results of works [8].

Presence of connections C=C and C-C gives the basis, using article [5] to assume, that the researched carbon sample such as "carbine" consists of polymeric circuits of carbon with kymylenove type of connection. Existence C-C of connection confirms existence of spiral model of carbon circuits described in [4].

Interactions between CNT, such as bundling, broaden optical lines. While bundling strongly affects photoluminescence, it has much weaker effect on optical absorption and Raman scattering. Consequently, sample preparation for the latter two techniques is relatively simple. The spectrum is analyzed in terms of intensities of nanotube-related peaks, background and pi-carbon peak; the latter two mostly originate from non-CNT in contaminated samples (Fig. 1). However, it has been recently shown that by aggregating nearly single chirality semiconducting CNTs into closely packed Van der Waals bundles the absorption background can be attributed to free carrier transition originating from intertube charge transfer [3].

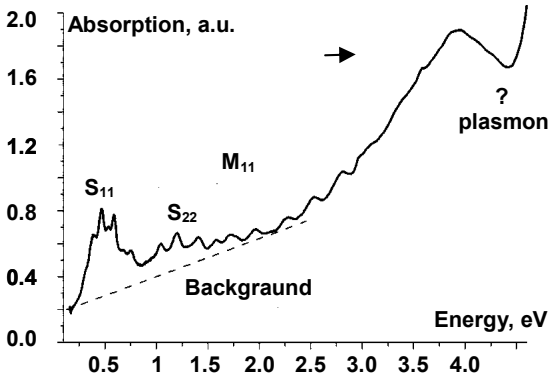

Fig. 1. Optical absorption spectrum from dispersed single-wall carbon nanotubes. [4]

Owing to their nature, SWNTs exhibit strong resonance Raman scattering due to their sharp electronic density of states. SWNTs have several unique Raman scattering features including the radial breathing mode (RBM) and tangential mode (*G*-band), which are sharp and strong peaks that can be easily distinguished from fluorescence backgrounds, and thus are suitable for optical imaging (Fig. 2). At comparison of *IR*-spectra of carbon circuits such as "carbine" with *IR*-spectra fullerenes and trubes such as "byndles" gives the basis to approve about qualitative difference of a structure of the given sample with a structural structure fullerenes and trubes. Characteristic styles of fluctuations carbon 5 and 6 nuclear ring which are compound fullerenes and tubes, it is not observed. It once again confirms an opportunity of existence of a chain structure of a chain structure of a sample [3].

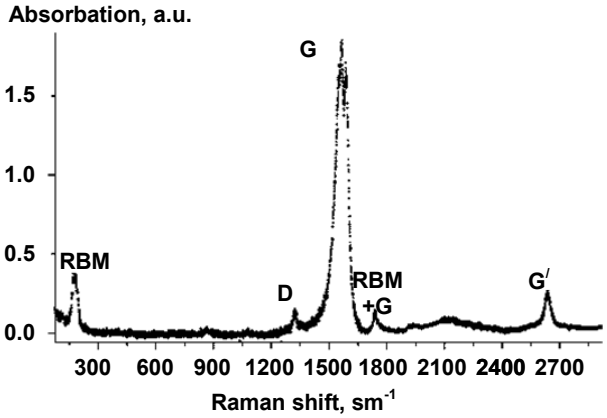

Fig. 2. Raman spectrum of single-wall carbon nanotubes [3]

The current-voltage characteristics of metal (*Pt*/*Ir*) tip - *DNA*/*MWCNT* - metal (*Pt*/*Ir*) tip have the behaviour of diode type. The value of conductivity are determined by ratio of DNA and MWCNT volumes. These results we used for obtained integrated diodes systems. Dependence of the normalized conductivity (*V*/*I*)*d*I*/d*V* versus *V* for MWCNT, MWCNT/DNA structures are calculated. *I-V* characteristics of individual carbine microstrings strings were measured in a range of temperatures of 20< T <300 K. The voltage changed in borders $\pm$ 2 *V*, a current through a sample 0,5 mA (Fig. 3.). The linear course of *I* - *V* characteristics was observed at a current up to 0,1 mA and dissymmetric a course at the greater current. It is presence of a hysteresis. The constructed dependence of the normalized conductivity (*V*/*I*)*dI/dV from V, that enables to estimate positions of local levels because of which there was a passage of carriers of a charge . Energy of activation of a current of carry was 0,4 eV. The resistance of carbine microstrings was 4 kΩ and resistivity was 25 mΩ*m.

It is necessary to note, that *I* - *V* microstrings has different character on a thermal cycle so the microstrings №1 at a stage of cooling and heating has metal type of conductivity whereas microstrings at a stage of heating shows semiconductor type of conductivity (Fig. 3).

Raman spectra was recorded in Raman spectrometer 514,5 nm line of *Ar* laser was used for the excitation. Investigation the Stokes, anti-Stokes processes, *D*- and *G*- bands by Raman spectroscopy (1000÷2000 cm^{-1}) was made. The bands are observed between 1300÷1340 cm^{-1} and 1500÷1600 cm^{-1}. Raman scattering in SWCNTs is resonant, i.e., only those tubes are probed which have one of the bandgaps equal to the exciting laser energy (Fig. 3). Those maps also contain oval-shaped features uniquely identifying (*n*, *m*) indices. [3]. The relative intensities of *D*- and G- bands depends on the type of graphitic material.

Received the Raman spectra of the MWCNT samples in the high frequency-range measured on the MWCNT/Si, MWCNT / *Au*, (MWCNT + DNA) / *Au* samples for same excitation laser powers densities and the same accumulation times. Insets of results shows that intensivity of the *G*-band does not depend on *Si* or *Au* substrate, but the intencivity of the *D*-band on the other hand shows some depends from

substrate. The additionals bands at 1094, 1216, 1777 cm^{-1} was observed on (MWCNT+DNA)/Au layers. All the above Raman modes can be observed both as Stokes and anti-Stokes scattering. As mentioned above, Raman scattering from CNTs is resonant in nature, i.e. only tubes whose band gap energy is similar to the laser energy are excited. The difference between those two energies, and thus the band gap of individual tubes, can be estimated from the intensity ratio of the Stokes/anti-Stokes lines. This estimate however relies on the temperature factor, which is often miscalculated – focused laser beam is used in the measurement, which can locally heat the nanotubes without changing the overall temperature of the studied sample [6].

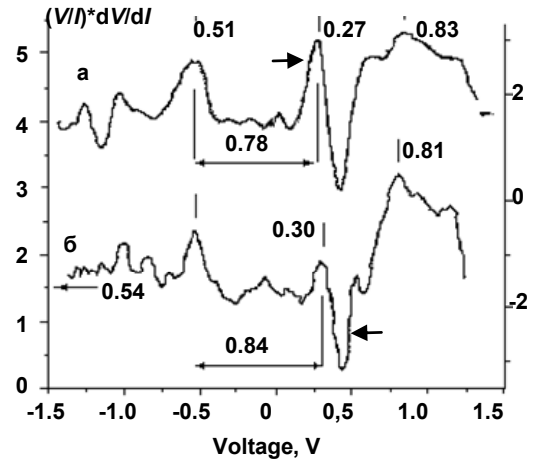

Fig. 3. Dependence of the normalized conductivity (V/I)*dI/dV versus V for MWCNT, MWCNT/DNA structures

Optical reflectance spectroscopy measurements were used for detection electron transition at MWCNT and MWCNT:DNA structures (Fig. 4.). From *UV-VIS-NIR* (300÷1000 nm) absorption spectra obtained for MWCNT and DNA/MWCNT layers the principal electronic absorption bands have been evaluated (2,95, 3,06, 3,95, 3,33, 3,38 eV), but the behaviour of absorption curve for DNA/MWCNT layer are determined by ratio of DNA and MWCNT volumes.

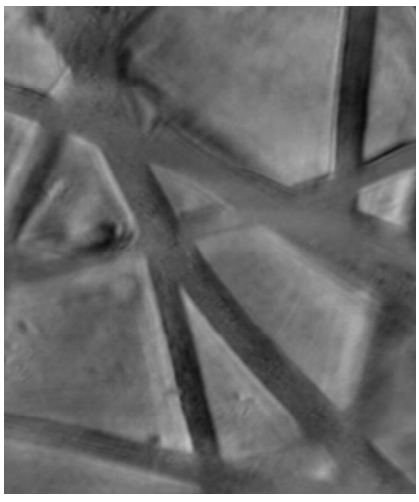

Fig. 4. The optical image of CNT microstrings

The role of the DNA porosity in the optical absorbtion at the DNA/MWCNT interface is revealed by the existence of the 2.5 - 3 eV and 2 eV bands (curves MWCNT:DNA/Au) and shifting of the minima at 2,96 eV, 3,05 eV, 3,34 eV. Existence DNA wrapped CNTs composite of connection confirms existence of spiral model of carbon circuits described in Fig. 5.

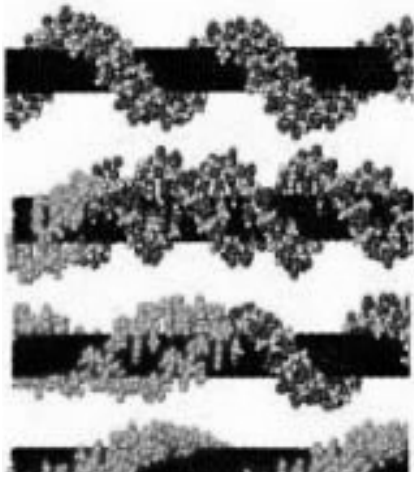

Fig. 5. DNA wrapped CNTs composite

In the experimental *IR*-spectra the vibration modes at 360, 450, 650, 864, 1231, 1400, 1444, 1575 cm^{-1}, which have been theoretically predicted for MWCNT with diameter 10 ÷ 40 nm, evaluated for DNA / MWCNT composite layer on these substrates. In these spectra the presence of added DNA bases group were identified (Fig. 6). CNTs can be modified with positive charges to bind DNA plasmids for gene transfection [2]. Used amine-terminated SWNTs and MWNTs functionalized bind DNA plasmids, and have achieved reasonable transfection efficiency. Amine groups were introduced to oxidized MWNTs for DNA binding and transfection, successfully expressing. Polyethylenimine (PEI) grafted MWNTs were used for DNA attachment and delivery, which afforded comparable efficacy to the standard PEI transfection method with the benefit of reduced cytotoxicity [7]. Small interfering RNA (siRNA) is able to silence specific gene expression via RNA interference (RNAi) and has generated a great deal of interest in both basic and applied biology [6]. With a cleavable disulfide bond linkage between siRNA and SWNTs, we successfully delivered siRNA into cells by nanotubes and observed gene silencing effect (Fig. 6, curve D_0). I further showed that our SWNT based siRNA delivery was applicable to those hard-totransfect human T cells and primary cells, which were resistant to delivery by conventional cationic liposome-based transfection agents (Fig. 6, curve D_1). Surface functionalization dependent cell uptake of SWNTs was observed. Compared with SWNTs coated with long PEG (5.4 kDa), shorter PEG (2 kDa) coated SWNTs with more hydrophobic surface exposed showed higher cellular uptake, which was favorable for siRNA delivery into cells (Fig. 6, curve D_3). I proposed that our SWNTs functionalized with short PEG (D_4) retained certain hydrophobicity (due to incomplete coverage of CNT sidewalls), which could cause binding and association with cells, resulting from hydrophobic interactions with hydrophobic cell membrane domains. The cell binding of SWNTs is an important first step for cellular entry via endocytosis. Results suggest that balanced chemical functionalization schemes that impart sufficient aqueous solubility and biocompatibility to CNTs, and retain the ability of CNT binding with cell surfaces are important for intracellular delivery of biomacromolecules by CNTs (Fig. 5.).

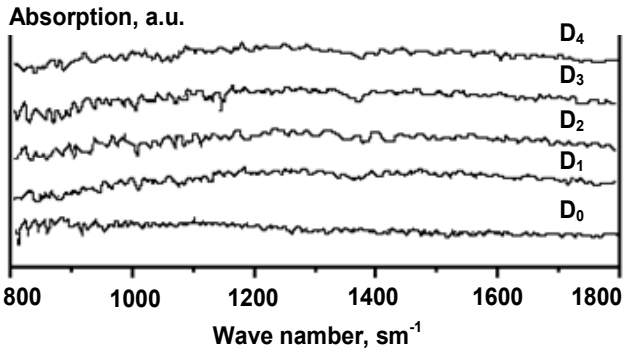

Fig. 6. FTIR spectra of DNA and CNTs/DNA composite

Conclusions. Various covalent and non-covalent chemistries have been developed to functionalize CNTs for biomedical research. Relying on their electric or optical properties, functionalized CNTs have been used for ultrasensitive detection. Clarify that *in vitro* and *in vivo* toxicities of CNTs are highly dependent on CNT functionalization. Well functionalized CNTs with biocompatible coatings are stable in biological solutions, and non-toxic *in vitro* to cells and *in vivo*.

CNTs are composed purely of carbon, while many inorganic nanomaterials (e.g. quantum dots) are composed of relatively more hazardous elements, such as heavy metals. The unique structure and tunable length of CNTs provide an ideal platform to investigate size and shape effects *in vivo*. Unlike conventional organic drug carriers, the intrinsic physical properties of SWNTs including resonance Raman scattering, photoluminescence, and strong *NIR* optical absorption can provide valuable means of tracking, detecting and imaging. Taken together, CNTs may serve as a unique platform for potential multimodality cancer therapy and imaging.

Using these results I assert that system of electron levels is self-formed at the (DNA + MWCNT) / Si interface as a result of DNA-tube interaction and optical absorption at 2.5 ÷ 3 eV is due to the MWCNT.

1. *Bianco A., Kostarelos K., Partidos C.D., Prato M.,* Biomedical applications of functionalised carbon nanotubes. // *Chem. Commun.* – 2005, – P. 571–577. 2. *Cao Q., Rogers J.A.,* Random networks and aligned arrays of SWCNT for electronic device applications. // *Nano Res.* – 2008 – Vol. 1 – P. 259–272. 3. *Chakravarty P., Marches R., Zimmerman N.S., Swafford A., Bajaj P., Musselman I.H.; Pantano P., Draper R.K., Vitetta E.S.,* Thermal ablation of tumor cells with anti body-functionalized SWNCT. // *Proc. Natl. Acad. Sci. U.S.A.* – 2008 – *Vol. 105* – P. 8697–8702. 4. *Dai H.*, Carbon nanotubes: Synthesis, integration, and properties. // *Acc. Chem. Res.* – 2002 – Vol. *35* – P. 1035–1044. 4. *Golberg D. Costa P.M., Mitome M., Bando Y.* Nanotubes in a gradient electric field as revealed by STM-TEM technique. // *Nano Res.* – 2008 – Vol. 1 – P. 166–175. 5. *Lowe C.R.*, Nanobiotechnology: the fabrication and applications of chemical and biological nanostructures. // *Curr. Opin. Chem. Biol.* – 2000. – Vol. 10. – P. 428–434. 6. *Rao A.M., Richter E., Bandow S., Chase B., Eklund P.C., Williams K.A., Fang S., Subbaswamy K.R.; Menon M.; Thess A.,* Diameter-selective Raman scattering from vibrational modes in carbon nanotubes. // *Science.* – 1997 – Vol. 275 – P. 187–191. 7. *Singh R., Pantarotto D., McCarthy D., Chaloin O., Hoebeke J., Partidos C.D., Briand J.P., Prato M., Bianco A., Kostarelos K.,* Binding and condensation of plasmid DNA onto functionalized CNTs: Toward the construction of nanotube-based gene delivery vectors. // *J. Am. Chem. Soc.* – 2005 – Vol. 127 – P. 4388–4396. 8. *Wang L., Zhao W., Tan W.*, Bioconjugated silica nanoparticles: development and applications. // *Nano Res.* – 2008. – Vol. 1 – P. 99–115.

Submitted on 23.09.12

UDC 621.382.23:538.945

O. Ivanyuta, Ph.D., V. Malyshev, engineer

NON-EQUILIBRIUM AMPLIFICATION OF JOSEPHSON VIBRATIONS

У роботі розглядаються деякі НВЧ властивості нерівноважних джозефсонівських контактів на бікристалічній поверхні. На відміну від стаціонарного ефекту Джозефсона, при нестаціонарному ефекті необхідно самоузгодження , що задовольняє вимогам динаміки квазічастинок і джозефсонівських фаз. Взаємодія між контактами істотно впливає на їх НВЧ властивості. В роботі проаналізована динаміка ланцюжка однакових контактів, у тому числі при зовнішньому НВЧ впливі (сходинки Шапіро), а також розглянута динаміка системи двох контактів з різними параметрами, де має місце ефект підсилення джозефсонівських осциляцій.

Ключові слова: ефект Джозефсона, НВЧ, сходинки Шапіро, підсилення.

The paper examines some of the microwave properties of nonequilibrium Josephson contacts bicrystal substrate. Unlike stationary Josephson effect, the unsteady effect to self-consistency that satisfies the requirements of quasiparticle dynamics and Josephson phases. Interaction between contacts significantly affect their microwave properties. This work analyzes the dynamics of a chain of identical contacts, including with external microwave exposure (Shapiro steps) and examined the dynamics of two contacts with different parameters where there is effect amplification Josephson oscillations.

Keywords: Josephson effect, microwave, step Shapiro, gain.

Introduction. Unlike stationary Josephson effect can be looked after at the serve of permanent tension between superconductors. Step of current begins to fix and the hertzian waves of high-purity($f_J / V = 483,6 \cdot MHz / \mu V$) emanate from a crack. Constancy of parameters is related to such constants of microelectronics, as a charge of electron and permanent Slat. At the height of tension a current through a contact will grow on steps origin of that like strengthening of echo in a resonant channel [8, 10].

This work aim was to study the mode of synchronously to phase synchronization of chain contacts, in that optimal terms are arrived at for a generation and reception of microwaves. Our researches showed that both at weak($h < 1$) and at strong cooperation($h > 1$) can take place as synchronously to phases modes, so are more difficult synchronous modes with the change of phases, heterogeneous modes with different anchorwomen by frequencies of contacts and chaotic modes.

Development and discussion. Surface wave resonators (SWR) are for many reasons very challenging for the realization of Josephson junction interactions with a microwave line. A high current density on SWR's superconducting (or metal) surface provides an effective coupling of junction arrays with the waveguide. Moreover the simplicity of SWR technology, the uniformity of microwave current density in superconducting film, make such circuits very attractive for applications in the future cryoelectronics. The SWR with Josephson junctions was fabricated using $Au - YBa_2Cu_3O_7$ bilayer on yttria-stabilized zirconia bicrystal substrate. The arrays were incorporated into SWR by meandering the bilayer across the grain boundary. Experimental results in the frequency range from 26 *GHz* to 40 *GHz* confirm strong coupling of the array with external micro-

wave current and uniformly distribution of this current along the whole 8 *mm* long array [3, 7, 5].

A thin film SWR was placed in the waveguide with dimensions $a = 7{,}1 \cdot mm$ and $b = 3{,}6 \cdot mm$ as shown in Fig.1. The resonant structure consists of an yttria-stabilized zirconia bicrystal substrate with the permittivity $\varepsilon = 26$ and a bilayer film *Au - YBCO* 2 with the length $\ell = 1{,}7 \cdot mm$ (along y) and the width $w = 7 \cdot mm$ (along *z*). The bilayer thickness h was equal to $0{,}5 \cdot \mu m$. The resonator was electrically connected with the wide waveguide face a ($\delta_1 = 0$) and fixed perpendicular to it ($\varphi = 90^0$) on the distance $\approx 0{,}5 \cdot$ mm from the narrow face of the waveguide. To provide dc series connection of bicrystal JJs the HTS film of SWR was patterned as shown in Fig. 2. The full number of slits with the width of $S = 15 \cdot \mu m$ along y directions was equal to the number of *JJs*, $N = 6$. The period of the structure was $L = 750 \cdot \mu m$. A small value of the normalized slit width $s = S / L = 0{,}02$ guarantied an inessential decreasing of the SWR quality factor Q and the shifting of the resonant frequency f_r compared to a continuous film SWR [3]. Fig. 3 and Fig. 4 showed the dependencies respectively of the unloaded Q and r_f of the SWR witch Josephson junction. At the critical temperature $T_C \approx 89 \cdot K$ increased approximately by a factor Q, but f_r increased by $\sim 1 \cdot \%$. Both variations were defined mainly by the thickness and properties of the gold cup film.

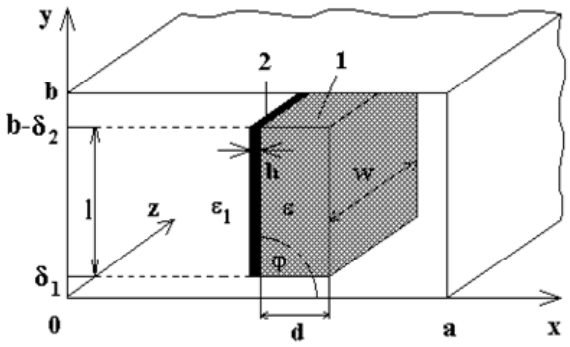

Fig. 1. Schematics of the surface wave resonator in the waveguide

The *JJs* embedded in the SWR were formed in the place of intersection of the $4 \cdot \mu m$ width bridge and grain boundary (GB) as shown in Fig. 2. The strips have a critical current, which is much larger than that of *JJs*, and are used to supply dc bias current and to measure the d_c voltage across every JJ in the array (Fig. 5). The distance between the first and the last junction was about $6 \cdot$ mm. The curve (a) in Fig. 4 shows the current-voltage (*I–V*) characteristic for 6 in series connected junctions without an applied microwave power. The minimum critical currents among the JJs in the array were $I_{Cmin} = 0{,}8 \cdot mA$. The value of characteristic voltage was $V_C \cong 80 \cdot \mu V$ at $76 \cdot K$. To supply ac bias, the microwave signal with the frequency $f_r \cong 31{,}5 \cdot GHz$ was applied. The amplitude of the first step reached its maximum value $\Delta I_1 \approx 0{,}3 \cdot mA$ at a very small power equal to $P \approx 80 \cdot \mu W$. It is important to note, that also steps with index $n = 2, \cdot 3$ were observed. This means that the microwave current is distributed very uniformly along the whole $6 \cdot$mm long array as it should be when SWR operates in the fundamental mode. The latter fact was also height oscillates absolutely equally in all series junctions documented by measuring the first current step height as a function of rf current for all 6 *JJs* in SWR (Fig. 5). The steps The same perfect dependencies were observed for $N = 11 \cdot JJs$ and for the steps with index $n = 0, \cdot 1, \cdot 2, \cdot 3$.

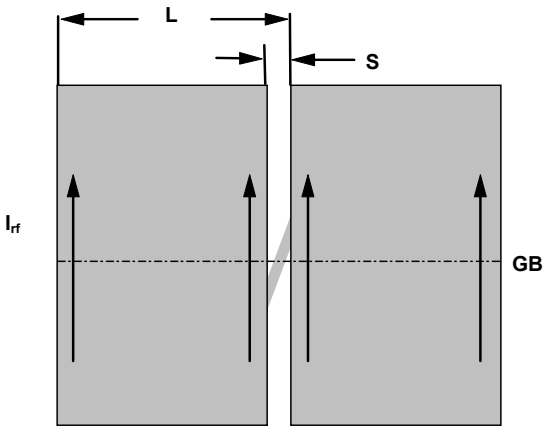

Fig. 2. Topologies of the series connected JJs arrays. Microwave bias current flows along the slits in y direction

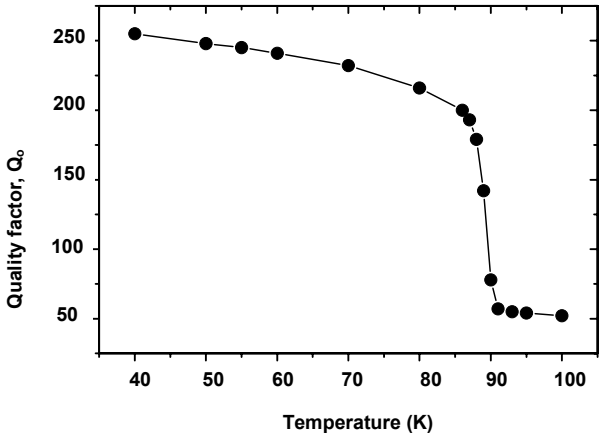

Fig. 3. Dependence of the unloaded quality factor *Q* on the temperature

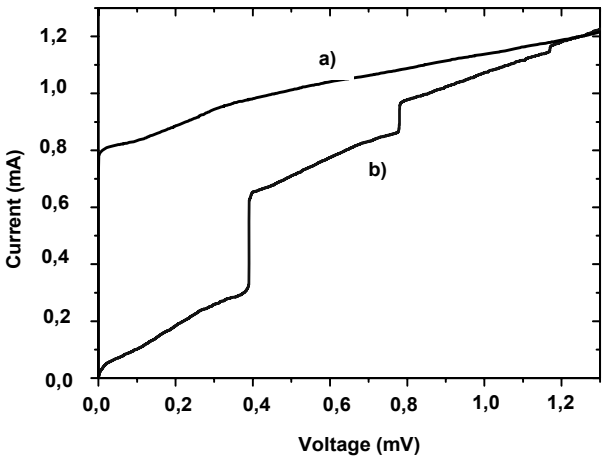

Fig. 4. *I-V* Curve of 6 series connected JJs (a) without microwave power and (b) with microwave power of 80μ*W*

From the microscopic point of view a basic process in a non-equilibrium superconductor is a change of function of distribution of quasi-particles, that is accompanied by the change of macroscopic descriptions of runback, power crack of Δ, level of Fermi E_f and invariant potential of Φ related to it [4, 8, 9].

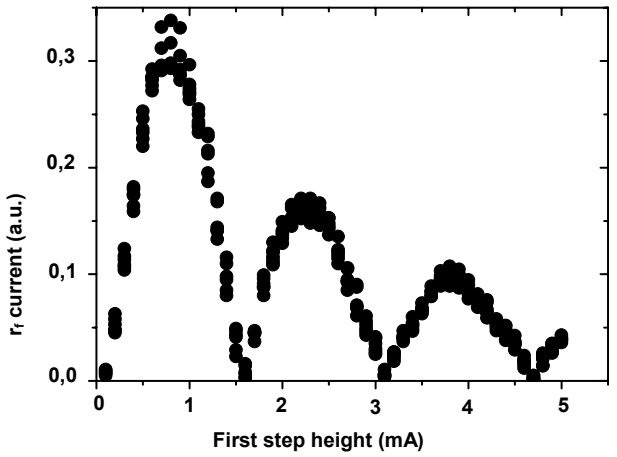

Fig. 5. The first step width against the amplitude of the external microwave current for each of the 6th JJs

The change of power crack takes place at the change of symmetric on energy of part function of distribution of n_ε (n_ε at $\varepsilon > 0$ describes distribution of almost electrons on energies, and n_e at $\varepsilon < 0$ - almost holes) and the way of life can in simplest case

$$1 = \lambda \cdot \int_{\Delta}^{\theta_D} \frac{1 - n_\varepsilon - n_{-\varepsilon}}{\left(\varepsilon^2 - \Delta^2\right)^{1/2}} \cdot d\varepsilon \qquad (1)$$

In general case gauge invariant potential Φ is included in dynamic equalizations. Expression for a charge assumes an air

$$\rho = -2e^2 N(0)\left(\Phi - \Psi\right) = -\frac{1}{4\pi r_d^2}\left(\Phi - \Psi\right) \qquad (2)$$

where $Y = \frac{1}{\varepsilon} \times \int_{\Delta}^{\infty}\left(n_\varepsilon - n_{-\varepsilon}\right) \cdot d\varepsilon$ - potential of electron-hole insufficient balance (being potential Y by just the same character comfortably at the receipt of dynamic equalizations), r_d - length of screening electric-field [8–9].

Ordinary correlation is able with the change of chemical potential $\frac{dj_{ij}}{dt} = \left(\frac{2|e|}{\left(h/2\pi\right)}\right) V_{ij}$ between the josephson difference of phases $j_{ij} = \left[\theta_i - \theta_j\right]$ singe and by voltage $V_{ij} = \left[f_i - f_j\right]$ violated. Instead, using determination F, we get non-equilibrium correlation of Josephson

$$\frac{dj_{ij}}{dt} = \frac{2|e|}{\left(h/2\pi\right)} V_{ij} + \frac{2|e|}{\left(h/2\pi\right)}\left(\Phi_j - \Phi_i\right) \qquad (3)$$

By basic parameters, qualificatory the degree of non-equilibrium effects of any type in tunnel structures and other systems with loosely-coupled interfaces, there are works $v\tau_\varepsilon$ and $v\tau_q$, where n is the so-called tunnel frequency that at the small thickness of layer of $d_0 << \ell_\varepsilon \ell_q$ is equal

$$v = \frac{1}{4e^2 N(0) R_N d_0} \qquad (4)$$

where R_N - resistance of contact up to par on unit of area. If $v\tau_\varepsilon > 1$ or $v\tau_q > 1$, then strong distortion formula distribution of quasi-particles is possible.

We will consider that the thickness of layers of d_0 is comparable with the depth of screening of electric-field of rd(that takes place in HTS) and many less than characteristic depths of relaxation nonequilibrium $d_0 << \ell_\varepsilon \ell_q$. The analysis of charge effects is simplified in this case, because it is possible to take AV of all sizes on the thickness of layer [1].

Other type of effects can be observed in the systems of contacts with substantially different parameters. We will consider the system of two contacts with a non-equilibrium middle electrode in a limit ? = 0. The initial system of equalizations looks like

$$\begin{aligned} \frac{d\varphi_1}{d\tau} &= \frac{2|e|}{\left(h/2\pi\right)} V_1 + \frac{2|e|}{\left(h/2\pi\right)} \Phi \\ \frac{d\varphi_2}{d\tau} &= \frac{2|e|}{\left(h/2\pi\right)} V_2 - \frac{2|e|}{\left(h/2\pi\right)} \Phi \end{aligned} \qquad (5)$$

$$\begin{aligned} J_{ci} \sin j_i + \frac{V_i}{R_i} + C_i \frac{dV_i}{dt} &= J(t), \cdot\cdot i = 1, \cdot 2 \\ \tau_q \Gamma \frac{d\Phi}{dt} + \Phi &= -\eta_1 J_{c1} R_1 \sin\varphi_1 + \eta_2 J_{c2} R_2 \sin\varphi_2 \end{aligned} \qquad (6)$$

Passing to the dimensionless variables, we will consider that characteristic tensions of contacts coincide $J_{c1}R_1 + J_{c2}R_2 = V_C$. This supposition is fully reasonable, for example, for tunnel contacts, different transparency of barrier. Then we will get

$$\begin{aligned} \beta_1 \frac{d^2\varphi_1}{d\tau^2} + \frac{d\varphi_1}{d\tau} + \sin\varphi_1 - \mu - \beta_1 \frac{d\mu}{d\tau} &= J_1, \\ \beta_2 \frac{d^2\varphi_2}{d\tau^2} + \frac{d\varphi_2}{d\tau} + \sin\varphi_2 + \mu + \beta_2 \frac{d\mu}{d\tau} &= J_2, \\ \alpha\Gamma \frac{d\mu}{d\tau} + \mu &= -\eta_1 \sin\varphi_1 + \eta_2 \sin\varphi_2 \end{aligned} \qquad (7)$$

where $\beta_i = \frac{2eJ_{ci}R_i^2 C_i}{\hbar/2\pi}, \cdot\cdot \alpha = \tau_q \omega_C, \cdot\cdot j_i = \frac{J}{J_{ci}}, \cdot\cdot$

$\mu(t) = \frac{2e}{\left(h/2\pi\right)\omega_C}\Phi(t), \cdot\cdot \omega_C = \frac{2eV_?}{\left(h/2\pi\right)}, \cdot\cdot \tau = \omega_C t$.

We will suppose now, that transparency (tunnel frequency) of the second barrier considerably anymore, what first $v_1 << v_2$. Then critical currents and parameters of non-equilibrium of contacts substantially differentiate $J_{C1} << J_{C2}, \cdot\cdot \eta_1 << \eta_2$. We will consider the area of external currents greater, than critical current of the second contact. Then $j_2 > 1$ and $j_1 >> 1$. By a deposit from a member $\eta \sin\varphi_1$ in equalization for m it is possible to scorn, and then in simplest case $\alpha\Gamma << 1$ and $\beta\omega^2 << 1$ we will get

$$\mu \approx \eta_2 \sin\varphi_2, \qquad (8)$$

$$\frac{d\varphi_2}{d\tau} + \left(1 + \eta_2\right)\sin\varphi_2 = j \qquad (9)$$

It ensues from this equalization, that a critical current effectively increased in $1 + \eta_2$ and, accordingly, amplitude of Josephson oscillations will increase. At the same time high-frequency Josephson oscillations on the first contact

with frequencies in j_1 / j_2 of one times greater, than on the second contact, it is possible not to take into [11].

Conclusions. This thesis considered examples of nonlinear oscillator arrays with a coupling which is a dynamical unit by itself. Each of the systems analyzed in the thesis led to the discovery of new and interesting phenomena, and also might have promising scientific applications.

It was shown that taking advantage of proper positioning of oscillating elements in a distributed array can provide a resonant architecture and a situation when weak physical coupling is effectively amplified, increasing the degree of coherence. I set up the problem of synchronization in the load-free Josephson transmission line and analyzed the effects of the coupling, which is intrinsically distributed.

Especially perspective are artificial tunnel structures with large transparency of barriers and internal josephson contacts in high temperature superconductors [11].

1. *Cawthorne A.B., Barbara, P., Shitov, S.V., Lobb. C.J., Wiesenfeld, K. Zangwill, A.*, Synchronized oscillations in Josephson Junction arrays: the Role of Distributed Coupling // Phys. Rev. B. – 1999. – 7575, Vol. 60. 2. *Ciria J.C., Pacetti P., Paoluzi L., Giovannella C.*, Photofluxonic Detection in Ladders and 2D Arrays of Josephson Junctions // Nucl. Inst. and Meth. in Phys. Res. A.– 1996. – 128, Vol. 370. 3. *Engel A., Semenov A.D., Hubers H.W., Il'in K., Siegel M.*, Fluctuation effects in superconducting strips // Physica C. – 2006. – 444, N 12. 4. *Golubov A.A., Kuprianov M.Yu., Il'ichev E.*, The Current-phase Relation in Josephson Junctions // Rev. Mod. Phys.– 2004. – 411, Vol. 76. 5. J*osephson B.D.*, Weakly Coupled Superconductors. Superconductivity, Vol. 1 (Parks, R. D. ed.), Marcel Dekker, 1969. 6. *Mygind, J., Pedersen N.F.*, Microwave radiation from superconducting arrays of Josephson junctions, Macroscopic Quantum Phenomena and Coherence in Superconducting Networks, (Giovanella, C. and Tinkham, M., eds.), Singapore: World Scientific, 1995. 7. *Morgan M., Weinreb S.*, A Millimeter-wave perpendicular coax-to-microstrip transition // IEEE Trans. Micro. Th. and Techniques. – 2002. – 817, N 50. 8. *Likharev, K.K.*, Superconducting weak links // Rev. Mod. Phys. – 1979. – 101, N 51. 9. *Likharev K.K.*, Dynamics of Josephson Junctions and Circuits. Gordon and Breach, New York, 1986. 10. *Sergeev A., Semenov A., Trifonov V., Karasik B., Gol'tsman G., Gershenzon E.*, Heat transfer in YBaCuO thin film - sapphire substrate system // J. Supercond. – 1994. – 341, N.7. 11 *Zhang T.*, Design and integration of HTS filters with a Josephson device 2012 Supercond. Sci. Technol. – 2012. – 105014, N.25.

Submitted on 02.09.12

UDC 577.3

K. Karpenko, post grad. stud., R. Yatsiuk, post grad. stud., M. Kononov, PhD., O. Sudakov, Ph.D.

SIMULATION AND RESEARCHING OF NETWORK STRUCTURE WITH 48 NEURAL ELEMENTS

Наведено основні актуальні фізичні моделі біологічного нейрона, проведено їх аналіз, вказано на переваги і недоліки конкретних моделей, обґрунтовано їх межі застосування при моделюванні нейронних мереж. Розглянуто нейронну мережу 6-ти шарової структури із 48 елементів з різними режимами активності: регулярні спайки, хаотичні спайки, регулярні та хаотичні бьорсти, та інш. Для дослідження обрано модель Іжикевича, яка дозволяє відтворювати різні типи активності, притаманних реальним біологічним нейронам.

Ключові слова: нейронні мережі, моделювання, модель Іжикевича, спайки, бьорсти.

The basic general physical models of biological neurons and mechanisms of its functioning were considered, their analysis was done, the advantages and disadvantages of particular models were shown, their scope of applicability in modeling neural networks was considered. It was considered the 6-layer neural network structure of 48 elements with different states: regular spikes, chaotic spikes, regular and chaotic bursting, etc. For simulation it was chosen the Izhykevich's model that lets to display different types of activity inherent for real biological neurons.

Keywords: neuron networks, simulation, Izhykevich's model, spikes, bursts.

1. Introduction. Relevance of modeling. The peculiarity of the biological approach to neural networks is that, it is based on the observation of processes at the cellular level and their description. The rapid accumulation of experimental data for the last quarter of XX century prepared the foundation, if not for a final answer to the question: "How a human thinks?", then at least, to try to build a new concept of the brain according to recent advances in physics, biophysics and computer equipment, that would not contradict experimental data. There are other desires for rapid development of neuroscience that are caused by the practical demands of medicine and by finding innovative ways to create an "intellectual" technology. [6]

Therefore, physical, mathematical and computer modeling of electrophysiological processes in biological objects are ones of the current and future research directions.

2. Physical models of biological neuron. Hodgkin and Huxley, based on experiments with membrane giant squid axon, found that the current, which flows through the membrane, can be represented as the sum of several components - bias current through the equivalent capacity of membrane, ion currents of conduction channels for Na^+ and K^+, and current leakage. In the base of Hodgkin-Huxley model [7] is the first law of Kirchhoff. The model accurately describes the dynamics of membrane potential, allows to simulate the behavior of a neuron in the presence of an external current, which flows through the membrane, it well describes the activation and deactivation of Na-currents, activation Ca-currents, the process of generation of pulses, subthreshold stimulation, refractoriness, hyperpolarization of fibers after momentum accommodation and others. The full system of equations is as follows:

$$C\frac{dV}{dt} = g_K(V - V_K) + g_{Na}(V - V_{Na}) + I(t),$$

where

$$g_K = g_{K\max} n^4,$$

$$g_{Na} = g_{Na\max} m^3 h,$$

$$\frac{dn}{dt} = \alpha_n(1-n) - \beta_n n,$$

$$\frac{dm}{dt} = \alpha_m(1-m) - \beta_m m,$$

$$\frac{dh}{dt} = \alpha_h(1-h) - \beta_h h,$$

$$\alpha_n = \frac{0.01(V-10)}{1-e^{(25-V)/10}},\ \beta_n = 0.125e^{-V/80},$$

$$\alpha_m = \frac{0.1(V-25)}{1-e^{(25-V)/10}},\ \beta_m = 4e^{-V/18},$$

$$\alpha_h = 4e^{-V/20},\ \beta_h = \frac{1}{1+e^{(30-V)/10}},$$

where V – membrane potential, V_K, V_{Na} – potassium and sodium equilibrium potentials, respectively. However, this model has one drawback – it requires a very large number of computing resources and today the simulation of neural networks with many elements using this model is impossible. Therefore, there is a need in simplified models that

retain the essential features of the dynamics of Hodgkin-Huxley neuron, but require less computer resources.

Another popular model of Hodgkin-Huxley type, which describes the dynamics of membrane potential as a function of ion currents, flowing through the membrane of the neuron, was developed by Terman and Rubin and their collaborators in 2002 [5], and is described by the equation:

$$C_m \frac{dv_s}{dt} = -I_L - I_K - I_{Na} - I_T - I_{Ca} - I_{APH} - I_{G\to S},$$

where v_s is the membrane potential of neuron in mV, and C_m – the conductance of membrane (normalized to 1 pF/μm^2). And currents (in pA/μm^2) are defined by the equations:

$$I_L = g_L(v_s - v_L),$$

$$I_K = g_K n^4 (v_s - v_K),$$

$$I_{Na} = g_{Na} m_\infty^4(v_s) h(v_s - v_{Na}),$$

$$I_T = g_T a_\infty^3(v_s) b_\infty^2(r)(v_s - v_T),$$

$$I_{Ca} = g_{Ca} s_\infty^2(v_s)(v_s - v_{Ca}),$$

$$I_{APH} = g_{APH}(v_s - v_K)\frac{[Ca]_i}{[Ca]_i + k_1},$$

$$I_{G\to S} = g_{G\to S}(v_s - v_{G\to S})\sum_j s_j,$$

There was a problem for researchers, who simulated a large network: to choose the optimal approach, scale modeling. Researches searched for a reasonable compromise between high detail of single element with the description of its dynamics and dimension of the network. Limitation of computational resources generated set of simplified models, which allow, on the one, hand satisfactorily simulate the dynamics of individual elements, and, the other, to effectively use computing resources. Because these models reproduced the dynamics of membrane potential as a phenomenon, without detailing the mechanisms that lead to this phenomenon, they came to be called phenomenological.

Among simplified models it is a classic model with nonlinear right-hand side, proposed by Fitz-Hugh-Nagumo [1] and then modified by Nagumo:

$$\frac{du}{dt} = a + bu + cu^2 + du^3 - v + I_{syn},$$

$$\frac{dv}{dt} = \varepsilon(eu - v),$$

where u and v – the membrane potential and additional variable respectively, others designation *a, b, c, d, ε, e* – constants, model parameters, from the choice from which depends on the appearance of obtained oscillations. This model, depending on the parameters, can simulate a set of types of neuron activity. In its classic form, with a steady second equation, the model demonstrates such phenomena as adaptation, post-anod exaltation and the reducing of the amplitude of AP in burst mode.

In 2001 Eugene Izhikevich [3] proposed a model of neuron, which somewhat simplifies the FHN model. It is based on a square polynomial in the right side of the equation for membrane potential, also is two-compartment model and contains an additional condition for discharge:

$$\frac{dv}{dt} = 0.04v^2 + 5v + 140 - u + I,$$

$$\frac{du}{dt} = a(bv - u),$$

$$v \leftarrow c, u \leftarrow u + d, \text{ if v>=30мВ},$$

where v and u are the dimensionless membrane potential and membrane reconstitution respectively, *a, b, c i d* – dimensionless parameters. The variable u simulates the activation of ionic K^+ currents and the deactivation of ionic Na^+ currents and provides negative feedback to v, I simulates external currents. This model was used for simulation of neural network which contained 10^5 neurons of the cerebral cortex that generated fluctuations in the form of spikes and bursts with delays and the synchronization of oscillations.

In [4] it is shown that this model can reproduce all twenty types of real biological activity of neurons depending on the values of four model parameters. Over the subjective opinion of the author, the only one drawback of this model is a partial dissolubility of its history due to discharge of membrane potential when reaching the threshold.

3. The choice of the model. The complexity of modeling dynamic properties and the using of large computer resourses by many-compartment and point models, based on equations of Hodgkin and Huxley, made it necessary to search for phenomenological models of the neuron, which would enable to reproduce the real cells dynamics as a phenomenon, without detailing the processes that lie at its basis.

Estimates of most models of demand for computing resources presented in [9]. In this paper it is presented the estimates of amount of operations that must be done to simulate vibrations of one neuron for 1 ms using the Euler first-order fixed-step equation method to solve a particular model. Izhikevich model requires 13 floating point operations to simulate fluctuations during 1ms, provided that the sampling time chosen equal to 1ms. For Fitz Hugh-Nagumo model 72 operations are needed for modeling of neuron during 1 ms at discretization time of 0.25 ms (at large time discretization the model loses its essential features). Rubin-Terman model requires 600 floating point operations when selecting discretization time of 0.1 ms, and Hodgkin-Huxley model with the same parameters requires 1200 operations.

The most successful of the above models in this case is Izhikevich model that requires relatively few computing resources and can simulate almost all kinds of fluctuations. Also it can be used the Rubin-Terman model, if the number of neurons in network order would be lower.

4. Connections. When simulating systems of analysis, processing and converting the information the most important is to preserve the quality of correspondence between biological neural networks and their models. The most significant correspondence is in the structure of connections between neurons, and is in the properties of the transformation of information flows in each neuron network. [8]

In this work it was investigated homogeneous types of neural networks – where all network elements are identical and form the same type of neural connections. All simulated networks are fully connected, networks in which each element of the next layer receives synapses from all the previous elements.

The main element, that takes part in almost all physiological processes, is the cerebral cortex. It has six layers, contains from 10 to 14 billion neurons and has a view of hierarchical system of neural networks – cortical columns. With this structure human can construct representations of complex objects. Six layers of columns numbered by roman numerals from superficial to deep. The first layer contains very few neurons, and the deeper layer has the more neurons. But the neurons of each level associated with almost all other hierarchical levels of the column, and in some cases with neurons of their level.

It was considered the neural structure in the form of columns, which consists of six layers of neurons. At each level each neuron is connected to all neurons of its level and the next (lower in the hierarchy) level. The scheme of this structure is shown in Fig. 1.

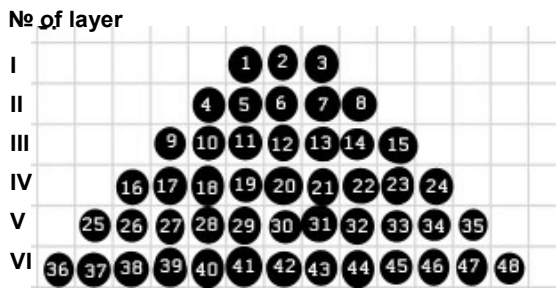

Fig. 1. The scheme of neural structure with 48 neural elements

5. Software implementation and results. The own software for modeling neural network was built, interface of which is as follows (Fig. 2).

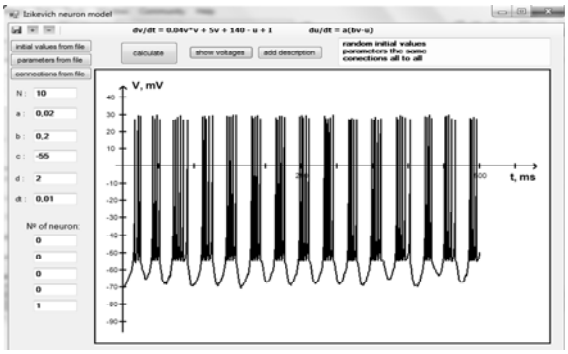

Fig. 2. The interface of own software

This tool was created by using the programming language C# and it is based on the following algorithm (Izhikevich neuron model which was calculated by using the method of Euler, fig. 3): where v[] and u[] – arrays values of corresponding potentials; a[], b[], c[], d[] - arrays values of parameters of neurons that can be set the same for all neurons via the program or get within a file the individual parameters for each neuron; connections[i][k] – the list that contains information about communications of system and can be formed by default tools (all to all), or also can be set by the file. If you need more flexibility to set the properties of the investigated system, it is possible to specify an external current which is fed to the neuron (for the case of modeling cortical columns it is the current that goes through the synapses of neurons from other cortical columns). The initial value for the membrane potential v[], depending on the needs of the user, can specify random or, again, can be set from the file.

Our first objective was to determine the maximum fixed time step interval *dt* for which the equations converge. When solving differential equations numerically one must use a time step sufficiently small to capture the dynamics of the solution; on the other hand, using a time step too small unnecessarily decreases the computing program while yielding no additional information. The goal is to find a time step that is a happy medium between these two conflicting requirements. The normal process to achieve this is to start with a relatively large value of *dt* for the simulation, then gradually decrease the value for subsequent runs until the observed solution of the equations no longer changes significantly.

Figures 4 through 7 show the results of runs for decreasing values of the time step *dt*. As can be seen from the figures, although the general form of the output waveforms remains roughly the same, the times at which the generated spikes fire continue to change far below *dt* = 1.0.

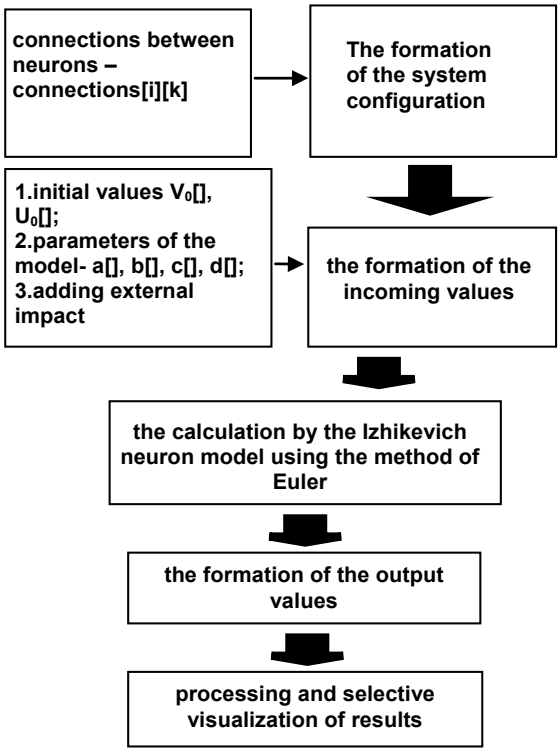

Fig. 3. The scheme algorithm of program implementation

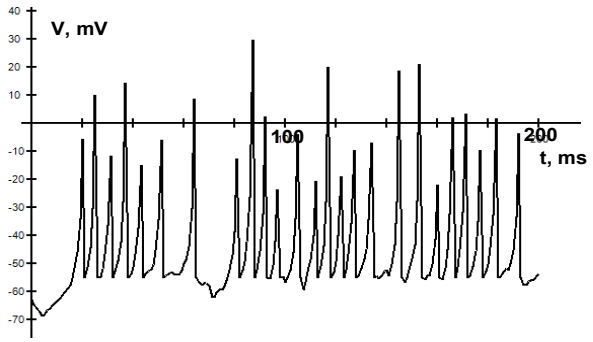

Fig. 4. dt =1.0 msec

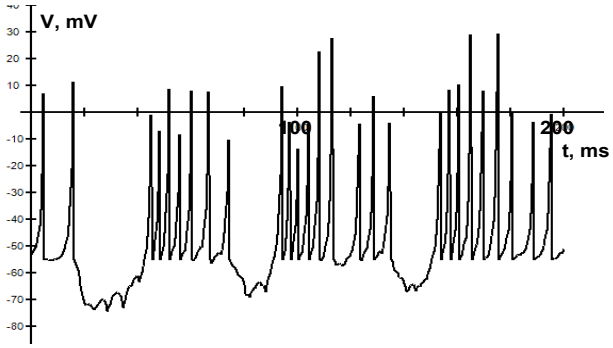

Fig. 5. dt =0.5 msec

From these we would estimate that we should have $dt \leq 0.01$ for sufficiently convergence.

It was considered homogeneous fully connected neural network, the hierarchical structure of which is close to the

cortical column and has six layers: the first layer has three neurons, the second – five, the third – seven, the fourth – nine, the fifth – eleven, the sixth – thirteen neural elements.

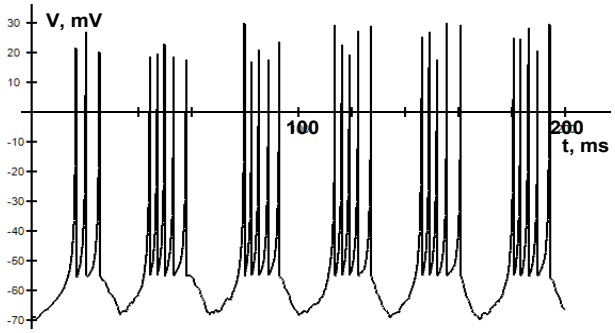

Fig. 6. dt =0.05 msec

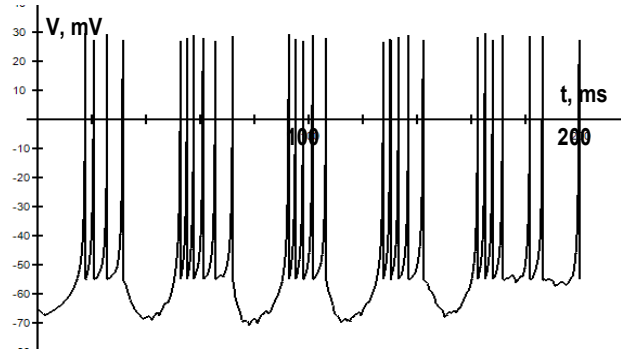

Fig. 7. dt =0.01 msec

The sixth level is the deepest or the lowest level of neural structures, it receives the synaptic current from the lower cortical columns. In this work, we set the current through the file for each neuron (from 36th to 48th, please. Fig. 1) of sixth layer. By simulation it was found that neural activity at a lower level has the form – *class 2 excitable* (Fig. 8):

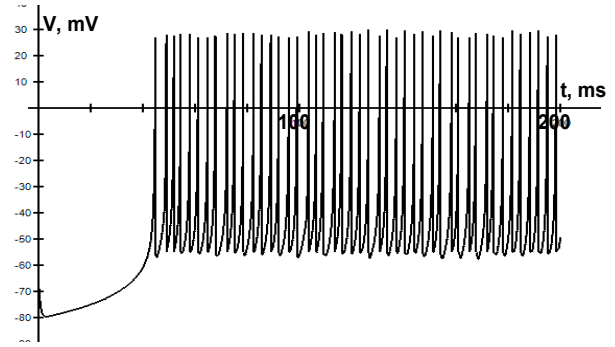

Fig. 8. The neural activity of neurons at sixth layer of network

Thus, the so-called primary information comes to the sixth level, later on, this information is processed by neurons of the level and grouped in a sequence and transmitted to higher levels.

If we analyze neural activity of the following, the fifth, level of the studied network – we can see that the behavior of the membrane potential of neurons differs significantly from the lower level, and looks like – mix mode: irregular tonic bursting and spiking (Fig. 9).

This dynamic suggests that at this level there is a recognition, processing and analysis of sequences of impulses, that came from the lower level, and such sequences as "structural units" are formed in greater consistency, in the result is "a sequence of sequences," which transferred on the hierarchy of levels.

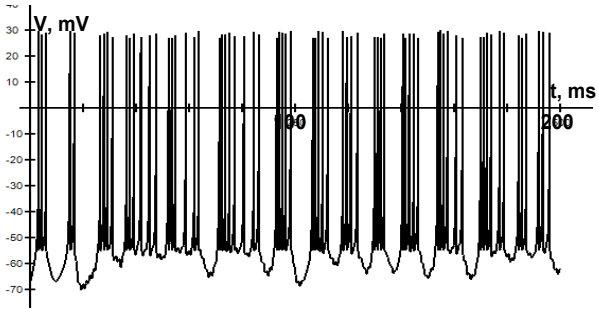

Fig. 9. The neural activity of neurons at fifth layer of network

The fourth-layer dynamics is not significantly different from the previous layer, the appearance of the membrane potential of neurons is not chaotic, – there is regular tonic bursting (Fig. 10):

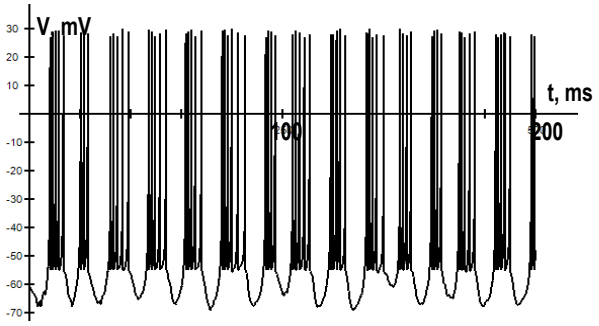

Fig. 10. The neural activity of neurons at fourth layer of network

Accordingly, there is recognition of "sequences of sequences," which came from the lower layers, processing and analysis, and the combination of more structured pulses, which, in turn, will go to higher levels of cortical hierarchy.

At the third level the neural activity of the studied network takes the form – mix mode: regular tonic double spiking and bursting (Fig. 11).

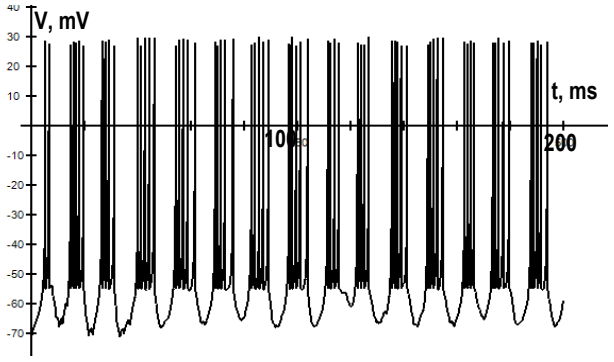

Fig. 11. The neural activity of neurons at third layer of network

On the second level the appearance of membrane potential of neurons becomes like – mix mode: regular single and double tonic spiking and tonic bursting (Fig. 12):

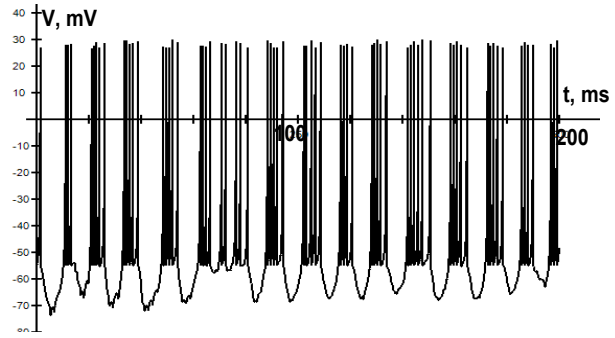

Fig. 12. The neural activity of neurons at second layer of network

The second and the first level of the cortical column are higher levels, on which there is the structural organization of the information flows from lower levels and is transformated into a final signal, which will be transmitted to the sixth level of neural columns that are higher of the anatomical location.

On the first neural level there is kind of the neural activity – mix mode: single spiking and regular tonic bursting (Fig. 13).

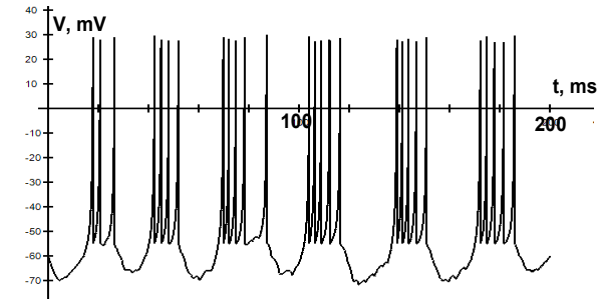

Fig. 13. The neural activity of neurons at first layer of network

Research is carried out with model parameters: a=0.02, b=0.2, c=-55, d=2 and time of discretization dt=0.01ms. Only for convenience the graph shows the membrane potential for a single neuron of the corresponding layer of the cortical structure, because the activity of each neuron within a layer has the same look and only shifted by a phase in time.

After simulation the neuron structure in our program, it has made sure that these results closely matched to the theory in literature.

6. Conclusions. The simulation of neurons and neural networks can explain not only how to run certain processes, but also reveal phenomena previously unknown and which are not obvious. From the methodological point of view simulation replaces the synthesis in cognition of nature.

Cortex is a hierarchical system of neural networks – cortical columns. With this structure human can construct representations of complex objects. Each object in memory is stored as a sequence of characteristics. But features can also be objects. Thus the representation of the object in the memory is a sequence of sequences. The hierarchical structure allows preserving of such structures. Depending on the complexity of the object, to its memory or recognition should involve columns from different hierarchical levels. So the simplest objects, that represented by small sequence of characteristics, or only one characteristic, involve columns from lowest levels in the hierarchy. The more complex object and on the larger level of abstraction is, then the higher column needed to remember or recognize it.

Such representation of the cerebral cortex allows understanding and describing the process of storing information about objects. Thus each object is a sequence of characteristics, where each characteristic may be an object, which is a sequence of sequences.

The knowledge of the structure allows building mathematical, and then the computer model of human memory, and investigating its performance. These studies may provide better representation of human memory, thinking and intelligence.

1. *Fitzhugh R.* Impulses and physiological states in theoretical models of nerve membrane//Biophysical Journal, 1961, 1, p.445–466. 2. *Hodgkin A.L.,* Huxley A.F. A quantitative description of membrane current and application to conduction and excitation in nerve //Physiology. – 1954. – № 117. – P. 500–544. 3. *Izhikevich E. M.* Simple model of spiking neurons //IEEE Transactions on Neural Networks. – 2003. – 14, №6. – P. 1569–1572. 4. *Izhikevich E. M.* Which Model to Use for Cortical Spiking Neurons? //IEEE Transactions on neural networks, 15: p.1063–1070, 2004. 5. *Terman D., J.E. Rubin, A.C. Yew,* and *C.J. Wilson.* Activity patterns in a model for the subthalamopallidal network of the Basal Ganglia//The journal of Neuroscience, 22(7):2963–2976, April 2002. 6. *Борисюк Г.Н., Борисюк Р.М., Казанович Я.Б., Иваницкий Г.Р.*. Модели динамики нейронной активности при обработке информации мозгом – итоги "десятилетия" //Успехи физических наук. – 2002. – 172, №10. – С.1189–1214. 7. *Горячко В.* Математична модель поширення нервового імпульсу в нейроні//Теоретична електротехніка. – 2005. – №58. – С. 20–26. 8. *Романов С.П., А.В. Бахшиев.* Математическое моделирование процессов преобразования импульсных потоков в естественном нейроне //Нейрокомпьютеры: разработка, применение, №3, 2009. – с.71–80. 9. *Тимощук П. В.* Порівняльний аналіз моделей нейронних осциляторів//Автоматика, вимірювання та керування. 2009. – №639. – С. 243–249.

Submitted on 23.05.12

UDC: 538.911, 004.8, 004.932

S. Korin, post grad. stud., D. Gryaznov, assist., O. Tretiak, Doct. Sci.

MODIFICATION TO BACK-PROPAGATION ALGORITHM FOR TRAINING ARTIFICIAL NEURAL NETWORKS

Термін навчання штучних нейронних мереж суттєво залежить від багатьох факторів, а саме таких як кількість нейронів та шарів, алгоритм навчання та його параметри. Оскільки алгоритм навчання і кількість шарів залежать від специфікації задачі, вони не розглядаються у цій статті. При вирішення задач з нескінченним числом навчальних вибірок, завжди потрібно обирати ШНМ з найбільш можливою кількістю нейронів у шарах. Запропонований новий метод значно прискорює процес навчання штучної нейронної мережі за допомогою модифікації до класичного алгоритму зворотного поширення помилки саме для описаних задач. Алгоритм був протестований на певній математичній задачі та було показано, що він дає кращі результати в порівнянні зі звичайним алгоритм зворотного поширення помилки.

Ключові слова : Штучна нейронна мережа, алгоритм зворотного поширення, багатошаровий персептрон, РСГР.

Training time of Artificial neural network greatly depends on many factors such as neurons' quantity, layers' quantity, training algorithm and its parameters. Since training algorithm and layers' quantity depend on solving task specifications, they are out of scope in this article. In tasks with infinite number of training samples, we should have a biggest number of neurons in layers as possible always. In this case, we offer a new method, which greatly accelerates a process of artificial neural network training by back-propagation algorithm modification. We tested our algorithm on mathematical task model and found that it gives better results in comparison with common back-propagation algorithm.

Keywords : Artificial neural network, Back-propagation algorithm, Multy-layer perceptron, DLTS.

Introduction. Back-propagation algorithm [5, pp. 216–245] is one of the most popular method of feed-forward multilayer artificial neural networks (ANNs) training. However, this method has some shortcomings [9, pp. 52–54]. First of them, ANN can trap in local minima, but not global, during training process. Second, network structure features are closely connected with solving problem properties and their generalization capabilities may be lost. Finally, they converge very slowly and convergent time greatly depends from ANN topology and increases with increasing quantity of neurons and layers. But sometimes we need a great ANN to solve some task. In papers [1,4,8] the methods of growing and automatically resizing network structure by adding neurons into hidden layers is described. But it is suitable for tasks with a few training samples' quantity for increasing ANN generalization capabilities and avoiding overfitting at the same time [2]. However, in cases with infinite number of training samples we can and should have the biggest ANN as possible without caring about overfitting. On the other hand, we need to care about convergent time. Our method is suitable exclusively for similar tasks.

Task model. For method consideration, we used ANN for evaluating parameters C_i and τ_i of function (1)

$$f(t) = \sum_{i=1} C_i e^{-\frac{t}{\tau_i}} \qquad (1)$$

From mathematical point of view, that function is a simplified Fredholm equation of 1st kind which is ill-posed problem.

This task was appeared with evaluating deep centers physical parameters in semiconductor structures by deep-level transient spectroscopy (DLTS) [6,7]. This problem is fully consistent with the type of problems described in the abstract, because the parameters C_i and τ_i are obtained from continuous range when all possible cases are simulated.

ANN was chosen as fully connected feed-forward multilayer perceptron with sigmoid as a transfer function. The ANN input data are presented as depiction of function (1) as shown below on figure 1.

The values on the input neurons depend on ratio of area's square under the function and full area's square of each cell. For example, from fig.1: input [1,1]=1, input [10,10]=0, input [1,7]=0.5, input [5,1]=0.95, etc.

In the general case, the quantity of addends in (1) is unknown. Therefore, a specific function (2) for C_i and τ_i representation in output layer was suggested.

$$f(C,\tau) = \sum_{i=1}^{n} C_i e^{-\frac{(\tau-\tau_i)^2}{\alpha}} \qquad (2)$$

This function (2) represents each C_i i τ_i as size and position of peak in output neurons as showed on figure 2. For example, output [0]=0.0, output [1]=0.4, output [2]=1.5, output [3]=3.5, etc. Eventually, on fig.2, it is shown that i=2, because two peak are there with C_1=8, τ_1=5 and C_2=2, τ_2=15.

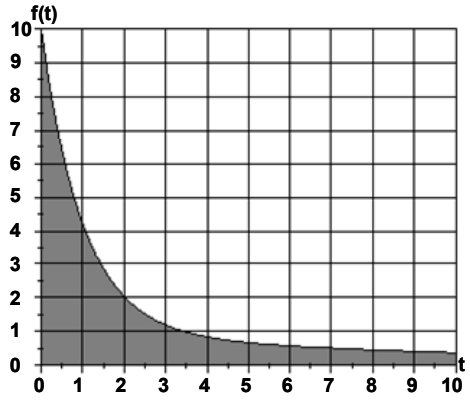

Fig. 1. The illustration for input data form

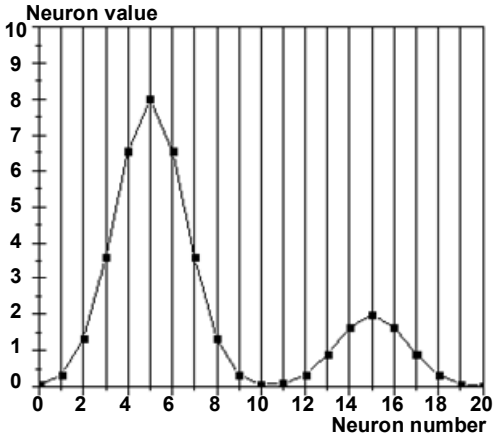

Fig. 2. The illustration for output data form

We use back-propagation algorithm with modification described in [3,10] for learning rate for that ANNs training.

The values of parameters C_i and τ_i are from continuous diapason. It means that we work with infinite number of training samples. Hence, we need to build ANN with great neurons' quantity in layers for solving this task model. Neu-

ron links' quantity will be great too, thus it will need a bigger quantity of training iterations. Therefore time to find direction for error minimization increases also, because it is necessary to process more variables. Eventually ANN's training time will be great. It is illustrated on figure 3, where MTE - mean testing error depends on training time.

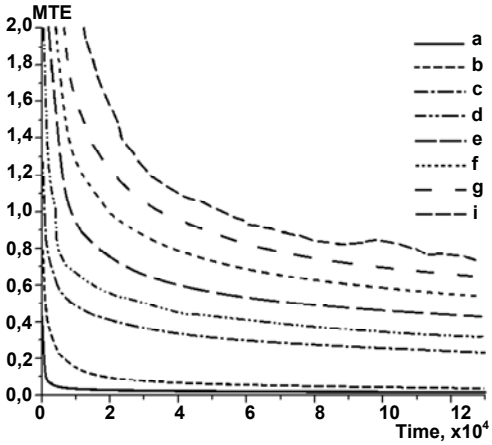

Fig. 3. ANN's training process with various neurons' quantity in layers : a) 64; b) 144; c) 256; d) 400; e) 576; f) 784; g) 1024; i) 1296 neurons

Method's description. Let's consider an ANN with three layers for understanding method technology. Imagine that the required quantity of neurons in each layer to solve some task is 4x2.

Firstly, it is necessary to build an ANN with three layers but a neurons' quantity in each layer is divided into four, i.e. two neurons in each layer. And then starts to learn this ANN using back-propagation algorithm during some time.

Secondly, build required ANN with three layers and 4x2 neurons in each of them. But now the synaptic weights for each neuron are selected from closest neuron's synaptic weights from previous ANN as shown on figure 4 and divides into four each of them.

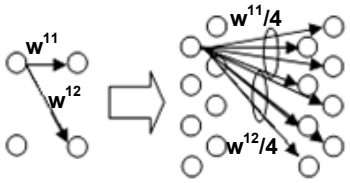

Fig. 4. Modifying a synaptic weights

As a result of our synaptic weights manipulation we receive a required neural network with preconfigured synaptic weights, not randomize. And as will be shown later, that ANN will train faster.

The results and discussions. We compared training process with common back-propagation algorithm and with the same algorithm but with our modification of synaptic weights for ANN with 256 neurons in each layer.

Firstly, we were training an ANN with 64 neurons in each layer during half of all training time. Then we calculated the synaptic weights for required ANN (with 256 neurons in each layer) based on synaptic weights from previous ANN (with 64 neurons in each layer). Thereafter we were training a built ANN during next half of time.

Training process is shown on figure 5. The training error increased after required ANN was built. However it returned to previous error level rapidly. Consequently, we can see a great decreasing of ANN error within the same training time.

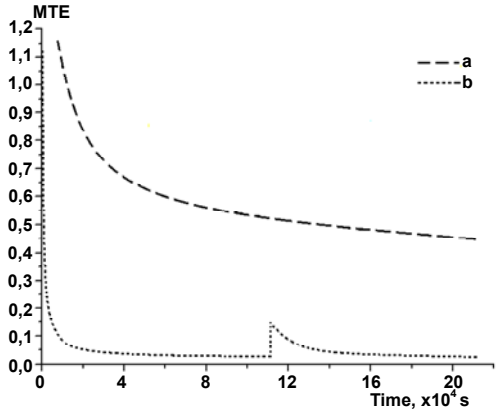

Fig. 5. ANN's training process with a) common back-propagation algorithm and b) with modification

We investigated a dependence of training error on ratio between training time for new ANN and for required ANN. Method efficiency (ME) is determined as ratio between training error for modified and for common back-propagation algorithm after expiring training time.

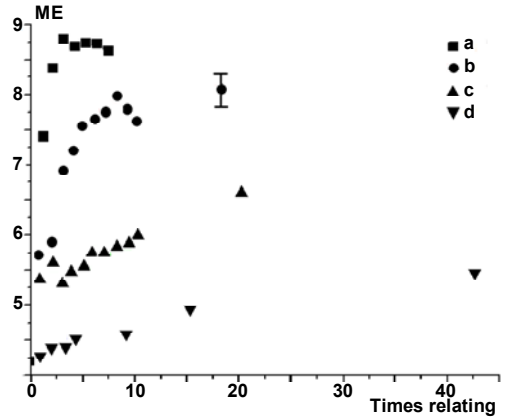

Fig. 6. Dependence of method efficiency on relation for new ANN training time and time required ANN training for ANN with various neurons' quantity in layers: a) 64; b) 100; c) 144; d) 256

As can be observed from figure 6, great dependency is absent. Therefore, we chose a half time division for next researches.

Dependence of improvement of ANN training error on quantity of neurons in layers is researched. For that purposes, we trained ANNs with common back-propagation algorithm, with our modified algorithm and with next modification of common algorithm, while synaptic weight modifications were two times during training time. In that case, firstly, we were training ANN with layers' size divided on eight during third part of all training time. Afterwards, we built ANN with layers' size divided on four based on previous ANN and were training it during another third part of all training time. And finally, we built the required ANN and were training it during last third part of all training time.

A great reduction of ANN's training error is there. Based on fig. 7, dependence of method efficiency on neurons' quantity in ANN's layer was built.

One can see, after certain neurons' quantity in layers the method efficiency is decreased (case a) on fig.8). That explained as we built required ANN from untrained previous smaller ANN.

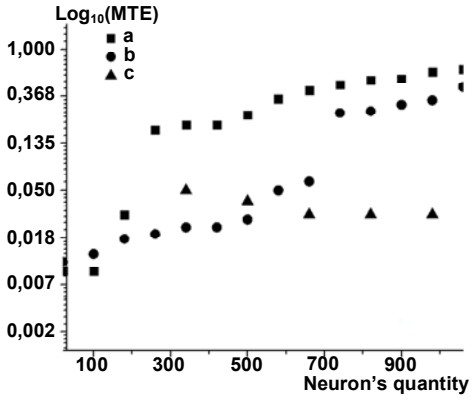

Fig. 7. Dependence of ANN's training error after training on training algorithm: a) back-propagation algorithm; b) modified back-propagation algorithm; c) modified back-propagation algorithm with double synaptic weight modifications

This effect can be avoided while use modified algorithm with double synaptic weight modifications as you can see on fig.8 b). Nevertheless, all improvement of ANN's training error is more than once.

Conclusions. This method of modifying a common back-propagation algorithm could in 8–10 times accelerate a process of ANN's training for each implementation. Method is suitable for training feed-forward multilayer ANNs with infinite number of training samples as shown on previous cases. But at the same time, there are small ANNs, where this acceleration is minimal.

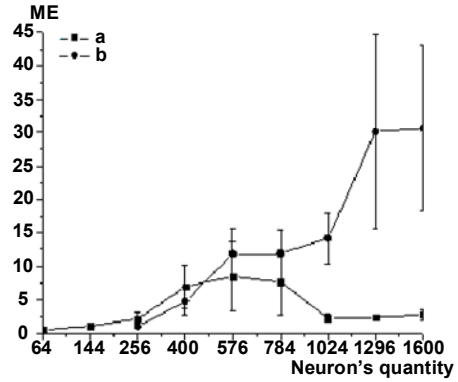

Fig.8. Dependence of method efficiency on neuron quantity in ANN's layer for: a) modified back-propagation algorithm; b) modified back-propagation algorithm with double synaptic weight modifications

1. *Alpaydin E.* GAL: Networks that grow when they learn and shrink when they forget // International Journal of Pattern Recognition. – 1994. – Vol. 8, № 1. – P. 391–414. 2. *Baum E., Haussler D.* What size net gives valid generalization? // Neural Computation. – 1989. – Vol. 1, № 1. – P. 151–160. 3. *Battiti R.* Accelerated back-propagation learning: Two Optimization Methods // Complex Systems. – 1989. – Vol. 3. – P. 331–342. 4. *Chakraborty G.* A growing network that optimizes between undertraining and overtraining // IEEE conference on Neural Networks. – 1995. – Vol. 2. – P. 1116–1120. 5. *Haykin S.* Neural Networks: A Comprehensive Foundation. – NJ, USA, 1998. 6. *Lang D.* Deep-level transient spectroscopy: A new method to characterize traps in semiconductors // Journal of Applied Physics. – 1974. – Vol. 45, № 7. – P. 3023–3032. 7. *Langfeld R.* A new method of analysis of DLTS-spectra // Applied Physics. –1987. – Vol. 44, № 2. – P. 107–110. 8. *Vinod V., Ghoso S.* Growing non-uniform feed-forward networks for continuous mappings // Neurocomputing. – 1996. – Vol. 10, № 1. – P. 55–69. 9. *Wasserman Ph.* Neural Computing: Theory and Practice. – NC, USA, 1989. 10. *Yu X.H., Chen G.A.* Efficient backpropagation learning using optimal learning rate and momentum // Neural Network. – 1997. – Vol. 10, № 3. – P. 517–527.

Submitted on 09.10.12

UDC 539.951

B. Kosarevych, stud., M. Soloviova, Ph.D., I. Anisimov, Doct. Sci.

SIMULATION OF INITIAL STAGE OF THE BEAM-PLASMA DISCHARGE IN HELIUM VIA PIC METHOD

Досліджено початкову стадію розвитку плазмово-пучкового розряду (ППР) у гелії шляхом одновимірного комп'ютерного моделювання методом макрочастинок. В залежності від густини струму пучка та тиску газу у системі виявлено три характерних режими: відсутність загоряння розряду; запалювання розряду, що не супроводжується помітним зростанням густини плазми; "регулярний" режим ППР, що супроводжується суттєвим зростанням густини фонової плазми.

Ключові слова: плазмово-пучковий розряд, плазмово-пучкова нестійкість, моделювання методом макрочастинок.

Initial stage of the beam-plasma discharge (BPD) in Helium was studied using 1D simulation via particle-in-cell method. Several regimes were observed and described depend on ranges of beam current density and gas pressure: absence of BPD ignition, BPD ignition that doesn't move to the substantional increase of the plasma density; "regular" BPD mode with the strong growth of the background plasma density.

Keywords: beam-plasma discharge, beam-plasma instability, particle-in-cell simulation.

Introduction. The recent interest to the beam-plasma discharge (BPD) is caused by its possible practical application. BPD as well as other types of discharges can be a source of non-equilibrium plasma. Its electron temperature can reach ~10^1 eV [15]. So BPD can be used for carrying out plasma-chemical reactions with the energy threshold [3, 10]. Deposition technologies, including chemical vapor deposition (CVD) and plasma enhanced CVD (PECVD) can be based on BPD. In this case plasma ions are accelerated by external potential and bombard the substrate.

For technological purposes it is necessary to manage plasma parameters easy. BPD plasma parameters can be varied by changing electron beam current or accelerating voltage.

At low current densities of the beam BPD is not realized, only electron beam focusing by ions takes place [20]. At high pressures BPD also is not realized, because the mean free path of the beam electrons is much smaller than the length of the system.

Ignition of the BPD is connected with the development of beam-plasma instability (BPI). Theoretically BPI was predicted by A. Akhiezer and Ya. Fainberg and D. Bohm and E. Gross [1, 16]. BPD was discovered by Ya. Fainberg and his staff (1960) initially in the magnetic field, and a year later – without a magnetic field. Similar research was carried out in the U.S.A. [7].

BPD was discovered 50 years ago, many works related to BPD were carried out. Most of them are experimental [11, 4, 14, 9, 18, 17]. The first attempts to describe BPD theoretically were made by Ya. Fainberg et. al. [12, 6]. In [12] only temporal dynamics of the plasma density and electron temperature were calculated. The spatial dynamics of the system was not studied.

The analytical BPD theory [15] describes its development only in general terms. BPI and ionization of background plasma by excited HF field are not considered self-consistently. However, the plasma density variation in time and space, the dependence of cross sections on interaction energy doesn't allow BPD analytical description. Full description can be done only using computer simulation [8, 5, 21, 19].

The aim of this work is simulation of the BPD initial stage in helium for various current densities of the electron beam (100÷2000 A/m^2) and gas pressures (10^{-3}÷0.1 Torr).

For these cases it's necessary to analyze the degree of ionization of neutral gas in the later stages of simulation, to investigate the conditions under which intense electric field is excited in the system and how this field affects the process of ionization of neutral gas.

Model description and simulation parameters. BPD ignition is caused by the electron beam injection into neutral or partially ionized gas. In the first case plasma initially appears due to ionization of neutral gas by electron impact.

Usually the electron beam is weak. The beam electron density is much less than the initial background plasma density.

One-dimensional package PDP1 [2] is used for simulation of the BPD initial stage. Electron beam is injected into the interelectrode space filled by the partially ionized plasma. The package deals with three kinds of particles, i.e. beam electrons, plasma electrons and ions. Neutral gas is taken into account as background, and its pressure is given. The number of real particles in a large macroparticle were chosen so that the total number of macroparticles of each kind was about $2.5\cdot10^5$. As the beam electron density is much smaller than plasma density, the specific kind of particles corresponds to the beam electrons. Maxwellian velocity distribution can be initially set for each kind of particles.

The package deals with the following elementary processes: elastic electron-neutral collisions, neutrals' excitation and ionization by electron impact. Cross sections of these processes depend on energy and are approximated by the curve shown in Fig. 1, parameters of the approximation are given in table 1.

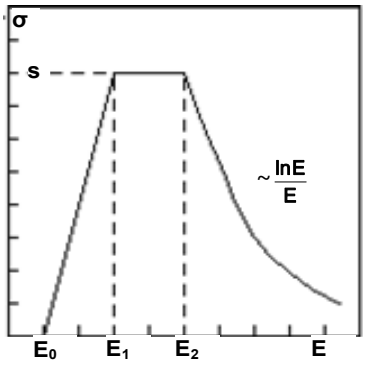

Fig. 1. Approximation of the cross section dependence on the electron energy

Interaction of electrons with neutral gas is taken into account only for plasma electrons. Thus, the electron beam interaction with plasma takes place only due to excitation of HF electric field.

Simulation parameters are taken close to experimental values [20]. Main simulation parameters are given in table 2.

Initially the gas is partially ionized. The ionization degree is in the range of $3\cdot10^{-4}$÷$3\cdot10^{-7}$. The interelectrode space contains $2\cdot10^4$ cells, so the cell length Δx=0.005 cm, and the condition $\Delta x<r_D$ is performed satisfactorily. The period of plasma oscillations $T_{pe}=10^{-9}$ s. However, the time step is chosen $\Delta t\approx\Delta x/v_b\approx10^{-12}s$, where the beam velocity v_b corresponds to the energy 5 keV.

Table 1

Parameters of the cross section of the interaction of plasma electrons with neutral atoms

Process	s (10^{-20} m^2)	E_0 (eV)	E_1 (eV)	E_2 (eV)
Elastic collisions	4	0	3	30
Excitation	0,043	19,7	20,5	21,5
Ionization	0,2	24,6	59	400

Table 2

Simulation parameters

Gas type and pressure p (Torr)	He, 10^{-3},10^{-2}, 0.1
Gas temperature T (eV)	0,025
Interelectrode length L (m)	1
Initial plasma density n_{e0} (cm^{-3})	10^{10}
Plasma electron temperature T_{e0} (eV)	1
Debye length r_D (cm)	0,01
Period of the Langmuir oscillations	$1\cdot10^{-9}$ s
Current density j_b (10^2 A/m^2)	1, 2, 5, 10, 20
Acceleration voltage U_a (V)	5000
Electron beam density n_b (10^7 cm^{-3})	1.5, 3.0, 7.5, 15,30
Time of beam flight in a system (s)	$2.4\cdot10^{-8}$
Number of cells	$2\cdot10^4$
Time step (s)	$1\cdot10^{-12}$
The characteristic simulation time (s)	$0{,}8\cdot10^{-7}$÷$1{,}0\cdot10^{-7}$

Simulation results. Development of the beam-plasma instability does not lead to ignition of the discharge at low pressures and moderate beam current densities. The mean free path of plasma electrons (80 cm) is comparable with the system length (1 m) at the pressure $1\cdot10^{-3}$ Torr. Phase portrait of electrons, spatial distributions of electric field and plasma electron density are shown in Fig. 2 for this case. The background plasma density doesn't increase substantially. The similar behavior takes place for all current densities at the pressure $1\cdot10^{-3}$ Torr and current densities less than 500 A/m^2 at the pressure $1\cdot10^{-2}$ Torr. Oscillations of the plasma electrons at plasma frequency are visible in this regime. They indicate that the frequency of electrons' collisions with heavy particles is low. The spatial distribution of the electric field has the same frequency.

The background plasma density relative increase is tens of percent for current densities $j_b \geq 500$ A/m^2 at the pressure 10^{-2} Torr and current densities $j_b \leq 1000$ A/m^2 at the pressure 10^{-1} Torr. Typical spatial distributions of electric field, plasma density and the phase portrait for electrons in this regime are shown in Fig. 3. The flow of beam electrons reflected from the collector can be seen in the phase portrait for current densities 500 A/m^2 at the pressure 10^{-2} Torr (see Fig. 3 a). This effect can be caused by the beam space charge, that is not compensated without appreciable ionization of neutral gas.

The heating of plasma electrons depends strongly on distance from the injector. The electron plasma temperature gradually decreases for larger distances. This decrease of a temperature occurs when the majority of beam electrons are notably decelerated (upper part of Fig. 3 a). The noticeable background plasma ionization occurs in the area where heating of background plasma electrons is significant. This corresponds to well-known ideas about the mechanism of the BPD through the heating of the electrons of background plasma by HF BPI field. The spatial growth rate of BPI is significantly decreased in the area where the background

plasma becomes inhomogeneous along the beam path (compare with Fig. 2).

The background plasma density increase is larger than its initial value for current densities $j_b \geq 500$ A/m^2 at the pressure 0.1 Torr. Typical spatial distributions of electric field, plasma density and the phase portrait for electrons in this regime are shown in Fig. 4. There is a back flow of beam electrons in the phase portrait. It corresponds to the formation of the virtual cathode. The frequency of the most intensive electric field is smaller in comparison with similar distributions in Figs. 2–3. Significant gas ionization by plasma electrons takes place for this case. The period $\lambda_b=V_b/\omega_{pe}$ of the wave resonance excitation is reduced because plasma density increases. The largest pressure 0.1 Torr corresponds to this regime, so the free path of particles in gas is the least. Excitation and ionization of neutral atoms becomes essential. Ionization takes place in all the interelectrode space.

The maximum plasma electron density at the time point 10^{-7} s in 7 times larger than its initial value. Obviously, ionization will be continued later and number of plasma electrons and ions will be increased in time. In practice this process is apparently limited by plasma diffusion in the transversal direction, recombination and reducing of the neutral atoms' number.

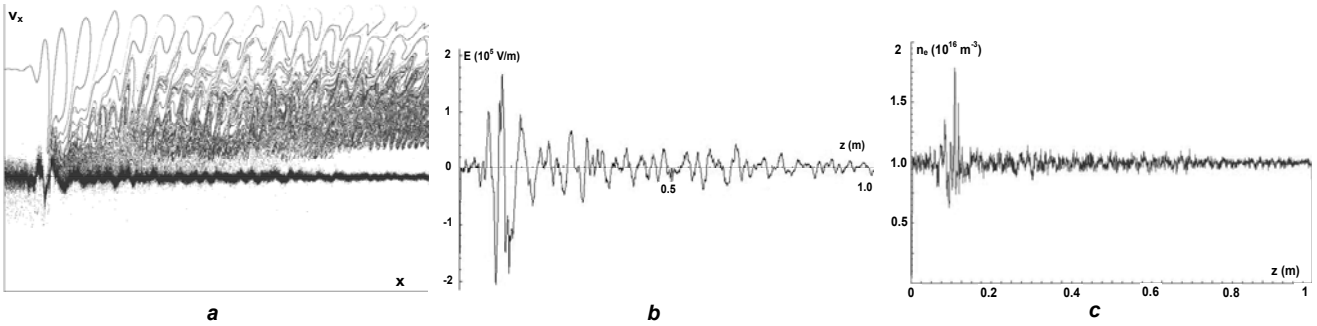

a *b* *c*

Fig. 2. Phase portrait of the beam electrons (top) and plasma (a), spatial distributions of electric field (b) and background plasma electron density (c) for the time moment t=10^{-7} s, the beam current density 200 A/m^2 and neutral gas pressure 10^{-3} Torr

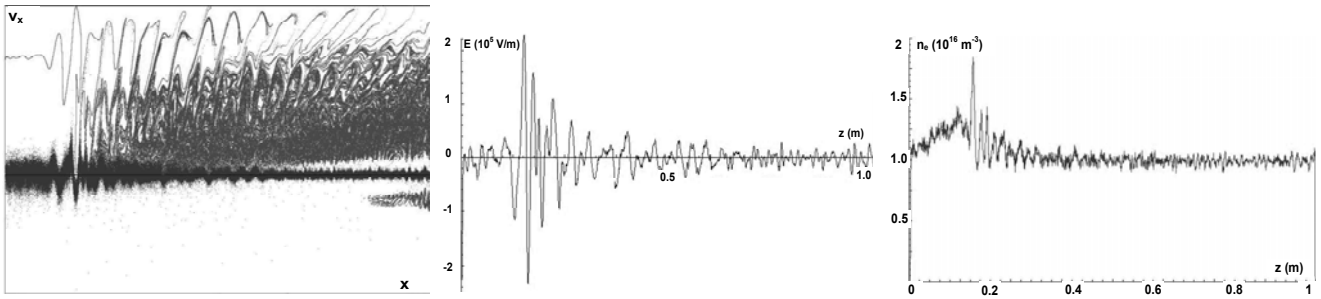

a *b* *c*

Fig. 3. Phase portrait of the beam electrons (top) and plasma (a), spatial distributions of electric field (b) and background plasma electron density (c) for the time moment 10^{-7}s, the beam current density 500 A/m^2 and neutral gas pressure 10^{-2} Torr

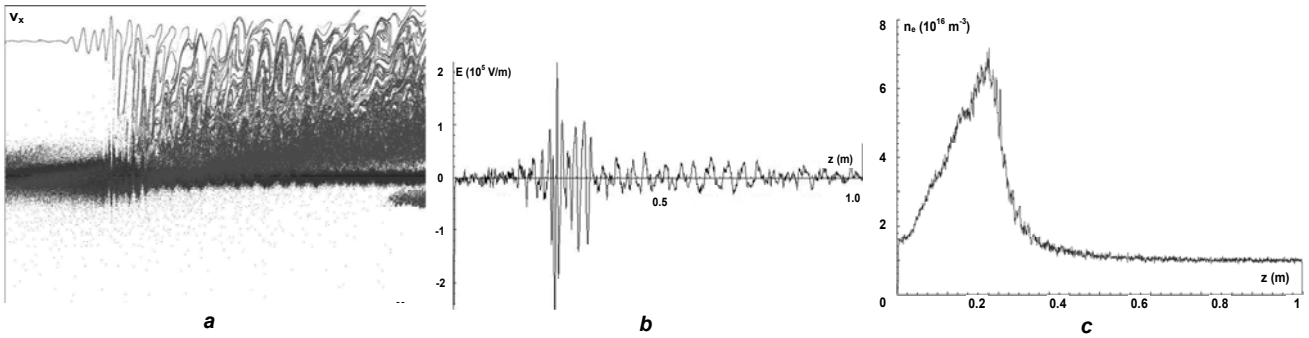

a *b* *c*

Fig. 4. Phase portrait of the beam electrons (top) and plasma (a), spatial distributions of electric field (b) and background plasma electron density (c) for the time moment 10^{-7}s, the beam current density 1000 A/m^2 and neutral gas pressure 0.1 Torr

The spatial-temporal dynamics of the main system characteristics is presented in Fig. 5. The current and pressure correspond to the boundary between regimes of the moderate and strong ionization. Time of simulation is four times larger than the electron beam flight time between electrodes and is equal to 100 electron plasma periods. The electron beam density distribution is shown in Fig. 5 a. Dark areas correspond to the propagation of electron bunches, their slope is determined by the beam velocity. Electron beam in the left part of space is homogeneous and monokinetic. The beam homogeneity breaks down as a result of BPI development in the right half space. Beam is modulated by density, and bunches are formed. However, these bunches decay later due to the mixing. The HF elec-

tric field is excited in the same area (Fig. 5 b). Average electron beam density is correlated with the distribution of electric field due to the bunch interaction with potential wave.

The most intensive electric field occurs near the middle of the system closer to the right electrode. This field assists plasma heating and gas ionization. However, plasma density increases due to ionization, and Cherenkov resonance condition breaks. This leads to the gradual shift of the region of maximum electric field and ionization to the right (Fig. 5 b). One can see few maxima at the final plasma density distribution (Fig. 5 d). From Fig. 5 a it is clear that the first maximum is formed earlier (approximately at t = 25 ns). It can be associated with the first splash of the electric field in Fig. 5 b, which is observed at t = 10-30 ns. Next maximums formation occur in the area where the field periodically reaches its maximum, starting from t = 40 ns.

The program does not take into account the plasma diffusion in the transverse direction and its recombination. So the plasma density at each point in space only increases in time.

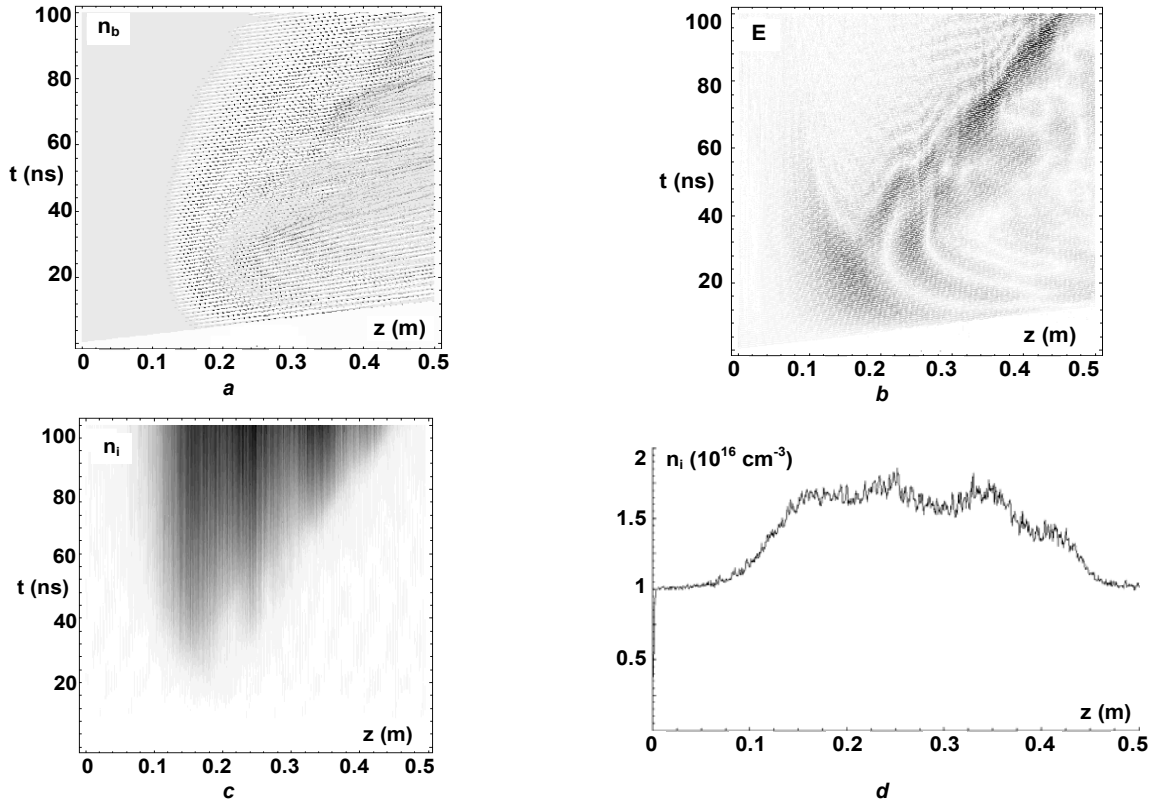

Fig. 5. Space-time dependence of the beam electron density (a), electric field (b), plasma ion density (c) and spatial distribution of plasma ion density for the time moment $1.1 \cdot 10^{-7}$ s (d), the beam current density 200 A/m^2 and neutral gas pressure 0.1 Torr

Conclusions. Simulation of the initial stage of BPD in helium was carried out for beam current densities 100, 200, 500, 1000 A/m^2, and neutral gas pressures 10^{-3},10^{-2}, 0.1 Torr.

Spatial and temporal dependencies of electron and ion plasma densities, beam electron density and electric field for the simulation time corresponding to 100 periods of electron plasma oscillations were analyzed. Ions in the phase portrait appear stationary, because the simulation time is equal to the ion oscillation period. Thus, distribution of plasma ions is similar to the intensity of ionization processes in space. The distribution of plasma electrons almost repeats the distribution of ions, but electrons feel electric field better. The frequency of the plasma electrons distribution corresponds to the frequency of the electric field.

According to the results of the simulation there are 3 typical regimes of the beam interaction with weakly ionized plasma.

At low pressures BPI is developed, beam is modulated by excited BPI HF field. However, additional gas ionization is not observed as the mean free path of electrons in a neutral gas is comparable to the system length.

At higher pressures mean free path decreases. As a result, BPD ignites. However, the increase of the degree of the gas ionization does not exceed its initial value.

At high current densities and higher pressures gas ionization is significant. Plasma density can exceed an order of the initial background value. In this mode ionization of the background plasma first starts closer to the left electrode. But variation of the background plasma density leads to moving of BPI from this area. Consequently, the area of intense electric field and intense gas ionization moves away from the injector. Therefore, the final distribution of plasma density can be non-monotonous.

In further research it would be interesting to consider the collision of beam electrons with neutral atoms and recombination processes in the background plasma, as well as to explore the possibility of stationary regime. It would also be interesting to consider 2D and 3D system geometry.

1. *Akhiezer A.Y., Fainberg Ya.B.* On the interaction of the beam particles with electron plasma // Reports of the AN USSR. – 1949. – Vol. 69, № 4. – P. 555–556. 2. *Anisimov I.O., Blazhko I.A., Siversky T.V.* Modified PDP1 package for beam-plasma systems simulation. // Proc. 2nd Int. Young Scientists Conf. on Applied Physics. T. Shevchenko National University of Kyiv, Faculty of Radiophysics. – 2002. – P. 6–7. 3. Experimental investigation of the beam-plasma discharge on purpose for holding the plasma-chemical reactions. *Atamanov V.M., Zhuzhunashvyly A.Y., Krashenynnykov S.Y. et al.* // Plasma physics. – 1979. – Vol. 5, № 1. – P. 204–210. 4. Collective interaction of intense electronic beams with plasma. I. Appearance and development of the beam-plasma discharge. *Berezyn A.K., Lyfshyts E.V., Fainberg Ya.B. et al.* // Plasma physics.– 1995. –

Vol. 21,№ 3. – P. 226–240. 5. *Birdsall Ch., Langdon A.* Plasma Physics and Numerical Simulation, trans. from English. – Moscow, 1989. 6. A nonstationary beam-plasma discharge. I. Mathematical model and linear theory. *Blioh Yu.P., Lyubarsky M.G., Podobinsky V.O. et al.* // Plasma Physics - 2003. – Vol. 29, № 9. – P. 801–808. 7. *Getty W.D., Smullin L.D.* Beam-Plasma Discharge of Oscillations // Journal of Applied Physics. – December, 1963. – Vol. 34, № 12. – P. 3421–3429. 8. The development kinetics of the initial stage of the beam-plasma discharge. *Guseva G.I., Dmitriev K.K., Zavyalov M.A. et al.* // Plasma Physics – 1987. – Vol. 13, № 3. – P. 366–369. 9. *Ivanov A.A., Leyman V.G.* About ignition of the beam-plasma discharge by powerful electron beam in a gas of high density // Plasma physics. – 1977. – Vol. 3,№ 4. – P. 780–785. 10. *Ivanov A.A., Soboleva T.K., Yushmanov P.N.* Perspectives of plasma-beam discharge application in plasma-chemistry. // Plasma physics. – 1977. – Vol. 3, № 1. – P. 152–162. 11. *Kochmarev L.Yu., Chmyl A.Y., Shustyn E.H.* About the structure and generation mechanism HF fluctuations in the beam-plasma discharge // Plasma physics. – 1995. – Vol. 21, № 3. – P. 257–266. 12. The theory of the beam-plasma discharge. *Lebedev I.M., Onischenko I.N., Tkach Yu.V. et al.* // Plasma Physics. – 1976. – Vol. 2, № 3. – P. 407–413. 13. *Levitsky S.M.* Collection of problems and calculations of physical electronics. Kyiv University Publishing, 1964. 14. Beam-plasma discharge with an electron beam injection into rarefied gas. *Meshkov I.N., Nagaytsev S.S., Seleznev I.A. et al.* – Novosibirsk Preprint 90–12, 1990. 15. *Myshyn E.V., Ruzhyn Yu.Ya., Telehyn V.A.* Interaction of electronic flows with ionospheric plasma. – Leningrad, 1989. 16. *Nezlyn J.W.* Instability of the beam charged particles in plasma. // UFN. – 1970. – Vol. 102, № 1. – P. 105–139. 17. *Serov A.A.* Relaxation of the electron beam in an inhomogeneous plasma in stationary beam-plasma discharge at the moderate low pressure // Plasma physics. – 2009. – Vol. 35, № 7. – P. 624–635. 18. *Skibenko E.I.* Beam-plasma discharge in a dense gas and strong magnetic field, its features and possible applications. // PAST. Series: Plasma electronics and new methods of acceleration (7). – 2010. – № 4. – P. 219–225. 19. *Tarakanov V.P., Shustin E.G.* Dynamics of beam instability in a bounded plasma space: numerical experiment // Plasma Physics. – 2007. – Vol. 33, № 2. – P. 151–158. 20. *Tutyk V.A.* Research of mode plasma-beam discharge by operation of the gas discharge electronic gun // Problems of atomic science and technology. Plasma Electronics and New Methods of Acceleration.. – 2008. – № 4. – P. 184–188. 21. Simultaneous Potential and Circuit Solution for 1D bounded Plasma Particle Simulation Codes. *Verboncoeur J.P., Alves M.V., Vahedi V. et al.* // J. Comp. Physics. – 1993. – № 104. – P. 321–328.

Submitted on 01.06.12

UDC 537.6/.8

G. Melkov, Dr.Sci., D. Slobodianiuk, post grad. stud.

PARAMETRICAL AMPLIFICATION OF WIDE-FREQUENCY SIGNAL IN MULTIMODE SYSTEM

В роботі аналітично та числовими методами досліджено задачу про параметричне підсилення широкосмугового сигналу в мультимодовій системі. Показано що наявність інших мод призводить до подавлення сигналу та обмежує його тривалість та затримку.

Ключові слова: Паралельна накачка, параметричне підсилення, S-теорія.

Analytically and numerically analyzed parametrical amplification of wide-frequency signal in multimode system. It was shown that presencence of other mods leads to signal suppression and limits its duration and delay.

Key words: Paralel pumping, parametrical amplification, S-theory.

Introduction. Problem of interaction between strong electromagnetic fields and ferromagnetic samples has attracted a lot of attention in past years. Processes that take place in such cases can be used for creation of wide range number of devices for signal processing and storage. Nonlinearity of Landau-Livshits equation brings a whole new "bunch" of different nonlinear effects at high power levels in ferromagnetic [2,4]. There influence on signal dynamics can be essential and cannot be neglected in some cases.

In [7] Schlömann E., Green J.J., and Milano U. detected threshold absorption of electromagnetic energy by the ferromagnetic sample in varying external magnetic field parallel to constant external magnetic field. This effect is caused by spin-waves instability under external electromagnetic pumping, so-called parametric excitation under parallel pumping. It is clear that such proceses increase amplitude of spin-waves which take energy from external source.

Such processes must satisfy both momentum and energy conservation laws [2] which can be written in a form

$$\begin{aligned} \omega_p &= \omega_1 + \omega_2 \\ k_p &= k_1 + k_2 \end{aligned} \qquad (1)$$

where ω_p, k_p are frequency and wave vector of the electromagnetic pumping respectively and $\omega_i, k_i, i = 1,2$ are frequency and wave vectors of spin-waves. For electromagnetic pumping we can assume $k_p = 0$ and therefore $k_1 = -k_2$ - so amplified spin waves has opposite wave-vectors.

It should be mentioned here that in general case conditions (1) can be satisfied not for only one pair of spin-waves but for a numerous pairs having degenerate frequency. Thus electromagnetic pumping will interact with all spin-waves satisfying condition (1), so all spin-waves satisfying mentioned conditions will grow exponentially. At the later stages of evolution nonlinear processes including interaction between amplified spin-waves must be taken into account. This can be done in a framework of so-called S-theory [4].

For simplicity we assume that only two pairs of spin-waves are excited in our system. First one is so-called signal group, having relaxation parameter Γ_1. The origin of this group can be for example external generator which excites spin-waves in a sample. Wave vectors of this group are relatively small and are about $k_1 \sim \frac{2\pi}{a}$ [2] where a – is antenna thickness used for excitation spin-waves in our sample. The second spin-wave group will be called dominant, having much larger wave vectors $k_2 \sim 10^4 sm^{-1}$ and lower dissipation rate than signal group $\Gamma_2 < \Gamma_1$. This is caused by numerous reasons: smaller group velocities and smaller influence of two-magnon scattering processes are the key reasons.

The goal of this work it to analyze processes of wide-range signal amplification under parametric pumping in multimode case.

Theory. For description of magnon system under the influence of parametric pumping S-theory approach is used. Description of amplified by means of parametrical pumping single spin-wave package can be done using following integro-differential equation:

$$\begin{aligned} -\frac{1}{f}\frac{df}{dt} = x^2 + x(2\alpha - 1)(\int f dx' - 1) + \\ +\alpha \int f dx' - \alpha + (\int f dx' - 1)^2 \alpha^2 + \int x' f dx' \end{aligned} \qquad (2)$$

where f denotes spin-wave package distribution function, x – generalized detuning from half-pumping frequency and α – parameter of nonlinearity. Equation (2) was obtained

in work [3] where asymptotical solution was found. It was shown that with time increasing distribution function profile tends to Dirac δ like profile with its maximum depending on detuning and nonlinearity parameters. At moderate stage distribution profile has Gauss-like shape.

Recalling multimode nature of our system, mentioned in introduction we should solve simultaneously two equation for f_1 and f_2 - signal and dominant groups. However analytical analysis of such system will be almost impossible. The solution is to use so-called "method of lines" [6] that will allow us to reduce equation (2) to a system of ordinary differential equation.

This reduction require introduction of one more parameter N number of equations we will use in our calculation. Problem of estimation optimum number of equation will be discussed later.

System of equation describing spin-wave system consisting of two groups dominate and signal under influence of parametrical pumping will have a form [2,4]:

$$\begin{aligned} &\frac{1}{2}\frac{dn_j}{dt} = n_k\left[-\Gamma_j + \mathrm{Im}\left[P_j^* e^{-i\psi_j}\right]\right] \\ &\frac{1}{2}\frac{d\psi_j}{dt} = \Omega_j + \mathrm{Re}\left[P_j^* e^{-i\psi_j}\right] \\ &P_j = hV_p + \sum_{j'} S_{jj'} n_{j'} e^{-i\psi_{j'}} \\ &\Omega_j = \omega_j - \frac{\omega_p}{2} + 2\sum_{j'} T_{jj'} n_{j'} \end{aligned} \qquad (3)$$

Spin-wave group evolution is described using group amplitude and phases n_j, ψ_j. Multiindex $j = (j_1, j_2 \ldots j_N)$ was introduced enumerating both number of equation in sets of N equations for each spin-wave group and enumerating type of spin-wave group: $j = 1$ for signal group and $j = 2$ for dominant group. Summation is carried over both types on indexes. S, T – are parameters of nonlinearity [4].

Assuming equal detuning $\Delta\omega = \omega_j - \omega_p/2$ between j_i and j_{i+1} equations and taking into account that parametrical pumping effectively amplifies signals in frequency band given by expression $\Omega_p = \sqrt{hV_p^2 - \Gamma^2}$ we obtain needed number of equations for desired detuning between equations which is:

$$N = \sqrt{hV_p^2 - \Gamma^2} \Big/ \left(\omega_j - \frac{\omega_p}{2}\right) \qquad (4)$$

Next problem is choosing initial conditions for amplitudes and phases of both groups. Due to thermal fluctuations spin-wave amplitudes in a sample always have a nonzero "thermal" level. It estimation was done in a work [5] and is about $n_0 = 10^{13} sm^{-3}$ which we will use in our calculation. However such estimation is valid only for dominated spin-wave group. Generally speaking amplitude of signal group, which is set by output generator can be ten times larger than "thermal" level. So in our calculation we will use the following expression for starting signal amplitude $n_1(0) = A_0 n_0$, where parameter $A_0 > 1$ is amplitude of signal group above "thermal" level.

Lets analyze system dynamics qualitively. At first stages of evolution both signal and dominant group will begin to grow exponentially according to their dissipation parameters:

$$\begin{aligned} &n_1(t) = A_0 n_0 Exp\left(hV_p - \Gamma_1\right) \\ &n_2(t) = n_0 Exp\left(hV_p - \Gamma_2\right) \end{aligned} \qquad (5)$$

Nonlinear effects will become significant at the time $t_1 = \frac{\ln A_0}{\Gamma_1 - \Gamma_2}$ when both groups amplitudes will become equal. At later stages according to S-theory only group with smaller dissipation will remain and all other groups will be suppressed. In our case dominant group will remain and signal group will be suppressed. Thus output signal duration will be limited due to nonlinear interaction in our system and its multimode nature. The duration of the output signal can be estimated to be

$$\tau_s = \frac{1}{hV_p - \Gamma_2} \ln \frac{1}{Sn_0} \sqrt{\left(hV_p\right)^2 - \Gamma_2^2} \qquad (6)$$

Such results are striking. This means that output signal length in multimode system is always limited due to excitation of dominant group which according to S-theory suppresses all other groups having higher dissipation rate. This effect can be threaten like parasitic cause signal amplification is important part of analog devices based on YIG.

Numerical calculation will be carried in case of YIG films. Parameters of the system will be following $\Gamma_0 = 2\pi \cdot 0.6 MHz$, $S = 5 \cdot 10^{-13} sm^{-3} s^{-1}$ [5]. According to (4) number of equations was set to $N = 100$ for both signal and dominant group with equal detuning $\Delta\omega = 0.01 MHz$.

Main results and discussion. Results of solving equations (3) with supercriticality $\xi = h / h_{thr} = 2dB$ are shown on Fig.1. As one can see signal is focused in a narrow region with small detuning $\Delta\omega = \omega_j - \omega_p/2$, and maximum amplification is for spectral component with $\Delta\omega = 0$. Also Gauss-like signal shape is clearly seen which was predicted in [3]. The most interesting result is signal suppression at $t > 4\mu s$ caused by dominant group influence in the framework of S-theory. As it was shown above this effect plays fundamental role in signal amplification processes that take place in multimode system.

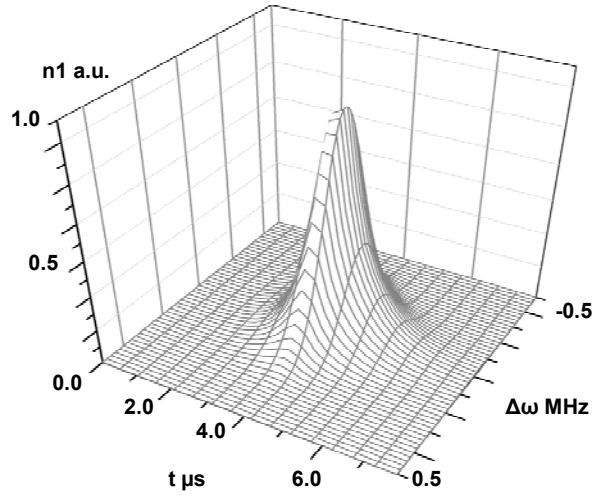

Fig. 1. Signal group evolution in time-frequency domain
$\Gamma_2 = 0.8\Gamma_1, A_0 = 3, \xi = 2dB$

For higher pumping amplitudes one can expect signal amplified frequency range increase and suppression to start earlier according to Eq. (6). Numerical solution coincides good with this predictions. Numerical solution for $\xi = 5dB$ is shown on Fig.2. It is clearly seen that in this case amplified signal frequency range is higher and suppression start earlier.

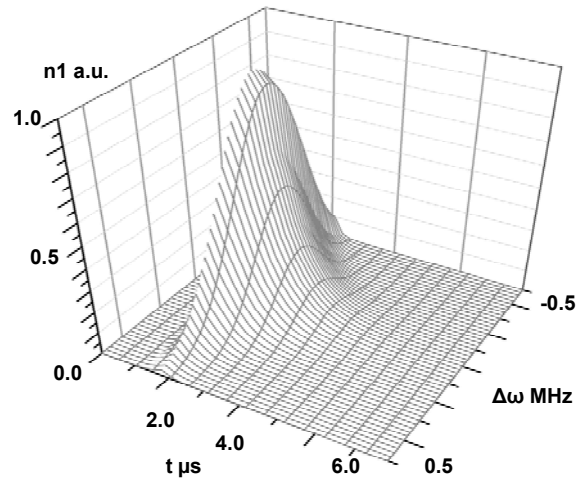

Fig. 2. Signal group evolution in time-frequency domain

$\Gamma_2 = 0.8\Gamma_1, A_0 = 3, \xi = 5dB$

Increase in amplified frequency range is obviously connected with increasing of pumping frequency band given by expression $\Omega_p = \sqrt{hV_p^2 - \Gamma^2}$.

As one can see signal suppression due to interaction between dominant and signal groups is the most significant effect that can be directly observed in multimode system. Next we will analyze dependence of signal duration and delay on pumping amplitude in such system.

Fig.3. shows results describing signal duration and delay dependence from pumping amplitude.

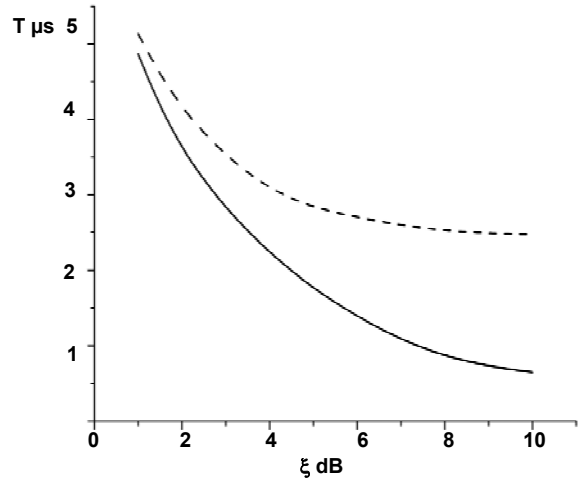

Fig. 3. The dependence of signal duration (dashed line) and delay (solid line) on the supercriticality ξ

$\Gamma_2 = 0.8\Gamma_1, A_0 = 3$

Here one can this qualitive agreement with Eq. (6), due to higher pumping amplitudes dominant groups saturates earlier thus signal delay and duration decrease. Dependence of dissipation rates between dominant and signal group is very important in this case. The smaller is dissipation of dominant group the more pronounced effect it causes on evolution of signal group.

Fig.4. shows the same dependence of signal delay and duration but for lower dissipation parameter of dominant group.

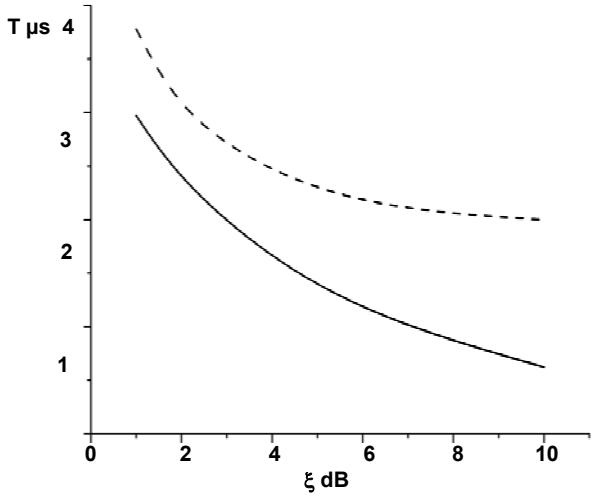

Fig. 4. The dependence of signal duration (dashed line) and delay (solid line) on the supercriticality ξ

$\Gamma_2 = 0.6\Gamma_1, A_0 = 3$

This effect can be used for nonlinear signal compression in YIG delay lines. However it should be noticed here that this require amplifying external pumping with relatively large amplitudes which can cause other nonlinear effect to arise.

Conclusion. Analytically and numerically problem of interaction of electro-magnetic pumping and spin-wave packets in multimode system was investigated. Modelling was carried in a framework of S-theory. Results show that multimode nature of the system plays important role in described proceses. Due to mentioned effect signal duration and delay is always limited and strongly on the pumping amplitude in such system. Such behavior can be used for signal compression in YIG delay lines

1. *Ахиезер А. И., Барьяхтар В. Г., Пелетминский С. В* Спиновые волны – М. 1967. 2. *Гуревич А.Г., Мелков Г.А.* Магнитные колебания и волны. – М., 1994 .3 .*Захаров В.Е, Львов В.С, Мушер С.Л.* О нестационарном поведении системы параметрически возбужденных спиновых волн // ФТТ – 1973. – Том.14, № 3. 4. *Львов В.С.* Нелинейные спиновые волны – М., 1987. 5. *Chumak A.V., Serga A.A., Hillebrands B., Melkov G.A., Tiberkevich V., Slavin A.N.* Parametrically stimulated recovery of a microwave signal using standing spin-wave modes of a magnetic film // Physical Review B. – 2009. – Vol. 79. 6. *Sarmin E.N., Chudov L.A.* On the stability of the numerical integration of systems of ordinary differential equations arising in the use of the straight line method // USSR Computational Mathematics and Mathematical Physics,– 1963 – Vol. 3(6). 7. *Schlömann E., Green J.J., and Milano U.* Recent developments in ferromagnetic resonance at high power levels // J.Appl.Phys. – 1960. – Vol. 31, №5. – P. 386.

Submitted on 07.05.12

UDC 537. 8

O. Nechyporuk, Ph.D., S. Kozban, stud.

COMPUTER SIMULATION OF MAGNETOSTATIC BACKWARD VOLUME WAVES DISPERSION IN 3-DIMENTIONAL SPACE OF WAVE NUMBERS AND FREQUENCY

Запропоновано програму для комп'ютерного моделювання дисперсії зворотних об'ємних магнітостатичних хвиль при довільному куті поширення в структурі метал-діелектрик-ферит-діелектрик метал. Отримано та проаналізовано відповідне дисперсійне співвідношення. Наводяться приклади моделювання дисперсії хвиль в тривимірному просторі хвильових чисел та частот.

Ключові слова: комп'ютерне моделювання, хвилі магнітостатичні, дисперсія.

Program for computer simulation of magnetostatic backward volume waves dispersion is proposed in the case of arbitrary angle of wave propagation in the structure metal-dielectric-ferrite-dielectric-metal. The corresponding dispersion expression is obtained and analysed. Examples of computer simulation of waves dispersion in 3-dimentional space of wave numbers and frequency are produced .

Key Words: computer simulation, magnetostatic waves, dispersion.

Introduction. Variety dispersion laws for magnetostatic waves (MSW) is widely used in the spin-wave electronics, in particular, provides the possibility of formation and processing of complex signals. The most flexible control is MSW dispersion in multilayer structures at arbitrary angle of wave propagation.

The goal is to develop programs for computer simulation of magnetostatic backward volume waves (MSBVW) dispersion in three-dimensional space of wave numbers and frequencies, which would provide a visual analysis and thus accelerated the selection of multilayer structures for specific applications. On the other hand, from the methodological point of view imaging dispersion dependences in three-dimensional space contributes to understanding the physics of the MSW and principles of devices of spin-wave electronics by students.

Development and discussion. Consider the tangent magnetized metal-dielectric-ferrite-dielectric-metal (MDFDM) structure, which is shown in Figure 1. Wave vector of MSBVW propagation $\vec{k}$ is in-plane at an angle θ related to the static external magnetic field $\vec{H}_0$ which is directed along the Z-axis. The thickness of the ferrite layer equals S, and the thickness of two dielectric layers are $-S_1$ and $S_2 - S$. The structure is not limited in the YZ plane.

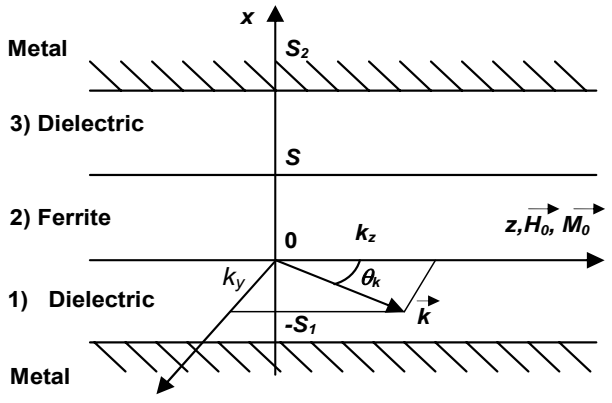

Fig. 1. Tangent magnetized of MDFDM structure

The dispersion for MSBVW in such a structure is obtained by known methods [1–2]. In the ferrite component structure of magnetostatic waves are described by Walker equation, and in dielectric layers – Laplace equation. Solutions for each of the components are searched in the form of inhomogeneous flat (with x coordinate) waves. Scalar potential must satisfy the usual boundary conditions. Such as continuity of tangential component of magnetic field on the boundary of dielectric-ferrite and normal components of magnetic induction equals to zero on the boundary of metal-dielectric (metal is ideal conductor).

As a result, we obtain the following expression:

$$\begin{aligned}&\mu\kappa k_s Ch(k_s(S-S_2))Sh(k_s S_1)\cos\kappa S+\\&+k_s^2 Ch(k_s(S-S_2))Ch(k_s S_1)\sin\kappa S+\\&+\mu_a k_y k_s Ch(k_s(S-S_2))Sh(k_s S_1)\sin\kappa S+\\&+k_s\mu_a k_y Sh(k_s(S-S_2))Ch(k_s S_1)\sin\kappa S+\\&+\mu_a^2 k_y^2 Sh(k_s(S-S_2))Sh(k_s S_1)\sin\kappa S+\\&+\mu^2\kappa^2 Sh(k_s(S-S_2))Sh(k_s S_1)\sin\kappa S-\\&-k_s\mu\kappa Sh(k_s(S-S_2))Ch(k_s S_1)\cos\kappa S=0\end{aligned} \quad (1)$$

In eq. (1) the following notations are used:

$$\begin{aligned}&Sh(k_s(S-S_2))=e^{-2k_sS_2}e^{k_sS}+e^{-k_sS};\\&Ch(k_s(S-S_2))=e^{-2k_sS_2}e^{k_sS}-e^{-k_sS};\\&Sh(k_sS_1)=1+e^{-2k_sS_1};\\&Ch(k_sS_1)=1-e^{-2k_sS_1};\end{aligned} \quad (2)$$

Also μ and μ_a are diagonal and off-diagonal components of the tensor of magnetic permeability of ferrite, κ - parameter of wave propagation in ferrites:

$$\kappa=\sqrt{-(k_y^2+\frac{k_z^2}{\mu})} \quad (3)$$

k_y, k_z are the components of the MSBVW wave vector in the plane of structure:

$$k_y = k\sin\theta,\ k_z = k\cos\theta \quad (4)$$

k_s is the parameter of wave propagation in dielectric components of the structure:

$$k_s=\sqrt{k_y^2+k_z^2} \quad (5)$$

MSBVW computer simulation. To analyze the dispersion of MSBVW in three-dimensional space of wave numbers and frequencies in the case of arbitrary angle between the directions of wave number and the external magnetic field was developed a program in an environment Microsoft Visual C# using TaoFramework and OpenGL libraries. The program's interface is shown in Figure 2. The program's interface contains the following fields: input field, graphical results output, properties of dispersion dependences area. Let's describe these fields separately.

Input field. This area is located vertically on the right side of the screen. In group "Parameters" there are following input fields: "Magnetizing Field" - set the value of the external magnetic field in the range from 0 to 6000 Oe; "Dielectric1", "Ferrite", "Dielectric2" fields - sets thickness layers of dielectric and ferrite in micrometers; "Mode Number"- specifies the number of mode in dispersion equation. Menu "Layer color" allows you to choose which color will next dispersion characteristics be displayed. Button "Modu-

late new layer" calculates value solutions of the dispersion equation and displays these values in the form of three-dimensional image in the relevant field and numeric range MSBVW existence in the display properties of dispersion dependences. Button "Clear last layer" clears the last calculated dispersion from the graphics area and field properties. Button "Clear all layers" clears the graphics area and properties. Button group "Zoom In" and "Zoom Out" can zoom in and out graphical results field, with a greater frequency range, and it is possible review dispersion characteristics for larger field values of magnetization. "Modulation Info." button shows the area that displays the properties of dispersion characteristics.

Selecting parameters thickness dielectric layers can display dispersion relations for isolated (Free Slab) and (or) metallic (Metalized Slab) ferrite layer.

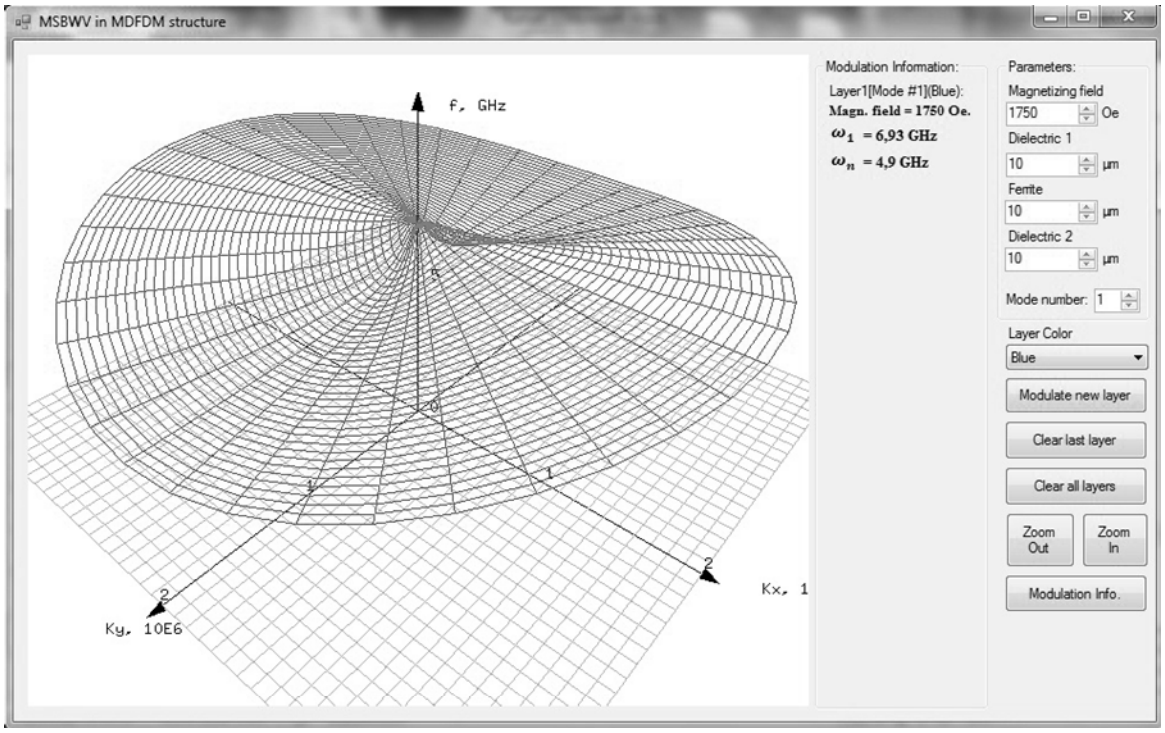

Fig. 2. The program interface for calculating the dispersion of MSBVW

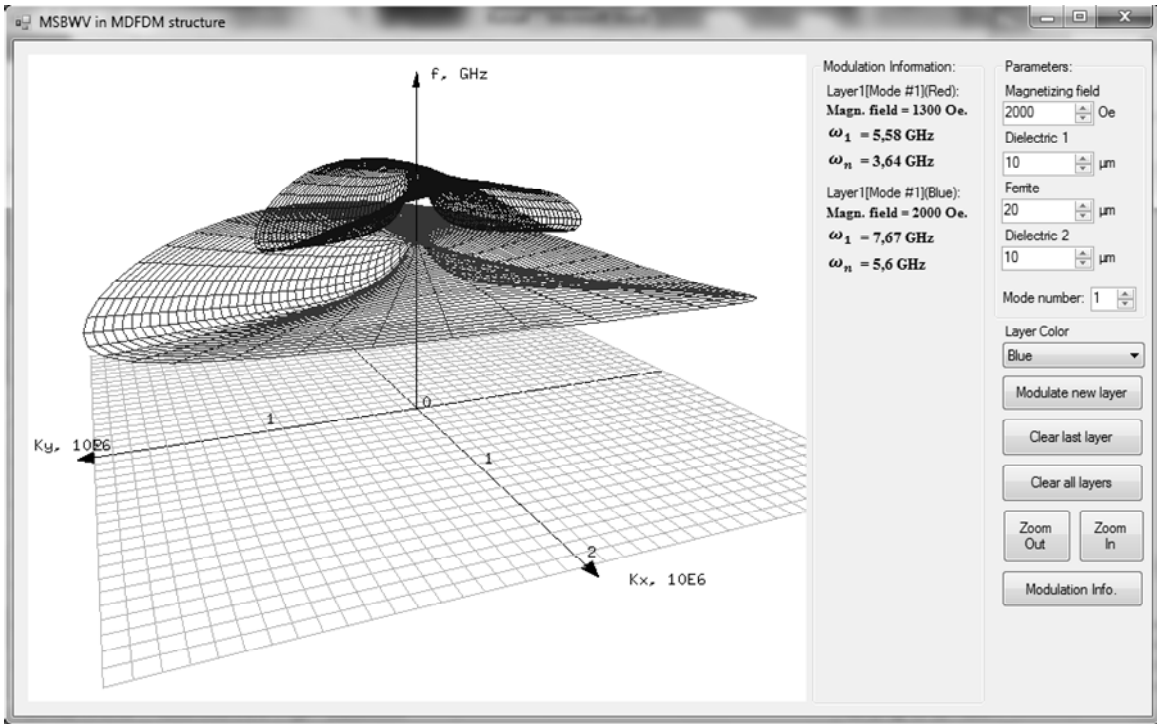

Fig. 3. Example of three-dimensional image variance MSBVW for ferrite layer thickness of 10 microns with size of magnetizing field 2000 Oe. (Black) and a thickness of ferrite layer 20 microns and the size of magnetizing field 1300 Oe (grey)

Display area graphs. In this area there is a plane (k_x, k_y), the values k_x and k_y are limited by the plane and been selected depending on the thickness of the ferrite layer. The axis of the frequencies is drawn nomal to the plane, at the center of it, the value of which will be determined according to the chosen scaling.

Three-dimensional image of the MSBVW dispersion for the selected case displays with one of five standard colors that are listed in the menu "Layer color". Maximum dispersion characteristics that can be represented is limited to five. An example of such image is shown on fig.3.

Properties of dispersion dependences area is displayed when the "Modulation Info." button is pressed, Re-pressing the button hides this area. Information about each of the dispersion dependences, (the number of mode ("Mode #"), the value of the magnetizing field, the limiting frequencies ("ω_1", "ω_H") are displayed here.

Controlling interface carried out by using the mouse and keyboard. With them, you can enter data, start the calculation process and provide image rotation along the vertical and horizontal axes.

Minimum requirements for the computers on which the installation is possible: Intel Atom 1,6 GHz processor (or analogues from other manufacturers), 256 MB RAM, VGA video card, Windows XP, availability of libraries OpenGL (opengl32. dll, glu32.dll).

Created Program for computer simulation of magnetostatic backward volume waves dispersion joined CD-ROM multimedia training courses and electronic library "Spin-wave electrodynamics and Electronics" [3]. As the experience of its use in the undergraduate and postgraduate visualization dispersion diagrams in three dimensions contributes to a deeper understanding of the physics of magnetostatic waves and principles of the devices spin-wave electronics and their application.

1. *Damon R.W., Eshbach J.R.* Magnetostatic modes of ferromagnetic slab // Journ. Phys. Chem. Solids. – 1961. – Vol. 19. – №3/4. – P. 308–320. *2. Данилов В.В., Зависляк І.В.,* Нечипорук О.Ю. Спін-хвильова електродинаміка. – Київ: Видавничо-поліграфічний центр "Київський університет", 2008, 351 р. 3. *Нечипорук О.Ю., Данилов В.В., Зависляк І.В.* Мультимедійний навчальний курс та електронна бібліотека "Спін-хвильова електродинаміка та електроніка", Київ, 2002, ISBN 1680–0249

Submitted on 18.09.12

UDC 535.42:534

O. Polishko, stud., E. Smirnov, Ph.D.

ACUSTO-OPTIC MODULATOR AND DEFLECTOR FOR NONPOLARIZED LIGHT

Досліджено акустооптичні (АО) модулятори та дефлектор для неполяризованого світла на основі парателуриту. Створено модулятор першого порядку дифракції на основі двох АО комірок, для якого досягнуто ефективність дифракції для ортогональних поляризацій 91 % та 92 %. Також створено модулятор нульового порядку дифракції, що забезпечує коефіцієнт контрастності 100:7. Розроблено акустооптичний дефлектор на основі двох АО комірок з максимальною ефективністю близько 90 % та роздільною здатністю понад 400 точок.

Ключові слова: акустооптика, акустооптичний дефлектор, акустооптичний модулятор, неполяризоване світло.

Acousto-optic (AO) deflector and modulators for nonpolarized light based on TeO_2 crystal are investigated. Double AO cells first order modulator with efficiencies for orthogonal polarised light achieve 91 % and 92 % was created. Single AO cell zero order modulator was created and compared. It provides extinction ratio 100:7. The prototype of the double AO cells deflector has been developed with maximum efficiency close to 90 % and the number of resolvable points more than 400.

Keywords: acousto-optics, acousto-optic deflector, acousto-optic modulator, nonpolarized light.

Introduction. In the majority of cases acousto-optic (AO) devices, based on paratellurite (TeO_2) crystals, work with the linearly polarized optical radiation. If such devices are used for the control of powerful nonpolarized fiber laser beams, their efficiency of diffraction are limited to 50 %. Nonpolarized radiation can be described as two waves with the linear polarization, which coincide with the optical eigenmodes of crystal. This task permits to apply anisotropic Bragg's diffraction to both of these linear polarized beams separately. To create such devices we can use several schemes described in [1] and calculated with the AO diffraction vector diagrams [2]. For creating the highest efficiency AO cells a TeO_2 monocrystal which has extremely high M_2 (AO figure of merit) was used. The indicatrix of refractive indices for uniaxial crystal with optical activity is described [3] with formula (1)

$$n_1(\theta) = n_{10}(\theta) / \sqrt{1 - n_{10}^2(\theta)\rho(\theta)G_{33}},$$
$$n_2(\theta) = n_0 / \sqrt{1 + n_0^2\rho(\theta)G_{33}}, \qquad (1)$$

where

$$n_{10}^2 = n_e^2 n_o^2 / \left(n_e^2 \cos^2\theta + n_o^2 \sin^2\theta\right),$$
$$\rho(\theta) = \left[\sqrt{\left(n_o^{-2} - n_{10}^{-2}\right)^2 + \left(2G_{33}\right)^2} - \left(n_o^{-2} - n_{10}^{-2}\right)^2\right] / 2G_{33},$$
$$G_{33} = \frac{\lambda R}{\pi n_0^3}.$$

For wavelength of light the λ=1.064 μm, n_e=2.352, n_o=2.208, R=25.5°/mm. For lights with the λ=0.63 μm, n_e=2.412, n_o=2.260, R=87°/mm.

Shear acoustic wave propagating along the direction close to [110] provides an extremely low velocity of sound (less than 700 m/s) and high figure of merit. Laser beams propagate along the direction close to [001].

Zero order modulator. Some devices with AO modulation requires to minimize losses of optical radiation. For these purposes can be use to zero order diffraction modulator, where transmitted beam is working. The principle of its operation is simultaneous AO diffraction of both orthogonal linear polarized waves by the same acoustic wave (Fig. 1).

Incident nonpolarized radiation splits into two linearly polarized beams, known as ordinary and extraordinary, describes with wave vectors k_o and k_e.

In zero order modulator anisotropic diffraction occurs on the beam k_e to first Bragg's order, and the beam k_e – to minus first order by the same shear acoustic wave K. Interaction described by a momentum conservation :

$$k_o - K = k_1,$$
$$k_e + K = k_2. \qquad (2)$$

The problem is to find the incident beam's direction when both the diffractions occur on the same acoustic wave. In the result of AO interactions intensity of transmitted beam is significantly reduced.

The frequency dependences of the Bragg's angles in the crystal with 7.9° angle between acoustic wave vector and [110] crystallographic direction are shown in Fig. 2. On the intersection of curves the both diffractions of ordinary and extraordinary polarized beam occur at the same incident angle.

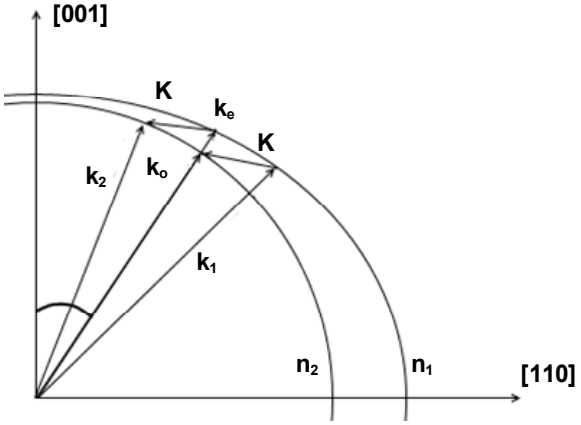

Fig. 1. Vector diagram of simultaneous interaction of orthogonal optical eigenmodes on the same slow shear acoustic wave

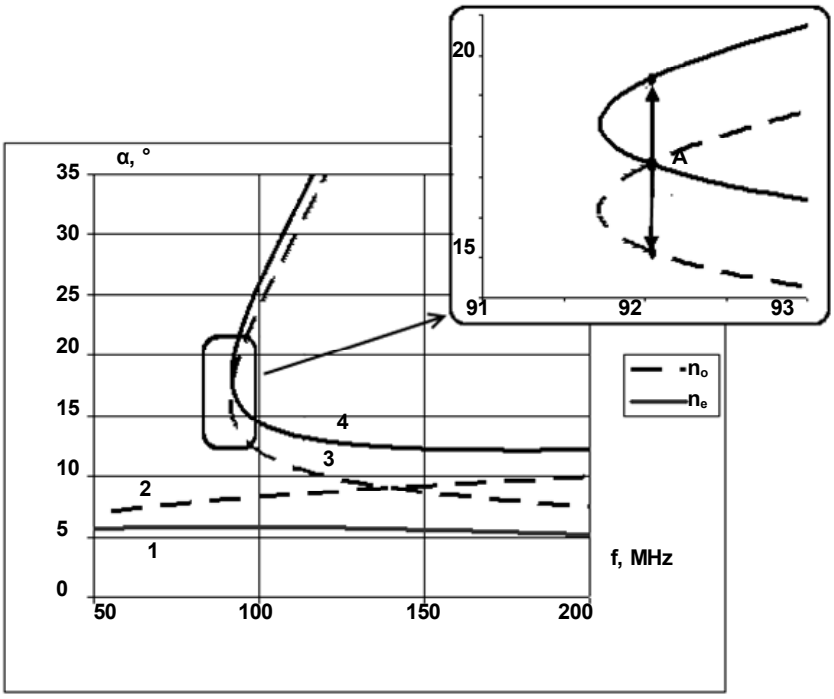

Fig. 2. Dependence of the Bragg's angle versus frequency of acoustic wave at λ =1.064 μm and 7.9° angle between wave vector of acoustic wave and [110] direction

Fig. 3. illustrates calculated dependences of acoustic wave's frequency for simultaneous diffraction both of the eigen modes, which needed to design zero order modulator, and the experimental results with different AO cells (marked with dots on Fig. 3).

Efficiency of diffraction achieved is 93 % for λ =1.063 μm at 1.9 W RF power delivered by the driver and frequency 51 MHz. The same results amount to 93% efficiency for λ =0.63 μm at 1 W RF power and frequency 92 MHz. Extinction ratio of both the experimentally studied modulators achives 100:7.

Two crystals first Bragg order modulator. If need to reach more extinction ratio we can use first Bragg order modulator. The task of creating nonpolarized AO modulator can be simplified with using typical AO deflectors.

This problem can be divided into two anisotropic AO diffraction of different incident radiation polarization. AO interaction with extraordinary polarized beam is correspond to typical deflector regime (line 1 on Fig 2) and occurs in the first AO cell.

AO difraction with extraordinary polarized beam occurs in the second AO cell with the same frequency of acoustic wave (line 2 on Fig.2). The angle between incident beam and optical axis [001] in first AO cells equal to the angle between diffracted beam and optical axis in second AO cell (Fig 4).

Therefore, the first AO cell deflects the beam to greater angle to its axis and the second AO cell deflects the beam to the lesser angle to its axis. The second AO cell must be oriented specularly with respect to incident beam, in order

to equalize both diffracted beam. The absence of re-diffraction of diffracted beam in the second AO cell is explained with unambiguous incident angle for this acoustic frequency (line 2, Fig. 2).

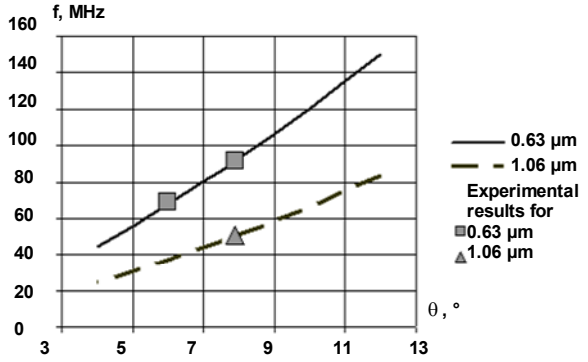

Fig. 3. Calculated dependence of the frequency acoustic wave for zero order modulation versus the angle between acoustic wave's vector and crystallographic axis [110]

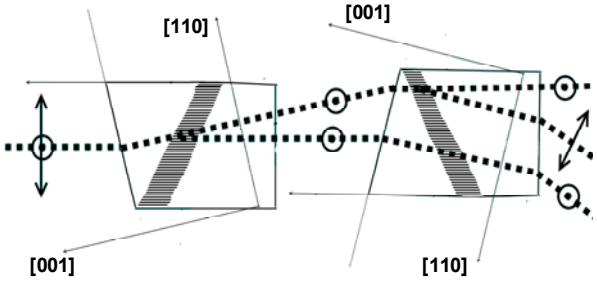

Fig. 4. Scheme of light propagation in two AO cells

91% efficiency of diffraction nonpolarized radiation is obtained by using two AOC at λ =0.63 μm and 1 W RF power delivered by the drivers and acoustic frequency 85 MHz. Intensity of zero order decreased to 7%. The difference between first order's intensity and zero order's loss of intensity is explained by re-diffraction because acoustic wave is divergent. The efficiency of diffraction is 91% for first AO cell and 92% for second AO cell.

There are other possible orientation of AO cells, such as optical axes are on one side of the incident beam, but it requires different acoustic frequencies – beams deflect at the same side (lines 1 and 3 in Fig. 2.).

Deflector for nonpolarized light. Some devices require nonpolarized beam steering, for example, machining center using infrared fiber laser. This task can be solved with AO deflection of nonpolarized light. One of the requirements for the AO deflector is the same angle of incident beam at different frequencies of acoustic waves.

It is carried out with extraordinary polarization (Fig. 2, line 1) but can not be realized (Fig. 2 line 2) with ordinary polarization.

Therefore rotation of the plane of linearly polarized light after first AO cell is necessary to provide diffraction in the second AO cell of the beam which has not been diffracted if the first AO cell. Rotation of the plane of linearly polarized light is providing with half-wave plate.(Fig. 5)

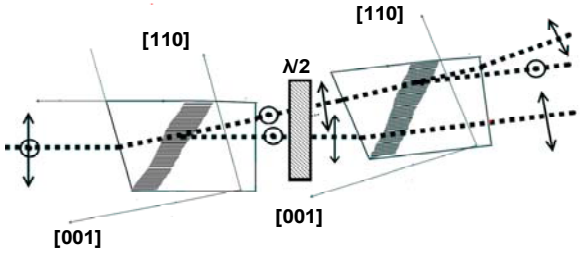

Fig. 5. Scheme of light propagation in nonpolarized light deflector (λ /2-half-wave plate)

The efficiency of diffraction in such AO deflector is achieve 90% (for λ =0.63 μm) which slightly less than AO deflector for linear polarize beam (Fig. 6).

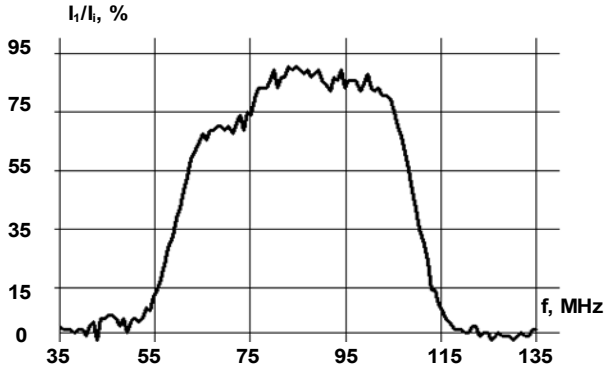

Fig. 6. Efficiency of diffraction on deflector for λ =0.63 μm power delivered by each drivers 1 W

Conclusion. Described methods allow obtain to 90–93% efficiency of diffraction for nonpolarized radiation.

This result is slightly less then AO devices which work with linear polarized radiation with the same acoustic power. Zero order modulator can be used in the instrument of control nonpolarized laser's beam, where minimum loss of light is required and low extinction ratio (100:7) is unessential. For the task where low intensity isn't unessential, first Bragg order's modulator will be better solution.

1. *Antonov S.N.* Acoustooptic Nonpolar Light Controlling Devices and Polarization Modulators Based on Paratellurite Crystals // Zh. Tekh. Fiz.- 2004. – Vol.74, №10. – P.84–89. 2. *Magdich L. N. and Molchanov V. Ya.*, Acoustooptic Devices and Their Applications. – M.: Sov. Radio, 1978. – 112 p. 3. *Tishenko T.N., Trybechkoy A.D.* Some of the questions the research and development of acousto-optic deflector for monocrystal TeO_2 // Avtometriya. – Novosibirsk.: Nauka, 1979. – P. 87–95.

Submitted 10.04.11

UDC 537.6/.8

O. Prokopenko, Ph.D., Asc. Prof., V. Malyshev, Lead Engineer,
L. Prokopenko, 1st Rank Engineer

MICROWAVE ENERGY HARVESTING USING UNCOUPLED THRESHOLD SPIN-TORQUE MICROWAVE DETECTORS

We analyze the efficiency of microwave energy harvesting using an array of uncoupled threshold spin-torque microwave detectors (STMDs). We show that the energy harvesting rate and the total output DC power are approximately linearly depend on a small number of non-interacting detectors in the array, and strongly depend on the frequency f and power P_{RF} of an input microwave signal. We calculate the phase diagram of the device's energy harvesting rate in coordinates $(f;P_{RF})$ and show that parallel arrays of STMDs have higher efficiency at lower levels of an input microwave power, while the series arrays are preferable at the higher levels of an input microwave power.

Key words: spin-torque microwave detector, threshold detector, energy harvesting.

Проаналізовано ефективність відбору енергії від сигналів НВЧ та її перетворення у енергію низькочастотних (НЧ) сигналів за допомогою масиву невзаємодіючих порогових детекторів НВЧ на основі магнітних наноструктур, керованих спін-поляризованим струмом. Показано, що ефективність такого перетворення та загальна вихідна НЧ потужність приблизно лінійно залежать від кількості детекторів у масиві за умови малої кількості детекторів, та суттєво залежать від частоти f вхідного НВЧ сигналу та його потужності P_{RF}. Розраховано фазову діаграму модельного пристрою – перетворювача НВЧ сигналів у НЧ сигнали – у координатах $(f;P_{RF})$ та показано, що масиви паралельно включених (на НВЧ) детекторів більш ефективні для перетворення відносно слабких НВЧ сигналів, а масиви послідовно включених (на НВЧ) детекторів мають кращу ефективність при перетворенні НВЧ сигналів з відносно високою потужністю.

Ключові слова: детектор НВЧ на основі магнітної наноструктури, керованої спін-поляризованим струмом, пороговий детектор, відбирання та перетворення НВЧ сигналу у низькочастотний сигнал.

Introduction. The spin-transfer torque (STT) carried by a spin-polarized electric current [1–2, 7, 10–11] can give rise to several types of magnetization dynamics (magnetization auto-oscillations and reversal) and, therefore, allows one to manipulate magnetization of a nanoscale magnetic object [9].

One of possible applications of the STT is the spin-torque microwave detector (STMD) based on the so-called spin-torque diode effect [3, 12]. In a STMD, a microwave current $I_{RF}(t) = I_{RF}\sin(\omega t)$ is supplied to a magnetic tunnel junction (MTJ) structure and excites magnetization precession in the free magnetic layer (FL). The resistance oscillations $R(t)$ resulting from this precession mix with the driving current $I_{RF}(t)$ to produce the output DC voltage $U_{DC} = \langle I_{RF}(t)R(t)\rangle$ (here $\langle ...\rangle$ denotes averaging over the period of oscillations $2\pi/\omega$ of the external microwave signal).

While the theory [13] predicts the typical resonance sensitivity of STMD to be $\varepsilon_{res} \sim 10^4$ V/W, the recent experiments performed by Prof. I.N. Krivorotov with colleagues [4–5] have proved that the sensitivity of spin-torque diodes can be substantially greater and can exceed $\varepsilon \sim 10^5$ V/W. It is important to note that the sensitivity of such STMD is more than 100 times higher than the sensitivity of Schottky diode (about $\varepsilon \sim 10^3$ V/W).

It has been shown recently that an STMD in a weak perpendicular bias magnetic field can operate as a non-resonant threshold detector of low frequency microwave signals [6]. In this novel dynamical regime of STMD operation, the detector is characterized by large-angle out-of-plane (OOP) magnetization precession, and therefore this regime can be called the OOP-regime. The output voltage of an STMD in the OOP-regime increases with the frequency of the input signal f, but is virtually independent of its power [6]. These properties of an STMD in the OOP-regime may be particularly suitable for applications in the microwave energy harvesting.

We believe, the STMD in the OOP-regime could be used as a base element for new energy harvesting devices, inasmuch as it has no resonance frequency, and, therefore, could accumulate energy from all the low-frequency region ($f_L < f < f_H$) of the microwave spectrum [6]. Here $f_L \approx 0.5 \div 1$ GHz is the lower detector's cut-off frequency, $f_H = \gamma B_0 / 2\pi$ is the upper detector's cutoff frequency, $\gamma \approx 2\pi \cdot 28$ GHz/T is the modulus of the gyromagnetic ratio, B_0 is the OOP weak bias DC magnetic field ($B_0 < \mu_0 M_S$), μ_0 is the vacuum permeability and M_s is the saturation magnetization of the FL of an STMD.

The energy conversion rate ζ_D of an STMD in the OOP-regime is estimated in [6] and has the form

$$\zeta_D(f, P_{RF,D}) = \frac{P_{DC,D}}{P_{RF,D}} \approx \frac{1}{2}\left[\frac{I_{th}(f)}{I_{RF,D}(P_{RF,D})}\right]^2 C^2(P), \qquad (1)$$

where $P_{DC,D}$ is the output DC power of an STMD under the action of input microwave power $P_{RF,D}$, $I_{th}(f)$ is the frequency-dependent threshold microwave current of an STMD, $I_{RF,D}(P_{RF,D})$ is a microwave signal current in the detector, $C(P) = \left(1-\sqrt{1-P^4}\right)/P^2$ is the dimensionless factor and P is the dimensionless spin polarization of current . Simple calculation shows that the maximum possible conversion rate of an STMD $\zeta_{D,\max} = C^2/2 \approx 3.5\%$ is reached in the case $I_{RF,D}(P_{RF,D}) = I_{th}(f)$, $P = 0.7$. Although the value of $\zeta_{D,\max}$ is less than 5% we believe that this ratio is sufficiently large for practical applications in microwave energy harvesting.

In this work we analyze a possibility and efficiency of microwave energy harvesting using an array of threshold STMDs operating in the OOP-regime. We calculate the total output DC power $P_{DC,A}$ and the total conversion rate ζ_A for an array consists of N STMDs under the action of monochromatic microwave signal with frequency f and power P_{RF}. We show that the energy harvesting rate and the total output DC power approximately linearly depend on

the small number of non-interacting detectors in the array N, but strongly depend on the frequency f and power P_{RF} of input microwave signal. We calculate the phase diagram of device's energy harvesting rate in coordinates $(f;P_{RF})$ and show that parallel arrays of STMDs have the higher efficiency at the lower levels of the input microwave power, while series arrays are preferable at the higher levels of the input microwave power.

Model and assumptions. At this stage we consider only the simplest case of N mutually uncoupled (non-interacting) detectors. We assume that all the detectors in the array are identical and have the same parameters. We also assume that the microwave resistance of an STMD $R_{RF,D}$ and the input microwave power P_{RF} are frequency-independent. For simplicity we also assume that the microwave resistance of an STMD $R_{RF,D}$ is equal to its DC resistance $R_{DC,D}$, hence, $R_{RF,D} = R_{DC,D} = R_D$.

Below, we analyze two simplest possible cases of schematics of an array of STMDs. In the first case all the detectors are biased in parallel at microwaves. This case may be realized when the array of the detectors is embedded in the outside protective layer of a device and the input microwave signal excites microwave currents $I_{RF,D}^{(p)}\left(P_{RF,D}^{(p)}\right)$ in each detector simultaneously. All the values corresponding to this regime of the device operation have the top index (p). The second case is the case when all the detectors are connected in series at microwaves. This case may be realized when the array of detectors is connected to an ideally-matched wide-frequency-range ($f_L < f < f_H$) microwave antenna. An input microwave signal with power P_{RF} can be transferred from the antenna to a series array of STMDs. Thus, the microwave current in each STMD $I_{RF,D}^{(s)}\left(P_{RF,D}^{(s)}\right)$ is equal to the total microwave current in the array $I_{RF,A}^{(s)}$, $I_{RF,D}^{(s)} = I_{RF,A}^{(s)} = I_{RF}^{(s)}$. All the values corresponding to this regime of the device operation have the top index (s).

In the following we consider a case, when the microwave power P_{RF} acting on each detector in the array is the same for all detectors, $P_{RF,D} = P_{RF}$ and do not depend on the number of detectors N. In other words, we assume that microwave power absorbed by each detector in the array is substantially smaller than the total microwave power existing in space. We stress that if this condition is not fulfilled the energy harvesting rate and the total output DC power produced by the array will become almost independent of the number of non-interacting detectors in the array N.

Theoretical analysis. When all STMDs in the array are connected in parallel, the microwave power acting on each detector with account of impedance mismatch effect [8] can be written as

$$P_{RF,D}^{(p)} = P_{RF}\frac{1}{4}\frac{\left(R_D + Z_{FS}\right)^2}{R_D Z_{FS}}, \qquad (2)$$

where $Z_{FS} \approx 377\ \Omega$ is the impedance of a free space (we consider the case when the array is located in a free space). Taking into account that $P_{RF,D}^{(p)} = 0.5\left[I_{RF,D}^{(p)}\right]^2 R_D$, one can obtain from (2) the exact expression for $I_{RF,D}^{(p)}\left(P_{RF}\right)$:

$$I_{RF,D}^{(p)}\left(P_{RF}\right) = \frac{R_D + Z_{FS}}{R_D}\sqrt{\frac{1}{2}\frac{P_{RF}}{Z_{FS}}}. \qquad (3)$$

The total output DC power $P_{DC,A}^{(p)}$ and the total conversion rate $\zeta_A^{(p)}$ in the case of N parallel biased microwave detectors can be calculated as

$$P_{DC,A}^{(p)} = NP_{DC,D}^{(p)} = \zeta_D^{(p)} N P_{RF}\frac{1}{4}\frac{\left(R_D + Z_{FS}\right)^2}{R_D Z_{FS}}, \qquad (4)$$

$$\zeta_A^{(p)} = \frac{P_{DC,A}^{(p)}}{P_{RF}} = N\zeta_D^{(p)}\frac{1}{4}\frac{\left(R_D + Z_{FS}\right)^2}{R_D Z_{FS}}, \qquad (5)$$

where $\zeta_D^{(p)} = \frac{1}{2}\left[\frac{I_{th}(f)}{I_{RF,D}^{(p)}\left(P_{RF}\right)}\right]^2 C^2(P)$.

Eqs. (4)–(5) show that the microwave energy harvesting in an array of parallel biased STMDs is most effective for a case of high-resistance detectors, when $R_D \approx Z_{FS}$. If the resistance-area product RA (the parameter of detector's material and fabrication technology) is selected, the condition $R_D \approx Z_{FS}$ can be fulfilled by choosing the appropriate size of the detector. In any case the total conversion rate cannot exceed $N\zeta_D^{(p)}$ ($N\zeta_D^{(p)} < 1$) and the total output DC power cannot exceed $N\zeta_D^{(p)}P_{RF}$ ($N\zeta_D^{(p)}P_{RF} < P_{RF}$).

When the STMD array is connected to a microwave antenna ideally-matched in a wide frequency range and all the detectors are biased in series, an input microwave signal of the power NP_{RF} can be delivered to the detector array having the total microwave resistance $R_A^{(s)} = NR_D$. The delivered signal excites the microwave current $I_{RF}^{(s)}$ in the array, which is the same for all the detectors, and with account of the impedance mismatch effect [8] can be written as

$$I_{RF}^{(s)}\left(P_{RF}\right) = \frac{NR_D + Z_{TL}}{NR_D}\sqrt{\frac{1}{2}\frac{NP_{RF}}{Z_{TL}}}, \qquad (6)$$

where $Z_{TL} = 50\,\Omega$ is the impedance of transmission line equal to the output resistance of the antenna.

The total output DC power $P_{DC,A}^{(s)}$ and the total conversion rate $\zeta_A^{(s)}$ in the case of N series-biased microwave detectors can be calculated as

$$P_{DC,A}^{(s)} = NP_{DC,D}^{(s)} = N\zeta_D^{(s)} P_{RF}\frac{1}{4}\frac{\left(NR_D + Z_{TL}\right)^2}{NR_D Z_{TL}}, \qquad (7)$$

$$\zeta_A^{(s)} = \frac{P_{DC,A}^{(s)}}{P_{RF}} = N\zeta_D^{(s)}\frac{1}{4}\frac{\left(NR_D + Z_{TL}\right)^2}{NR_D Z_{TL}}, \qquad (8)$$

where $\zeta_D^{(s)} = \frac{1}{2}\left[\frac{I_{th}(f)}{I_{RF,D}^{(s)}\left(P_{RF}\right)}\right]^2 C^2(P)$.

Eqs. (7)–(8) show that the microwave energy harvesting in the array of series biased STMDs is most effective for a case of low-resistance detectors, when $R_D \approx Z_{TL}/N$. If the resistance-area product RA (the parameter of detector's material and fabrication technology) is selected, the condition $R_D \approx Z_{TL}/N$ for some particular number of the detectors N can be fulfilled by choosing the appropriate size of the detector. In any case the total conversion rate cannot exceed $N\zeta_D^{(s)}$ ($N\zeta_D^{(s)} < 1$) and the total output DC power cannot exceed $N\zeta_D^{(s)}P_{RF}$ ($N\zeta_D^{(s)}P_{RF} < P_{RF}$).

It is obvious, that Eqs. (4), (5) are correct in the case $N = N^{(s)} < \frac{1}{\zeta_D^{(p)}} \frac{4R_D Z_{FS}}{\left(R_D + Z_{FS}\right)^2}$, while Eqs. (7), (8) are correct in the case $N = N^{(p)} < \frac{1}{\zeta_D^{(s)}} \frac{4NR_D Z_{TL}}{\left(NR_D + Z_{TL}\right)^2}$, i.e. $N < 29$ if we have ideally matched detector array.

This means that in a real device the output DC power and the total conversion rate could be improved by several times depending on the number of detectors N in the array. It is also understandable that it is more convenient to use small arrays of uncoupled STMDs ($N << N^{(p)}, N << N^{(s)}$) instead of large arrays. In small arrays of STMDs it is possible to achieve sufficiently high conversion rate and output DC power for a relatively small number of detectors $N \approx 1 \div 10$.

As one can see from Eqs. (4)–(5), (7)–(8), in the optimum case, when an array of non-interacting detectors is ideally matched to an external microwave circuit (free space or antenna), the total conversion rate and the output DC power approximately linearly depend on a small number of detectors in the array N. This condition is not fulfilled if $N \geq N^{(p)}, N^{(s)}$ respectively, thus for arrays with $N \approx N^{(p)}, N^{(s)}$ this dependence is not linear and can be approximately written as N^{α} (it is our assumption), where $\alpha << 1$. It is obvious that $\alpha = 1$ for $N = 1$ and must decrease with an increase of N. It seems, that in the simplest case α may be *qualitatively* evaluated as $\alpha(N) = 1/N$. More rigorous expression for $\alpha(N)$ should be found from an experiment.

Using the proposed simple expression $\alpha(N) = 1/N$, we can estimate characteristic improvement N^{α} for $P_{DC,A}^{(p)}(N)$, $P_{DC,A}^{(s)}(N)$ and $\zeta_A^{(p)}(N)$, $\zeta_A^{(s)}(N)$ for ideally matched arrays, presented in Fig. 1. As one can see the device energy conversion rate and the output DC power can be improved for an array with several detectors. The optimum number of the detectors is $N_{opt} = 2 \div 5$.

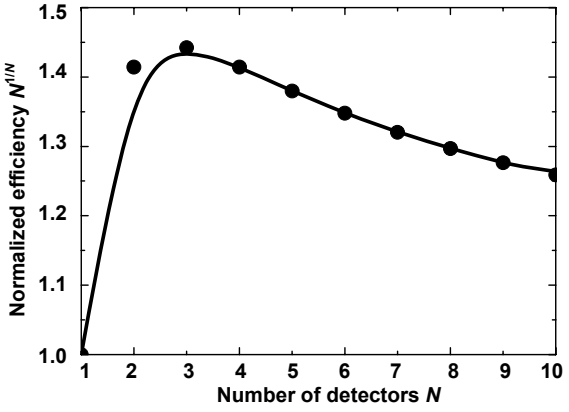

Fig. 1. Characteristic approximate dependence of improvement $N^{1/N}$ of output DC power $P_{DC,A}^{(p)}(N)$, $P_{DC,A}^{(s)}(N)$ and total conversion rate $\zeta_A^{(p)}(N)$, $\zeta_A^{(s)}(N)$ relatively to $P_{DC,D}$ and ζ_D, respectively, as a function of number of detectors N for ideally matched array (points are exact values and line is a spline approximation)

Results and discussion. In the following we consider only the case of an array of non-interacting detectors, which is ideally matched to an external microwave circuit, i.e. the case $R_D = Z_{FS}$ for the STMDs connected in parallel and $NR_D = Z_{TL}$ for the STMDs connected in a series.

In our calculations we used the following typical parameters of an STMD at the temperature 300 K (see e.g. [3, 6, 12–13]): spin-polarization efficiency $P = 0.7$, Gilbert damping constant $\alpha = 0.01$, saturation magnetization of the FL $\mu_0 M_s = 0.8$ T, OOP bias DC magnetic field $B_0 = 38$ mT. For simplicity in the following we consider the case $N \approx N_{opt} = 4$.

The typical dependencies of $\zeta_A^{(p)}(P_{RF})$ (solid lines) and $\zeta_A^{(s)}(P_{RF})$ (dashed lines) for ideally-matched four detectors are presented in Fig. 2 and the typical dependencies of $\zeta_A^{(p)}(f)$ (solid lines) and $\zeta_A^{(s)}(f)$ (dashed lines) are presented in Fig. 3. One can see from these figures that an array of parallel-biased STMDs allows one to perform energy harvesting at the lower levels of the input microwave power, while an array of series-biased STMDs is more convenient to perform energy harvesting from microwave signals with larger levels of input microwave power. We expect that real energy harvesting devices may consists of a combination of parallel and series detector arrays in order to have good performance in a wide range of input microwave powers.

Since the energy conversion rate strongly depends on the frequency and power of input microwave signals, we calculate the phase diagrams of device's energy harvesting rate in coordinates $(f; P_{RF})$ for the optimal number of detectors $N = N_{opt} \approx 4$. These diagrams are presented in Figs. 4, 5. One can see that the energy harvesting device based on a parallel array of uncoupled STMDs can operate in high-frequency low-power area, while the performance of the device based on a series array of uncoupled STMDs is better in low-frequency high-power area on the phase diagram.

We believe that the formalism developed above may be used for optimization of real energy harvesting devices with parallel and series detector arrays working simultaneously.

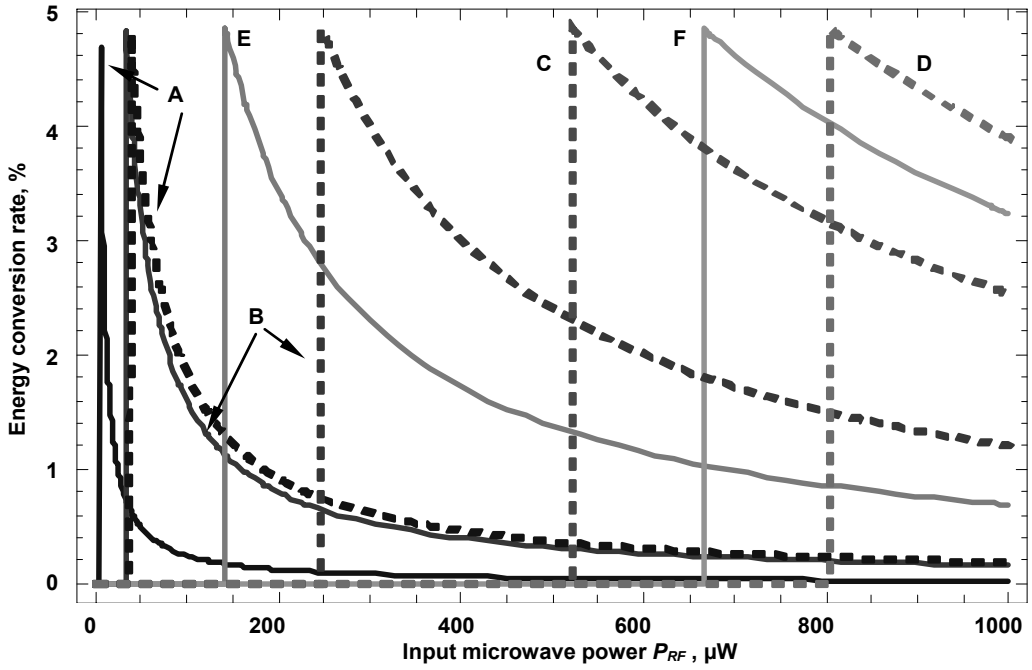

Fig. 2. Dependencies of $\zeta_A^{(p)}(P_{RF})$ (solid lines) and $\zeta_A^{(s)}(P_{RF})$ (dashed lines) for ideal-matched detectors in a case of different signal frequency: A – $f = 1$ GHz, B – $f = 2$ GHz, C – $f = 2.5$ GHz, D – $f = 2.8$ GHz, E – $f = 3$ GHz and F – $f = 4$ GHz

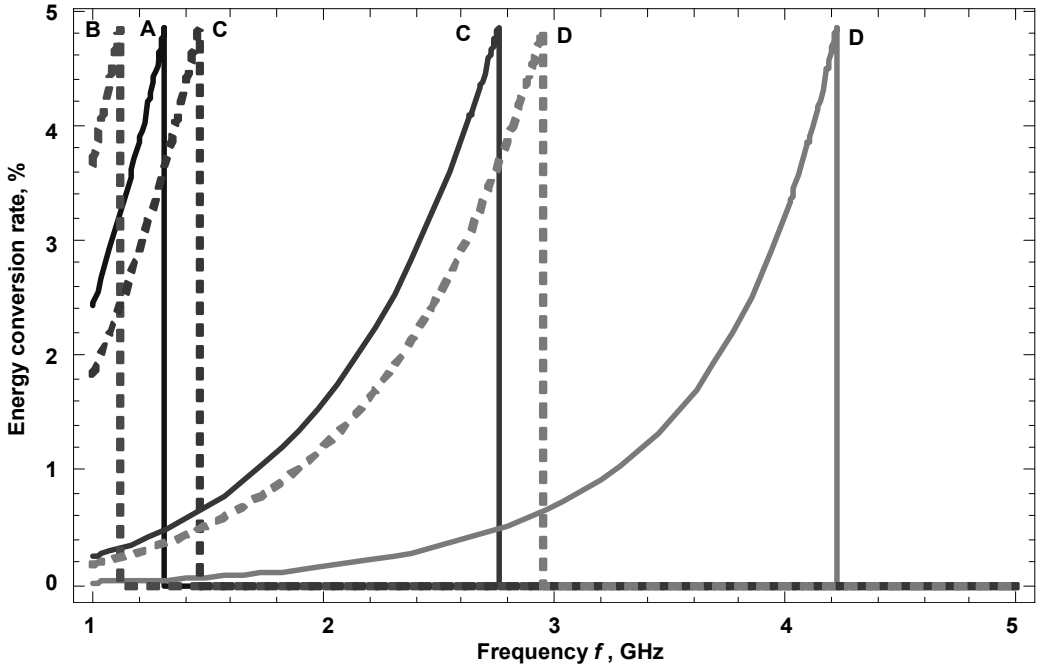

Fig. 3. Dependencies of $\zeta_A^{(p)}(f)$ (solid lines) and $\zeta_A^{(s)}(f)$ (dashed lines) for ideal-matched 4 detectors in a case of different signal power: A – $P_{RF} = 10$ μW, B – $P_{RF} = 50$ μW, C – $P_{RF} = 100$ μW, D – $P_{RF} = 1$ mW

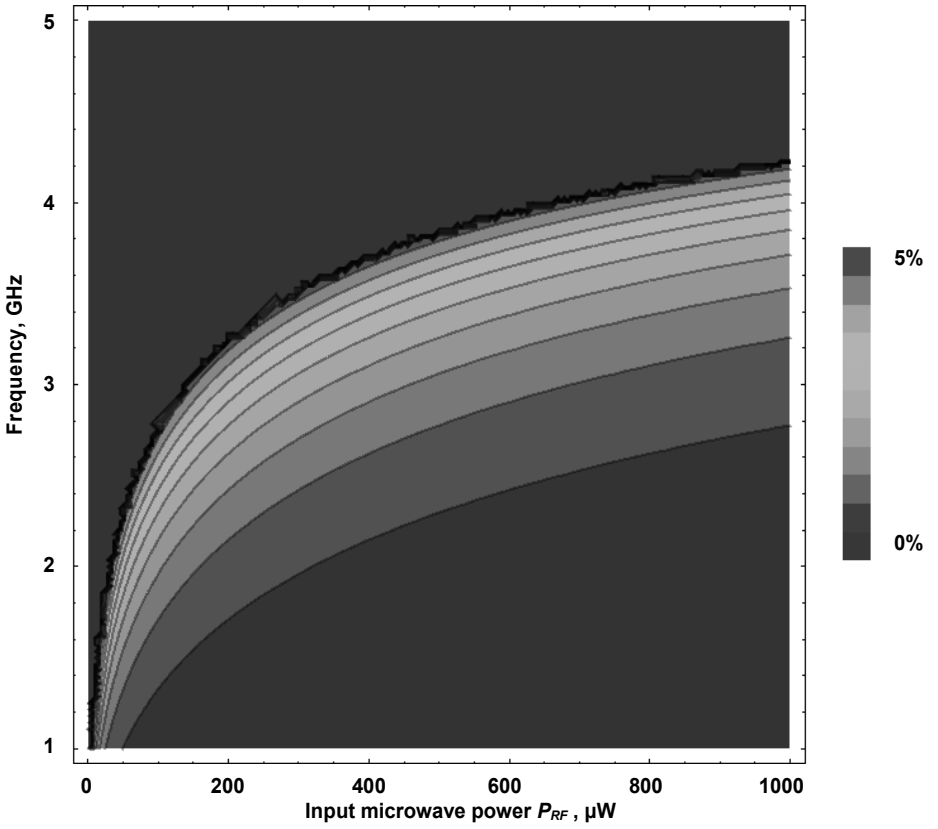

Fig. 4. Phase diagram for $\zeta_A^{(p)}(P_{RF}, f)$ in coordinates $(f; P_{RF})$ for an ideally matched array of $N = 4$ STMDs

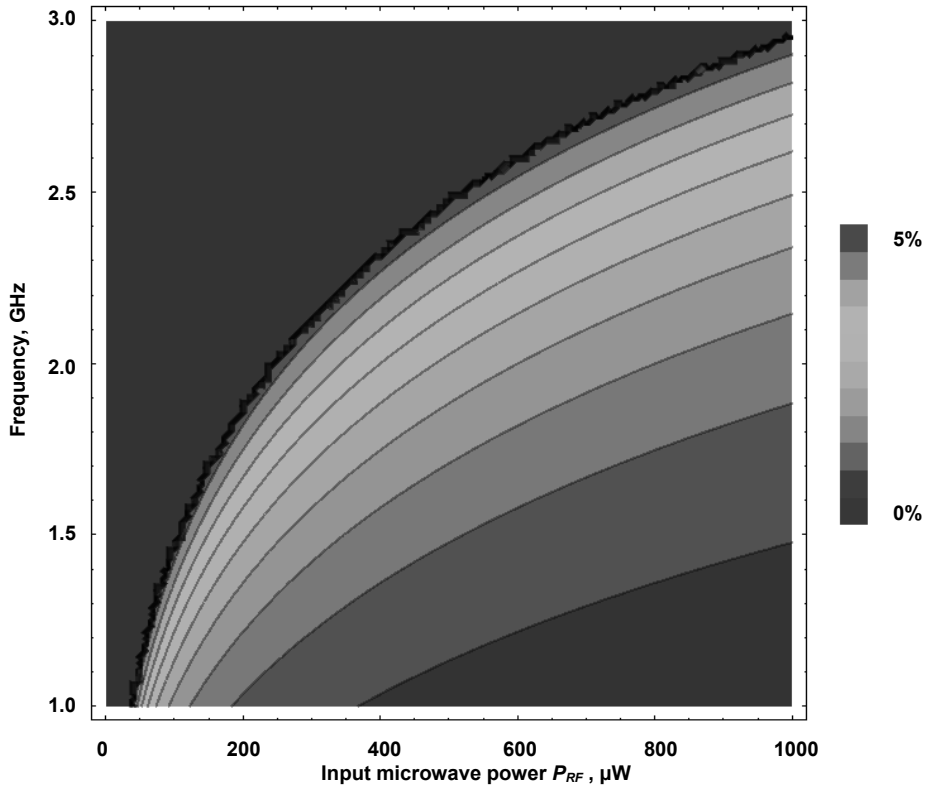

Fig. 5. Phase diagram for $\zeta_A^{(s)}(P_{RF}, f)$ in coordinates $(f; P_{RF})$ for an ideally matched array of $N = 4$ STMDs

Conclusion. We have demonstrated that the energy harvesting rate and the total output DC power are approximately linearly depend on the small number of non-interacting detectors in the array, and strongly depend on the frequency f and power P_{RF} of an input microwave signal. For the optimal number of detectors in the array $N_{opt} \approx 4$ we calculate the phase diagram of the device's energy harvesting rate and show that parallel arrays of STMDs have higher efficiency at lower levels of an input microwave power, while the series arrays are preferable at the higher levels of an input microwave power. We believe that the formalism presented above may be used for optimization of real energy harvesting devices with parallel and series detector arrays working simultaneously.

Acknowledgments. The authors would like to thank to Prof. A.N. Slavin and Dr. V.S. Tiberkevich for discussions.

This work was supported in part by grant M/212–2011 of The State Agency of Science, Innovations and Informatization of Ukraine and by grant UU34/008 of The State Fund for Fundamental Researches of Ukraine.

1. *Погорілий А.М., Рябченко С.М., Товстолиткін О.І.* Спінтроніка. Основні явища. Тенденції розвитку // Український фізичний журнал. Огляди. – 2010. – Т. 6, № 1. 2. *Berger L.* Emission of spin waves by a magnetic multilayer traversed by a current // Physical Review B. – 1996. – Vol. 54. 3. *Ishibashi S., Seki T., Nozaki T., Kubota H., Yakata S., Fukushima A., Yuasa S., Maehara H., Tsunekawa K., Djayapravira D.D., Suzuki Y.* Large diode sensitivity of CoFeB/MgO/CoFeB magnetic tunnel junctions // Applied Physics Express. – 2010. – Vol. 3. 4. *Cheng X., Boone C.T., Zhu J., Krivorotov I.N.* Nonadiabatic stochastic resonance of a nanomagnet excited by spin torque // Physical Review Letters. – 2010. – Vol. 105. 5. *Cheng X., Boone C.T., Zhu J., Krivorotov I.N.* Spin torque diode detectors with sensitivity exceeding that of Schottky diodes // Abstracts of the 55th Annual Conference on Magnetism and Magnetic Materials (MMM 2010, Atlanta, Georgia, USA). – 2010. – EC–03. 6. *Prokopenko O.V., Krivorotov I.N., Bankowski E., Meitzler T., Jaroch S., Tiberkevich V.S., Slavin A.N.* // Journal of Applied Physics. – 2012. – Vol. 111. 7. *Ralph D.C., Stiles M.D.* Spin Transfer Torques // Journal of Magnetism and Magnetic Materials. – 2008. – Vol. 320. 8. *Ramo S., Whinnery J.R., van Duzer T. Fields and Waves in Communication Electronics.* – New York: Wiley, 1984. 9. *Slavin A., Tiberkevich V.* Nonlinear auto-oscillator theory of microwave generation by spin-polarized current // IEEE Transaction on Magnetics. – 2009. – Vol. 47. 10. *Slonczewski J.C.* Current-driven excitation of magnetic multilayers // Journal of Magnetism and Magnetic Materials. – 1996. – Vol. 159. 11. *Slonczewski J.C.* Excitation of spin waves by an electric current // Journal of Magnetism and Magnetic Materials. – 1999. – Vol. 195. 12. *Tulapurkar A.A., Suzuki Y., Fukushima A., Kubota H., Maehara H., Tsunekawa K., Djayaprawira D.D., Watanabe N., Yuasa S.* Spin-torque diode effect in magnetic tunnel junctions // Nature. – 2005. – Vol. 438. 13. *Wang C., Cui Y.-T., Sun J.Z., Katine J.A., Buhrman R.A., Ralph D.C.* Sensitivity of spin-torque diodes for frequency tunable resonant microwave detection // Journal of Applied Physics. – 2009. – Vol. 106.

Submitted on 27.09.12

UDC 533.9.08

R. Semenyshyn, stud., A. Lebid, post grad. stud.,
V. Boretskij, Ph. D., I. Babich, Ph. D., A. Veklich, Ph. D.

INVESTIGATIONS OF PLASMA OF ELECTRIC ARC DISCHARGE BETWEEN BRASS ELECTRODES

Методами оптичної емісійної спектроскопії досліджено параметри плазми вільно існуючого електродугового розряду між латунними електродами при силах струму 3,5 та 30 А. Радіальні розподіли температури плазми визначали методом діаграм Больцмана із залученням спектральних ліній атомів міді та цинку. Обговорюється доцільність застосування окремих спектроскопічних констант ліній ZnI у діагностиці плазми з домішками парів цинку. Проаналізовано можливість використання моделі локальної термодинамічної рівноваги в такій плазмі.

Ключові слова: оптична емісійна спектроскопія, плазма електродугового розряду.

The parameters of free burning electric arc plasma between brass electrodes at arc currents 3.5 and 30 A are studied by optical emission spectroscopy techniques. The radial distributions of plasma temperature were obtained by Boltzmann plot method using spectral lines of copper and zinc atoms. The suitability of some ZnI spectroscopic data usage in diagnostics of plasma with zinc vapours is discussed. The possibility of application of local thermodynamic equilibrium model in such plasma is analyzed.

Keywords: optical emission spectroscopy, plasma of electric arc discharge.

Introduction. Wide application of composite materials in devices for the electrical engineering industry has stimulated the interest in studying of the arc discharge plasma burning between electrodes produced from such materials. These electrodes are usually produced from composite materials or alloy of several metals as well. Namely, brass is an example of copper and zinc alloy, which is widely used. Optimization of these electrotechnical devices is impossible without knowing the plasma parameters in such discharges.

Plasma diagnostics is important part of numerous scientific investigations and industrial applications. The optical emission spectroscopy (OES) is the most widely used method for arc plasma diagnostics [4]. It allows to obtain such important characteristics of arc as temperature and electron density without disturbing of the object.

It is well known that plasma temperature can be obtained by absolute measurement or by comparison of relative intensities of spectral lines. Existence of local thermodynamic equilibrium (LTE) and axisymmetric configuration of the arc are supposed in such kind of measurements.

Since the electric arcs occur in breaking of the contacts in switching devices, it believes that studied free burning discharges can be used as a model of real arcs. Therefore such investigations may clarify the processes of mass transfer in a discharge gap.

In this work plasma of a free-burning electric arc in air between brass electrodes is studied by OES technique.

Experimental setup. The arc was initiated in air between the flat end surfaces of non-cooled rod electrodes. The electrode diameter was 6 mm; the discharge gap was 8 mm, the arc currents were 3.5 A and 30 A. To avoid the metal droplet appearing a pulsing high current mode was used: the current pulse of 30 A was put on the "duty" low-current (3.5 A) discharge. The pulse duration was 30 ms.

Due to the spatial and temporal instability of the discharge, we used the method of one-pass tomographic recording of the spatial distribution of spectral line intensities [1]. Fast scanning of the spatial distributions of the radiation intensities was performed using the (B/W) Sony ILX526A 3000 pixel CCD linear image sensor (Fig. 1).

Due to the instability of the discharge, we carried out statistical averaging of the recorded spatial distributions of the radiation characteristics. We also took into account the non-uniformity of the spectral sensitivity of the apparatus.

In order to carry out the spectroscopic procedures for plasma diagnostics in electric arc discharges between brass electrodes, we need reliable information about the spectroscopic data of the spectral lines for zinc and copper, namely, oscillator strength. Additional problem in the temperature measurement by the relative intensity method is the selection of appropriate spectral lines.

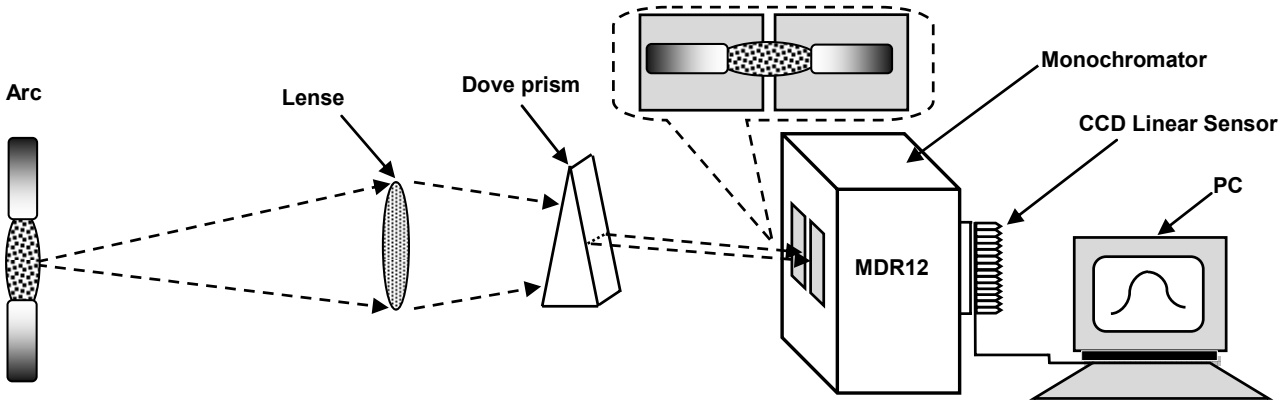

Fig. 1. Scheme of experimental setup

Results and discussions. For diagnostics of plasma of electric arc discharge the CuI lines 510.5 nm, 515.3 nm, 521.8 nm, 570.0 nm, 578.2 nm and 793.3 nm previously were selected [2]. In addition to copper spectral lines some lines of zinc were used too. Namely, lines ZnI 462.9 nm, 468.0 nm, 472.2 nm, 481.0 nm and 636.2 nm were selected. For arc current 30 A CuI spectral line 521.8 nm wasn't taken for temperature obtaining, because of overlapping with CuI spectral line 522.0 nm as one can see in interferogram obtained using Fabri-Perrot interferometer [6] (see Fig. 2).

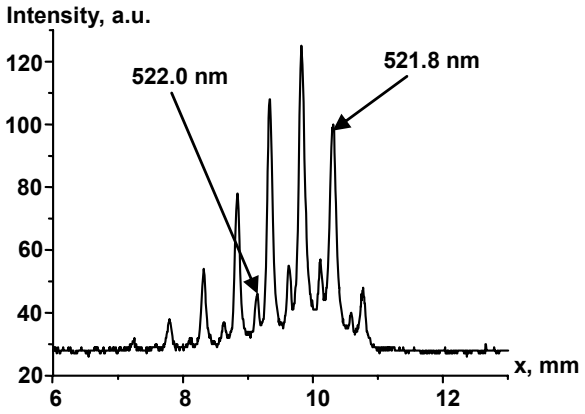

Fig. 2. Interferogram of CuI spectral lines

The spectroscopic data for CuI and ZnI lines were previously selected in [2] and [3], respectively. This work is the next step in selection of spectroscopic data. Namely, the ZnI 462.9 nm line with log(g·f) = -0.93 [5] was additionally selected.

In Fig. 3 and Fig. 4 Boltzmann plots obtained by CuI and ZnI lines emitted by electric arc plasma at discharge axis are shown for arc currents 3,5 A and 30 A respectively. One can see that linear fitted diagrams obtained by both spectroscopic elements are close to be parallel. It means that the temperatures obtained from these plots at this radial point should be in a good agreement. Therefore, the plasma model of local thermal equilibrium (LTE) can be assumed. The temperature for every point of radial distance from plasma column axis can be obtained from the slopes of Boltzmann plot for these spatial points, respectively.

We compare Boltzmann plot obtained by CuI and ZnI lines emitted by plasma of electric arc discharge between brass electrodes in air for two different radial distances (see Fig. 5 and Fig. 6). As one can see, with increasing of radial distance Boltzmann plots are not acceptable for temperature measurement with a good accuracy.

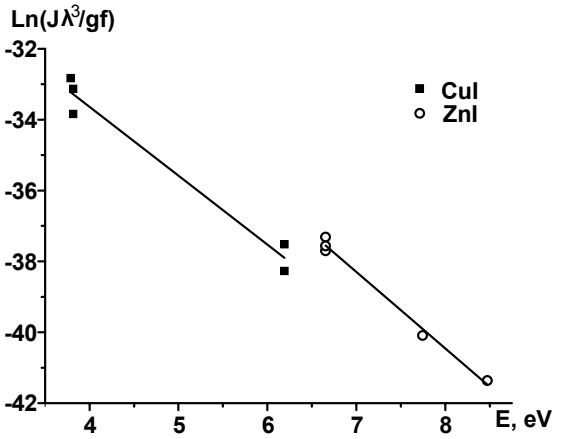

Fig. 3. Boltzmann plot obtained by CuI and ZnI lines emitted by plasma of electric arc between brass electrodes, arc current 3,5 A, radial distance r = 0 mm

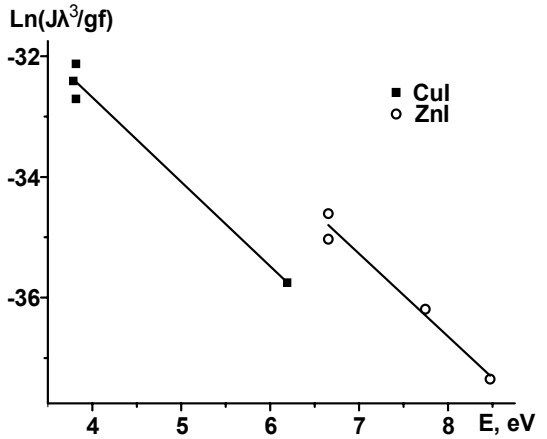

Fig. 4. Boltzmann plot obtained by CuI and ZnI lines emitted by plasma of electric arc between brass electrodes, arc current 30 A, radial distance r = 0 mm

The matter is that the population densities cannot be used to form a straight line in the Boltzmann plot for both spectral elements with increasing radial distance. Taking this into account the assumption of LTE isn't correct at the distance more than 2 mm (see Fig. 6).

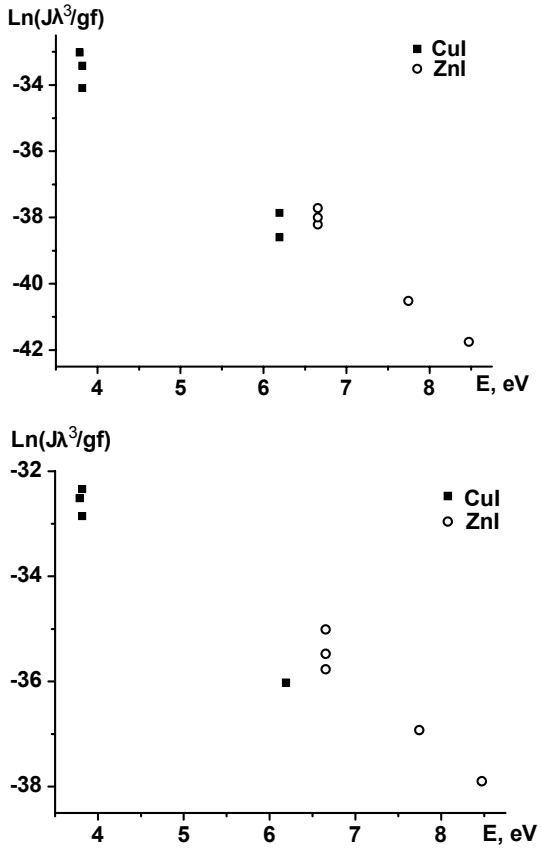

Fig. 5. Boltzmann plot obtained by CuI and ZnI lines emitted by plasma of electric arc discharge between brass electrodes, arc current 3,5 A (a) and 30 A (b), r = 1,1 mm

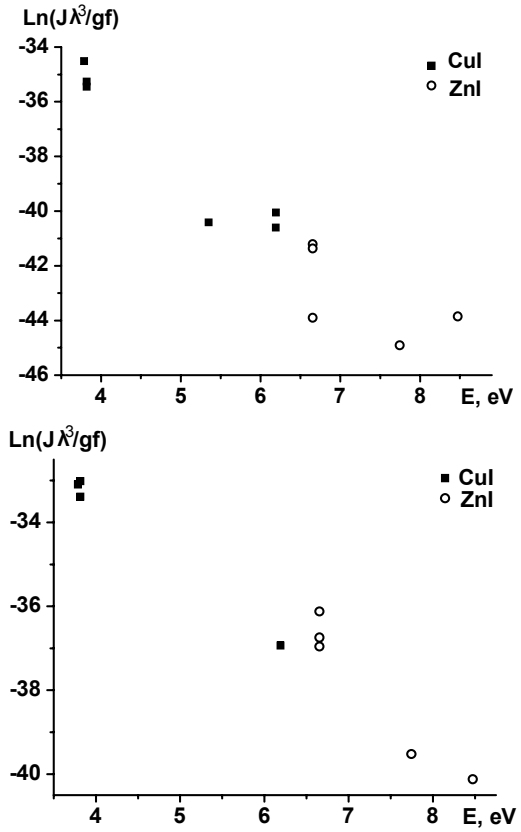

Fig. 6. Boltzmann plot obtained by CuI and ZnI lines emitted by plasma of electric arc discharge between brass electrodes, arc current 3,5 A (a) and 30 A (b), r = 2,6 mm

In Fig. 7 and Fig. 8 radial distribution of plasma temperature of electric arc discharge between brass electrodes in air obtained by CuI and ZnI lines are shown for arc currents 3.5 A and 30 A, respectively. One can see that chosen spectral lines of copper and zinc provide a good agreement in the temperature measurement with an appropriate accuracy. So, spectral line ZnI 462.9 nm line with log(g·f) = -0.93 [5] can be recommended for plasma diagnostics additionally.

Conclusions. Testing of previously selected ZnI spectral lines were provided. From the Boltzmann plot analysis we recommend these lines and their spectroscopic data selected in [3] for diagnostics of plasma with zinc vapours. Additionally, spectral line ZnI 462.9 nm line with log(g·f) = -0.93 [5] can be recommended too.

In approach of LTE the radial distributions of temperature in arc plasma was obtained by ZnI and CuI lines as well. Taking into account the agreement between temperatures obtained by using spectral lines of these elements the LTE is realized in such plasma. At radial distance more than 2 mm studied plasma is not in equilibrium.

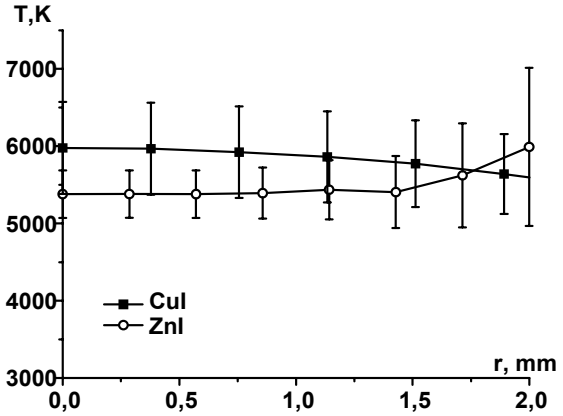

Fig. 7. Radial profiles of temperatures in air plasma of electric arc between brass electrodes obtained by CuI and ZnI lines, arc current 3,5 A.

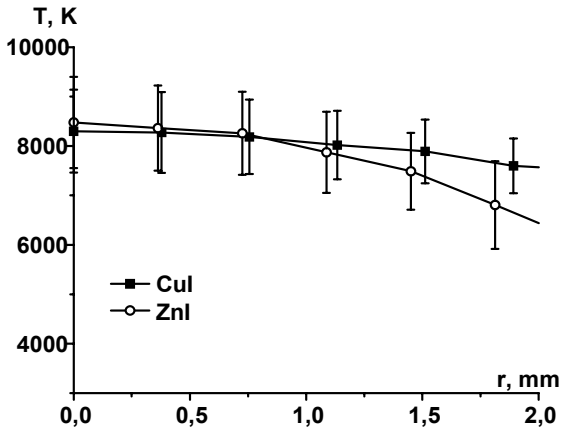

Fig. 8 Radial profiles of temperatures in air plasma of electric arc between brass electrodes obtained by CuI and ZnI lines, arc current 30 A

1. *Babich I. L., Osidach V. Ye., Sobovoy V. I., Veklich A. N.* // Czechoslovak Journ. of Physics. – 2002 – 52, Supplement D, pp. D731–D735.
2. *Бабіч І.Л., Борецький В.Ф., Веклич А.М.* та ін. Спектроскопія плазми електродугового розряду між композитними електродами Ag-CuO // Труды института проблем материаловедения им. И.Н. Францевича НАН Украины. Серия: Композиционные, слоистые и градиентные материалы и покрытия. Электрические контакты и электроды. – 2010. – С. 82–115.

3. *Бабіч І.Л., Борецький В.Ф., Веклич А.М.,* та ін. Спектроскопія плазми електродугового розряду між композитними електродами Ag-SnO_2-ZnO // Труды института проблем материаловедения им. И.Н. Францевича НАН Украины. Серия: Композиционные, слоистые и градиентные материалы и покрытия. Электрические контакты и электроды. – accepted in May 2012. 4. *Murphy A.* The effects of metal vapour in arc welding // J. Phys. D: Appl. Phys. – 2010. – 43. 5. *Thevenin F.* Oscillator strength from the solar spectrum // Astron. Astrophys. Suppl. Ser. – 1989 – 77 – pp.137–154. 6. *Veklich A.N., Osidach V.Ye..* The determination of electron density in electric arc discharge plasma //Bulletin of the University of Kyiv. Series: Physics & Mathematics – 2004 – pp.428–435.

Submitted on 14.05.12

UDC 533.9

S. Sidoruk, eng., V. Chernyak, Doc.sci., E. Martysh, Doc.sci., V. Yukhymenko, eng., S. Olszewski, Ph.D., I. Babich, Ph.D., O. Fedorovich, Ph.D.

THE CYLINDRICAL GEOMETRY PULSED PLASMA–LIQUID SYSTEMS WITH THE POSSIBILITY OF CONVERGENT ACOUSTIC WAVES EFFICIENT GENERATION

У роботі досліджено можливість генерування збіжних акустичних хвиль в рідині за допомогою відбивання створених імпульсним електричним розрядом акустичних хвиль від твердої циліндричної поверхні. Отримано спектри випромінювання плазми імпульсного розряду в воді та у воді з домішками повітря, розрахована температура заселення електронних збуджених рівніе атомів міді CuI та кисню OI, в тому числі поведінку цієї температури під час розрядного струму.

Ключові слова: імпульсна плазмово-рідинна система, збіжна акустична хвиля, неідеальна плазма, температура.

This research investigates the possibility of convergent acoustic waves generation in a liquid by means of waves reflection created by pulsed electric discharge from a solid cylindrical surface. The spectra of pulse discharge plasma radiation in water and in water with air dash were obtained. Electronic levels excitation temperature of Cu I and O I atoms was calculated, including the behaviour of such excitation temperature during the discharge current.

Keywords: pulsed plasma-liquid system, convergent acoustic wave, non–ideal plasma, temperature.

Introduction. Nowadays, in plasma chemistry use of non-equilibrium plasma and transition to plasma-liquid systems (PLS), with a help of which greater efficiency and selectivity of chemical reactions initiated by fast electrons can be achieved, is considered to be more perspective. [2–3].

By raising discharge capacity some difficulties may occur when using the non-equilibrium plasma. For example, changing the discharge type for more equilibrium one and increase the discharge current [1]. Such problems can be avoided by transition to the pulsed regime with a fundamentally different mechanism of increasing the discharge power level.

New related factors emerge due to the usage of pulsed electrical discharges in the liquid: strong ultraviolet radiation and acoustic or even shock waves. Systems with energies of more than 1 kJ/pulse may be often found in literature which can't be good for the resource of such systems work. From this perspective, the usage of pulsed systems with relatively low pulse energy and focusing of acoustic waves is more reasonable. Besides, the acoustic oscillations in such systems can be used as an additional influence mechanism on chemical transformations.

The most attention is paid to the systems with strong convergent waves when using the acoustic vibrations for chemical reactions. However, the processes when the powerful convergent waves are collapsing are not studied well enough. System of cylindrical, spherical or parabolic surfaces used when focusing the shock waves for the technological needs are well known in the literature [4–7]. However, among their disadvantages, such should be mentioned: not using all of the acoustic wave energy and the problem of peripheral sources generation synchronization, which in its turn leads to a distortion of the front shock wave ideality and thus reduces the efficiency of the focusing.

Perhaps, more promising method of using acoustic waves is to generate them by single axial pulse electric discharge with subsequent reflection from the perfect focusing surface. This approach can provide better convergent acoustic wave compression symmetry both in the gas and liquid medium. This research is devoted to studying of such an approach possibilities.

Experimental setup. Plasma chemical reactors of cylindrical geometry with discharge plasma axial location have been created on the condition that the plasma channel characteristic radius r is much smaller than the base cylinder radius R. If to maintain this ratio the construction could be of two types: either the cylinder radius and height are proportionate or radius is much bigger than the height of the cylinder. Figures 1–2 present plasma chemical reactors schemes:

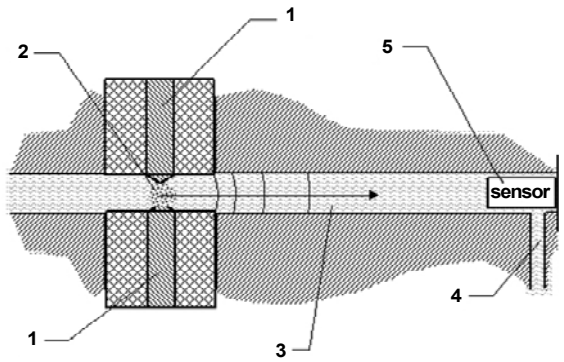

Fig. 1. Scheme of experimental plasma chemical reactor (base radius is much bigger than the cylinder height) 1 – metal electrodes, 2 – discharge plasma, 3 – liquid subsystem, 4 – channel to output the signal wire pressure sensor, 5 – pressure sensor

Stainless steel cylinder outer diameter is 370 mm and internal – 270 mm. Outer cylinder height is 100 mm and internal – 10 mm. Pressure sensor is located inside the cylinder (Fig. 1), with one end touching the inner wall of the cylinder, and the other one projecting inside of the channel for 20 mm (the length of the sensor). Two stainless steel coaxial electrodes hermetically imposed in teflon insulators have been aggregated in the liquid volume in order to form a discharge gap. Insulators diameter is 20 mm. Electrode diameter – 10 mm. The points of working electrodes in a shape of cone have angle of 90° and spherical surface with a radius of 2 mm. Discharge gap length for the steady breakdown in the liquid is 0.5 mm at the voltage of 19 kV. This design has been used with condenser capacities up to 18 nF and the voltage of up to 20 kV. Also the used geometry has been with proportionate height and radius of the cylinder (Fig. 2).

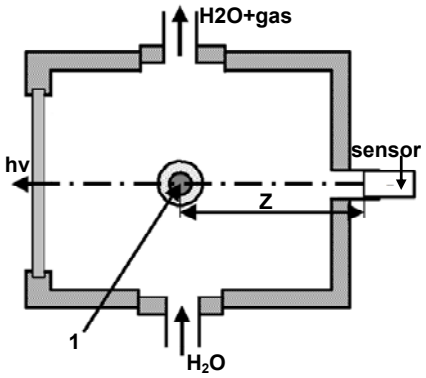

Fig. 2. Scheme of experimental plasma chemical reactor (base radius and height of the cylinder are proportionate), 1 – 10 mm diameter electrodes, introduced into the teflon insulators with 20 mm diameter

Electrodes with the diameter of 10 mm, introduced into the Teflon insulators with the diameter of 20 mm are marked on the figure with 1. Optical investigations were carried out by recording plasma channel radiation that passes through the quartz window. Pressure sensor was located on the system axis and the distance from the electrodes to the sensor was 95 mm (Z on Fig. 2). The radius of the cylinder was 140 mm, and the height was 170 mm.

Results and discussion. Plasma radiation properties. The following regimes and different liquid parameters have been used to investigate the pulsed discharges emission in liquid: distilled water, distilled water with the air flow in discharge gap with speed of 50cm^3/s and the water absence (atmospheric pressure air). Plasma radiation spectra for these regimes are presented in fig. 3–4:

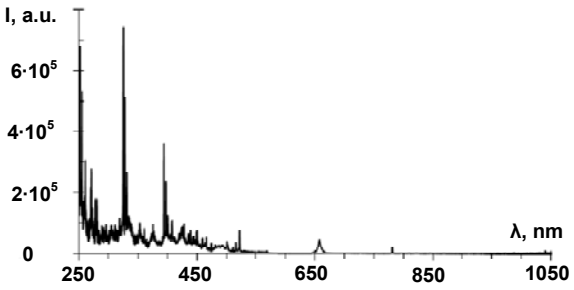

Fig. 3. Plasma radiation spectrum of the pulsed discharge in water with air flow

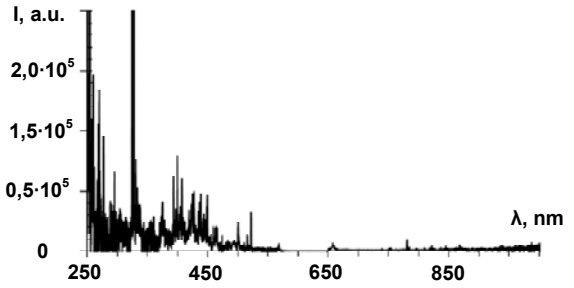

Fig. 4. Plasma radiation spectrum of the pulsed discharge in air at atmospheric pressure

In the spectra electrode material luminescence lines were visible - copper Cu I at wavelengths of 324.7 nm, 327.4 nm, 510.5 nm, 515.3 nm, 521.8 nm, OI 777.1 nm; 844.6 nm; broaden hydrogen line of the Balmer series – 656.3 nm. For the plasma radiation spectrum of pulse discharge in air – the lowest luminescence intensity of smallest hydrogen-oxygen components and the largest contribution from the electrode material have been observed.

The situation changes in the case of pulsed electric discharge plasma in the water without an air dash. Plasma radiation spectra for these regimes are presented on fig. 5.

Continuous luminescence areas, located in the near ultraviolet and at the beginning of the optical fields could be observed on the indicated radiation spectrum. Broaden hydrogen line of the Balmer series is observed (656.3 nm) lines of O I (777.1 and 844.6 nm) and absorbed areas at the wavelengths which correspond to resonant transitions of Cu I (324.7 nm and 327.4 nm). Due to the intensity modulation of the continuous spectrum connected with the SOLAR II spectrometer peculiarities, modulated continuous luminescence areas averaging was held with help of software package Origin 7.0. 10 averaging mode operations in the 100 points have been used (average value in the range has been calculated (i-(n / 2)): (i + (n / 2)), where i – is the curve index point, and n – number of averaging, in this case 100). It is assumed that the continuous signal modulation spectrometer is connected with the interference on the CCD lines protective film (film thickness ~1 μm).

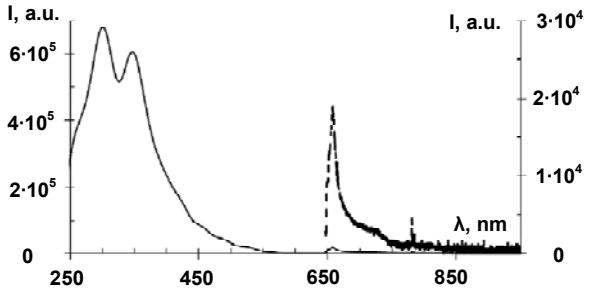

Fig. 5. Plasma radiation spectrum of pulsed discharge in water. Secondary axis shows the bigger range scale of 640–950 nm

Excited electronic population levels temperature (that in all cases was about 11000K±500K) for the regimes in which it was possible to observe lines of Cu I 510.5, 515.3 and 521.8 nm has been calculated by the Boltzmann diagram method.

It is noticeable that so-called non-ideal plasma type is implemented in the pulsed discharge in a liquid, which reveals itself by continuous luminescence area appearance [13]. The dense plasma is called non-ideal in where the average potential energy of particles interaction is comparable to their average kinetic energy [8, 14].

The Boltzmann formula use implies that the Debye sphere contains many charges: $n_e 4\pi d^3/3 >> 1$. This imposes restrictions $ne << 2{,}5 \cdot 10^5 (T(K))^3 cm^{-3}$ on the theory applicability. In this case, the average energy of two charges interaction is much smaller than the thermal energy kT. When $n_e > 10^7 (T(K))^3 cm^{-3}$ – plasma is clearly non-ideal [11].

Thus at a temperature of 10^4 K electrons concentration in non-ideal plasma is $n_e > 10^{19}$ cm^{-3}, and in the case of electric discharge pulsed plasma in the gas channel with a liquid wall at the temperature of the copper atom excited levels of 10^4 $n_e = 10^{17}$ cm^{-3} (conditionally accepted by T(K)). Therefore we can say that such plasma is weakly non-ideal.

From these radiation spectra one can see that air addition into the fluid results in almost complete disappearance of plasma continuous luminescence areas as well as to the hydrogen line width reduction at half height (eg, water $\Delta\lambda \approx 13$ nm, water with air $\Delta\lambda \approx 5$ nm), which indicates reduction of both electron concentration and non-ideal plasma.

Plasma channel radiation could have been recorded using the Photo-electrical multiplier and monochromator MDR-23, which allowed to obtain luminescence plasma channel profile and duration in time, and on specific wavelengths. Oscillograms of luminescence and current are presented in Figure 6.

During plasma pulsed discharge radiative properties study in a liquid it has been established that the duration of plasma channel luminescence at the energies of $0.1 \le E \le 30$ J practically does not exceed the duration of the discharge current, which is different from cases where pulse energy is $E \ge 1$ kJ [10]. In the case of pulsed discharge in a liquid, the smaller amplitude level area appeared on a current oscillogram. It is assumed that it corresponds with the electrolysis phase, and the proof for that is – the plasma luminescence absence when in the area (Fig. 6), which indicates that the mechanism is different from a discharge current flow.

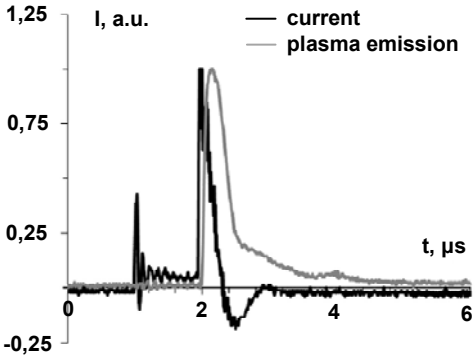

Fig. 6. Oscillograms of discharge current and plasma radiation (water, C=0.015 uF, without air, ballast resistor R=10 ohms)

Highly dispersed gas bubbles, which can't be combined into one, are formed during the electrolysis. It is considered that electrolysis stochastic duration phase always precedes the pulse discharge flow in the liquid phase. Since the discharge itself occurs in a liquid with micro bubbles, this result can be considered as a proof of Mark Kushner's bubble theory (University of Michigan, USA) [5]

Differences in the intensity of luminescence rate rise for the OI lines have been revealed, while studying the behavior of the luminescence plasma channel duration at wavelengths, which correspond to the identified components in the averaged spectra.

The explanation of this fact can be obtained by considering the cross sections dependence of oxygen atom electronic levels excitation from the average energy of electrons [7]. When increasing electrons energy, primarily, higher electron levels of oxygen atoms are filled and then lower. The electrons average energy depends on the electric field in the discharge gap, and that is why at high values of electric field (at the previous impulse front) more rapid filling of the oxygen atom higher electronic level is expected in the discharge gap (E_2=12.08 eV, 926.6 nm).

Temperature populations of oxygen atom excited levels O fall within the discharge current, which is typical for the initial phase of gas-discharge plasma development. While the near-cathode potential jump emerges, the electric field in the inter-electrode gap rapidly decreases..

Generation of convergent acoustic waves. Pressures growth has been expected to appear on the front acoustic waves formed by electrical discharges because of the cylinder geometry (Fig. 1), which allowed to increase the condenser capacity to 0.18 nF. The discharge gap length was 0.5–1 mm. Also ballast resistor which value could be changed to 100 ohms has been placed in the discharge circuit. In Fig. 8 the acoustic signal and discharge current oscillograms at different ballast supports for pulse PLS cylindrical geometry with proportionate radius and height of the cylinder (Fig. 2) are presented.

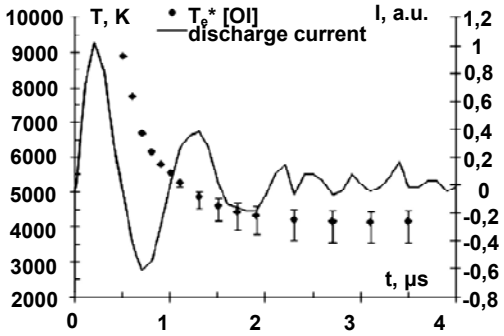

Fig. 7. Excitation temperature of oxygen atom O I during the discharge current

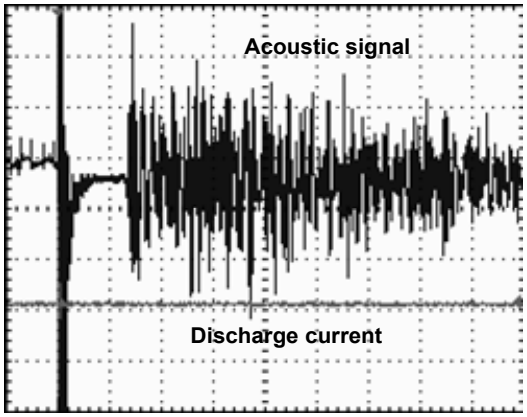

Fig. 8. Oscillograms of current and acoustic signal C=15 nF, discharge gap of 0,5 mm, U=19 kV. Sensitivity 50 μs/div.

The first signal burst on the upper oscillogram is the electromagnetic obstacle from the pulse breakdown, because of the form similarity and appearance time of that signal part in the form and appearance of the discharged current recorded at the lower oscillogram, and is not directly related to the acoustic signal. Time of noisy acoustic signal appearance corresponds to 70 microseconds from the time of discharge current fixation and is comparable with the time of acoustic waves passage in water from the system axis to its wall (length 95 mm – t=0,095(m)/1500(m/s) =6 4 • 10^{-5}(s)). Noisy nature of the acoustic signal might be connected with the own sensor vibrations.

In the pulsed plasma-liquid system with cylindrical geometry where radius of the cylinder is much bigger than its height – another result has been observed (Fig. 1). Typical oscillogramme of the acoustic signal and discharge current in such system is presented in figure 9.

Acoustic signal with delay time of 80 microseconds has been detected towards the discharge current, which corresponds to the time of acoustic waves passage to the lateral surface (length 115 mm – t=0,0115(m)/ /1500(m/c)=7,6•10^{-5}(c)). But the fact of the second acoustic signal burst appearance, comparable to the first one, with the delay time of 170–180 microseconds, which corresponds to the passage time of acoustic waves from the lateral surface to the axis of the cylindrical system and back is fundamentally different. A similar situation has been observed in the case of working capacity increase to 180 nF.

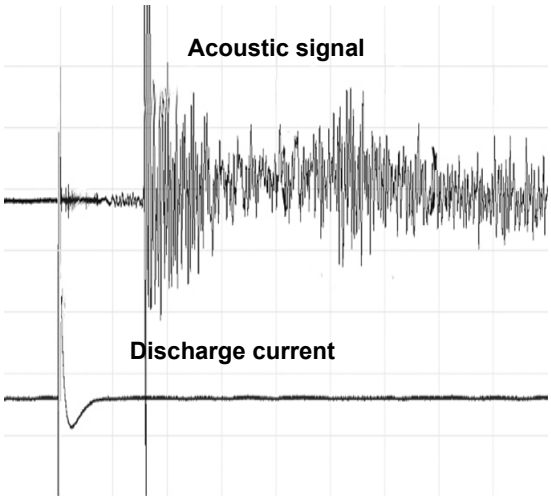

Fig. 9. Oscillogram of current and acoustic signal C=15 nF, discharge gap 0.5 mm, U=19 kV. Sensitivity 50 μs/div.

Conclusions. The electrolysis phase presence preceding heterophase environment electrical breakdown and points to the discharge development in the liquid with micro bubbles are shown. This result confirms the Mark Kushners theory of "bubble" breakdown (University in Michigan, USA) [5].

For the first time the formation of convergent acoustic wave after reflection from an ideal solid cylindrical surface in plasma-liquid system with cylindrical geometry and axial single pulse discharge has been investigated. It is shown that effective focusing can be expected during the passage of acoustic waves inside the system, such as proportionality divergent and convergent reflected acoustic waves energies. This result means that systems with additional acoustic-chemical effect for plasma chemical applications are promising.

During the studies of pulsed discharge plasma radiation properties in the liquid the weak non-ideal plasma formation has been detected with the concentration not exceeding 10^{17} cm^{-3}. Adding air to the liquid reduces the intensity of the continuous spectrum and the concentration of electrons, so it is believed that the air dash reduces non-ideality plasma level.

The decreased temperature characteristic of excited oxygen atom levels population (O I) has been obtained during the discharge current duration, which is typical for the initial phase of gas-discharge plasma development.

Proportionality of plasma luminescence and discharge current duration has been discovered, which is fundamentally different from cases with powerful pulsed discharges in water at a pulse energy of more than 1 kJ [10].

1. *Chernyak V.* Sources of nonequilibrium plasma at atmospheric pressure / I. Prysyazhnevych, V. Chernyak, J.D. Skalný, Š. Matejčik, V. Yukhymenko, S. Olszewsky, V. Naumov // Ukr. J. Phys. – 2008. – vol. 53, № 5. – P. 472–476. ISSN 0503–1265. 2. *Fridman A.* Plasma Chemistry / A. Fridman. – N.Y.: Cambridge Univ. Press, 2008. 3. *Fridman A.* Plasma Physics & Engineering / A. Fridman., L. Kennedy. – N.Y.: Taylor & Francis, 2004. 4. *Kruglyakov E.P.* Evolution of mirrors in Novosibirsk: past, present and future / E.P. Kruglyakov, A.V. Burdakov, A.A. Ivanov // Book of abstracts of International conference-school on plasma physics and controlled fusion and 4-th Alushta international workshop on the role of electric fields in plasma confinement in stellarators and tokamaks, September 13–18, 2010, Alushta, Crimea, Ukraine — P. 175. 5. *Kushner M.J.* Plasma production in liquids: bubble and electronic mechanism / N.Yu. Babaeva, M.J. Kushner // Bulletin of the APS GES10, October 4–8, Paris, France – 2010. – vol. 53, 3. – P. 151. ID: BAPS.2010.GEC.QR.1 2. 6. *Lukes P.* Generator of focused shock waves in water for biomedical applications / P. Lukes, P. Sunka, P. Hoffer, V. Stelmashuk, J. Benes, P. Pouckova, J. Zeman, L. Dibdiak, H. Kolarova, K. Tomankova P. / Book of Abstracts: NATO Science Advanced Research Workshop on Plasma for bio-decontamination, medicine and food security, March 15–18, 2011, Jasná, Slovakia. – P. 67–68. 7. *Lieberman M.A.* Principles of plasma discharges and materials processing / M.A. Lieberman, A.J. Lichtenberg. – NY. A Wiley & Sons, INC., 1994. ISBN: 0–471–00577–0. 8. *Кулик П.П.* Неидеальная плазма / П.П. Кулик, В.А. Рябый, Н.В. Ермохин – М.: Энергоатомиздат, 1984. – С. 200. 9. *Попов Н.А.* О термоядерном синтезе при взрыве сферического заряда (проблема газодинамического термоядерного синтеза) / Н.А. Попов, В.А. Щербаков, В.Н. Минеев, Р.М. Зайдель, А.И. Фунтиков // УФН. – 178, №10. – 2008. – С. 1087–1094. 10. *Пасечник Д.Л.* Временная эволюция спектров излучения импульсных разрядов в воде / Д.Л. Пасечник, П.Д. Старчик, О.А. Федорович // Сборник научных трудов "Теория, эксперимент, практика разрядноимпульсной технологии", Киев "Наукова думка". – 1987. – С. 6–9. 11. *Райзер Ю.П.* Физика газового разряда / Ю.П. Райзер. – М.: "Наука", 1987. 12. *Тесленко В.С.* Генерация и фокусировка ударно-акустических волн в жидкости многоочаговым электрическим разрядом / В.С. Тесленко, В.В. Жуков, А.П. Митрофанов, А.П. Дрожжин // Журнал технической физики. – 1999. – 69, №4. – С. 138–140. 13. *Федорович О.А.* О рекомбинации водородно-кислородной плазмы ИРВ на стадии релаксации / О.А. Федорович, Л.М. Войтенко // Материалы XIII Международной научной школы-семинара "Физика импульсных разрядов в конденсированных средах", 21–25 августа. – Николаев, 2007. – С. 116–118. 14. *Фортов В.Е.* Физика неидеальной плазмы / В.Е. Фортов, И.Т. Якубов – Черноголовка, 1984. – С. 264.

Submitted on 14.02.12

UDC 536.6

V. Sohatsky, Ph. D., I. Zavislak, Dr. Sci., M. Popov, Ph. D.

CHANGE OF MAGNETIC STATE OF FERRITE-GARNET FILM UNDER MECHANICAL STRAIN

Представлені результати впливу механічних напруг у п'єзоелементі цирконату-титанату свинцю на доменну структуру механічно зв'язаної з ним магнітооптичної плівки залізо-ітрієвого гранату. Механічна деформація такої сендвіч-структури при прикладанні електричної напруги до п'єзоелемента може призводити до переорієнтації напрямку вектора намагніченості магнітооптичної плівки з перпендикулярного до паралельного її площині. Зміни доменної структури, що супроводжують таку переорієнтацію можуть використовуватись для керування параметрами світла, що проходить через плівку.

Ключові слова: намагнічування, ферит-гранат, магнітооптика.

The results of influence of mechanical pressure in a zircon-titan lead piezoelement on domain structure of epitaxial yttrium-iron garnet film, being in a close contact with piezoelement are presented. Such a sandwich structure consisted from magnetic layers rigidly joined with a zircon-titan lead piezoceramic (PZT) element allowed to remagnetize ferromagnetic layer without application of magnetic field, only by means of application voltage to PZT that created a mechanical strain. The results of mechanical pressure effect on domain structure of epitaxial yttrium-iron garnet (YIG) film, contacting with a piezoelement are presented in this paper. The possibilities of using a composite YIG-PZT structure for light control are also shown.

Key words: magnetization, ferrite-garnet, magneto-optics.

Introduction. The problem of light control by means of magnetization changes is actual for creation of the devices for optoelectronics [7], spintronics [5], quantum computing, etc. There are several methods suitable for changes of magnetization as application of magnetic field, mechanical stress, polarized current, illumination by light, etc. The problem of the nanosized elements remagnetization is connected with power consumption because of the problem in localization of magnetic field [10]. Another way of remagnetization, studying during the last years is to use a polarized current. This method is complicated in realisation because of too high current density, necessary for remagnetization (up to 108A/cm2). Therefore a remagnetization under applied electric voltage due to magnetoelastic effect is seems promising since it is profitable from the energy losses point of view.

For noticeable changes of the domain structure (or a local magnetization) with the small losses, the film should be soft magnetic with high enough magnetostriction and have a suitable mismatch of the crystal lattices size parameter with the substrate. The internal mechanical strain arisen because a mismatch have strong effect on magnetic anisotropy, which can create instability of the domain structure (nearest to indifferent position of magnetization). In such a case the reconstruction of domain structure occurred the most easily. The obvious additional requirements to magnetooptical film are small anisotropy and high magnetooptical Faraday rotation.

So the goal of this work was to investigate the influence of mechanical stress on magnetization and light transmission coefficient of magnetooptic film with a stripe periodic domain structure.

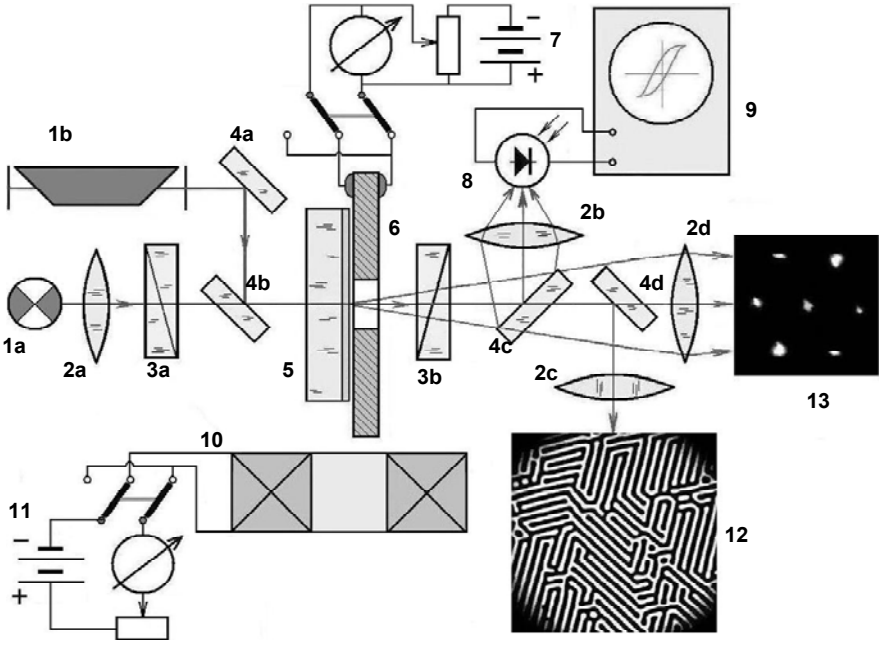

Fig. 1. Scheme of experimental set-up for magneto-optical and piezoelectric measurements. The numbers marks: 1 – light sources (a tungsten lamp, light-emitting diode, and/or lasers with 0,628 nm or 0,532 nm wavelengthes; 2 – optical elements (lenses); 3 – polarizers; 4 – light-splitting cells (half-transparent and conventional mirrors); 5 – YIG film on GGG substrate; 6 – PZT-piezoelement, rigidly connected with YIG film; 7 – a source of voltage for piezoelement; 8 – photodetector; 9 – oscilloscope for display of a loop of a magnetic hysteresis; 10 – the coil for creation of magnetic field; 11 – current source for a coil; 12 – magneto-optical image of the domain structure observed in a microscope; 13 – spectrum of light diffraction on YIG domain structure

Samples and experimental set-up. General scheme of the experimental equipment, used for measurements, is presented on Fig. 2. This experimental set-up allowed to observe the domain structure and correspondent diffraction spectra as well as to measure the intensities of the diffraction spectra components and angles of Faraday rotation of the light beam, passed through the film.

Magnetic hysteresis loops were obtained as a dependence of magnetization vs applied magnetic field or voltage, applied to piezoelement plate, rigidly connected with YIG film. The piezoelement had a disk shape with metallized surfaces and contact pads for electric connection; a round hole of approximately 2 mm in diameter was done in the disk centre for transmission of light. The samples of magnetooptical YIG films had either 2-layered structure (two films on both sides of gallium-gadolinium garnet $Ga_3Gd_5O_{12}$ substrate) or only one layer on one side of the substrate (just nearest to a piezoelement).

The transparent GGG substrate allowed to use magneto-optical Faraday effect for measurements of perpendicular-to-plane component of YIG magnetization and to observe diffraction of light on its domain structure.

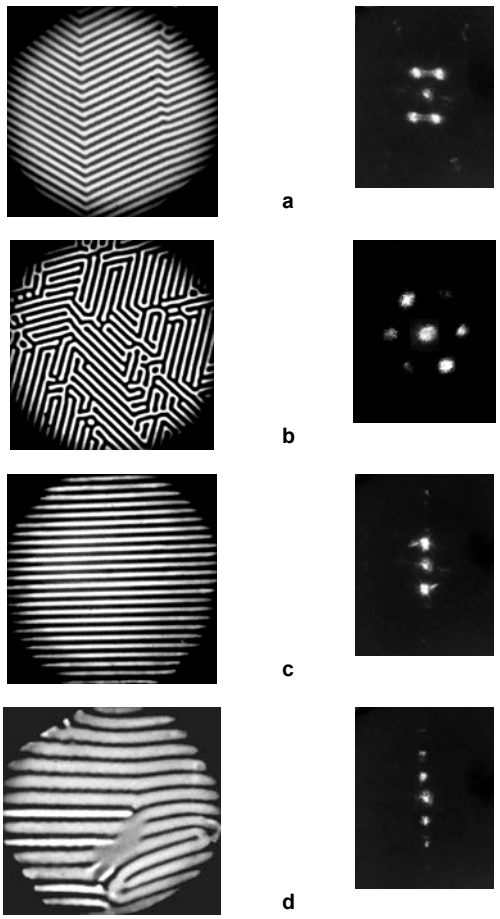

Fig. 2. Reconstruction of YIG domain structure and correspondent diffraction spectra under the influence of external magnetic field

Reconstruction of YIG domain structure. A typical domain structure of YIG film in the equilibrium state could looks like a "parquet" (Fig. 2a and 2b), with the stripe domains placed along three easiest directions of anisotropy axes in the film plane. If magnetic field of several Oersted was applied in any of 3 easy directions in the film plane, all the stripe domains were directed along the nearest directions of the easy axes (Fig. 2c). In case of magnetization in the directions of hard axes (with slightly higher fields of the domain reconstruction, that are shown on Fig.3) the initial stripe structure took the form of a "parquet".

Increasing of the applied field (H>6 Oe) could change a relation of their sizes (Fig. 2d): half of them increase their width and another half decrease; thus a total period is being changing slightly, that is seen as appearance of even maxima on correspondent diffraction spectra.

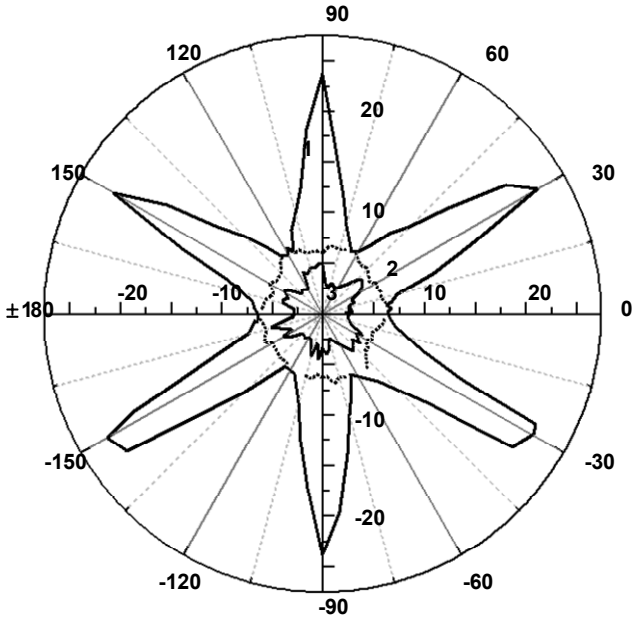

Fig. 3 . Dependence of reconstructing fields value (radii on azymuthal angle between the field and <110> axis: 1– reconstruction of the domain structure from "parquet" type into stripes; 2– reconstruction to non-symmetric relation of the domains sizes; 3 – reorientation of magnetization into in-plane direction

At the field from 8 till 11 Oe, a domain structure of Faraday type become almost invisible (if the light beam is perpendicular to the film plane) because of in-plane reorientation of magnetization. The above value is for easy axis direction; it increases to 32 Oe in hard direction and depends on the explored film area, magnetic pre-history, etc. In case of oblique illumination it is possible to distinguish the domains with a nearest to in-plane magnetization.

The domain structure of YIG film could be also changed under mechanical stress. These stresses are caused by deformation of a piezoelement under the voltage, applied to it. At piezovoltage $U_p \cong 130$V magnetization of YIG film was almost completely reoriented in a film plane from the initial perpendicular-to-plane direction. Unlike a previous case when reorientation took place under applied magnetic field, a stress-induced domain structure became considerably disordered as illustrated by Fig.4a,b.

The domains, formed under mechanical stress in the absence of external magnetic field had no unambiguous period or orientation in plane. Application of such a field, even quiet a small one, at once reconstructed the shape of domains into stripes and oriented them in the direction of applied field. Pictures on Fig.4c,d illustrate the possibility of observation of low contrast domains on the place of "disappeared" Faraday domain structure. This remaining structure, magnetized in a plane can be seen mainly because the light beam is not precisely perpendicular to magnetization

(i.e. presence of the small perpendicular component of magnetization that contributes to Faraday effect).

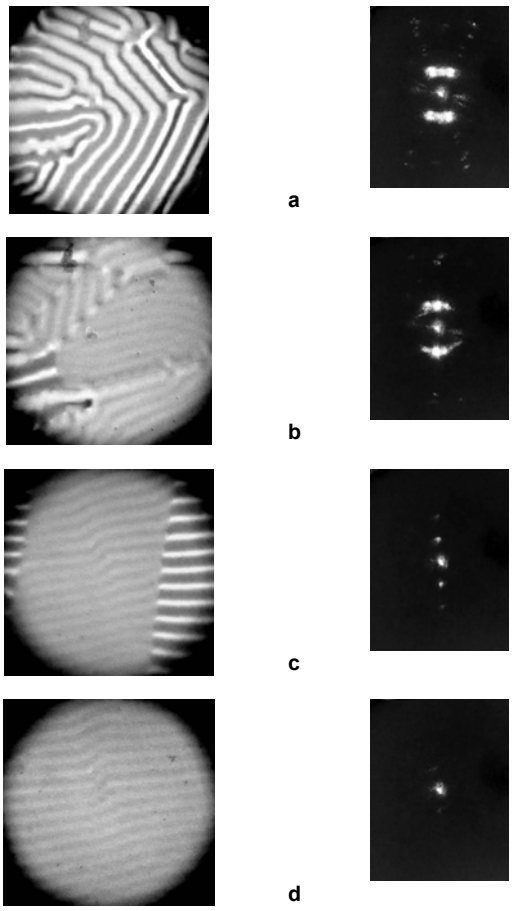

Fig. 4. Reconstruction of YIG domain structure and correspondent diffraction spectra under the influence of voltage, applied to piezoelement

Experiment. There is almost linear dependence of the piezovoltage, caused a total reoriention of magnetization from perpendicular to in-plane direction on external magnetic field *H*, applied in the film plane. On Fig.5 such a dependence is shown for the field parallel to [110] direction.

Such a reorientation of magnetization in plane under piezovoltage take place only in one direction of applied voltage, i.e when the film is compressed. In such a case a perpendicular-to-plane axis become hard magnetization axis and magnetization vector change its direction into plane. Changing polarity of the voltage, applied to piezoelement change the direction of its deformation and correspondent deformation of YIG film. When the film is extended, a perpendicular axis become easy and magnetization again is reoriented perpendicular-to-plane. In such a case the domain structure becomes looking like initial stripes parallel to three easy anisotropy directions with perpendicular-to-plane magnetization in domains, as it was shown on Fig. 2b. Thus application of the piezovoltage of reverse polarity allows to restore labyrinth type Faraday domain structure.

As it is seen from the graph, magnetic field of about *H*=6,4Oe intensity can reorients magnetization in a film plane without application of the piezovoltage. The graph allows to choose the values of magnetizing field and corresponding piezovoltage to control magnetization and selection of the optimal regimes of the monochromatic light beam modulation. Passing through the film with the "Faraday" stripe domain structure diffracted beam forms interference maxima, located in the transverse direction of the stripes. The intensity of light, diffracted on undoped alloy YIG film is small, accounting in accordance with the formula:

$$I_1/I = \frac{4}{\pi^2 \cdot n^2} \cdot \sin^2(\phi \cdot h) \cdot \sin^2\left(\frac{\pi n \nu_1}{\nu_1 + \nu_2}\right) \cdot e^{-\alpha h}$$

(where I - is the intensity of light beam entering the film, h = 10 mm - the thickness of YIG film, α =1400 cm^{-1} - absorption coefficient, ϕ=0.125 deg/μm - the angle of specific Faraday rotation YIG) and confirmed by the experimental value $I_1/I_0 \leq 0{,}01\%$ in the red and $\leq$ 0,02% in the green range (in YIG films doped with bismuth, diffraction efficiency reaches 1%).

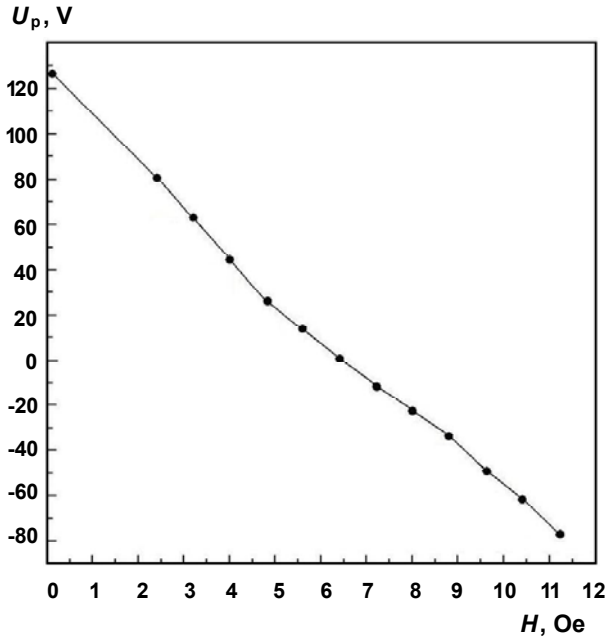

Fig. 5. Dependence of voltage on a piezoelement, necessary for reorientation of YIG magnetisation in a plane

Results and discussion. In order to use magnetic reorientation for modulation of light we feed the piezoelement by a.c. voltage of the rectangular or sinusoidal shape and measured intensity of the diffraction light (actually of the first maximum since the higher maxima are neglectly small). In spite of non-linear dependence of the diffraction light intensity I_1 on piezovoltag U_p (Fig.6), the shape of output signal was almost identical to the shape of input one, moreover independently on amplitude of the input voltage. The reason of this was in not too high amplitude of input a.c. voltage (up to ±16 V maximum value). Besides that in dynamic (or a.c.) mode some smoothing of the above dependence is occurred.

The dependence of the intensity of modulated signal on frequency demonstrates the gradual decreasing of amplitude after f> 3 kHz (Fig.7e) and tendency to fall down to 0 at f =5 kHz.

A simple model of domain structure, which was consisted from two types of periodical stripe domains with volume parts ν_1 and ν_2 was used for calculations. Magnetization of the domains is determined by minimum of the total free energy $W = W_{an} + W_Z + W_{dd}$, that is a sum of W_{an} – anisotropy, W_Z – Zeeman and W_{dd} - magnetostatic energies. The equilibrium energy W_0 from the above formula was obtained as a minimum W on alternatives θ_1, φ_1, θ_2, φ_2 for three values of anisotropy field H_U = -20 Oe; 0 Oe and 20 Oe.

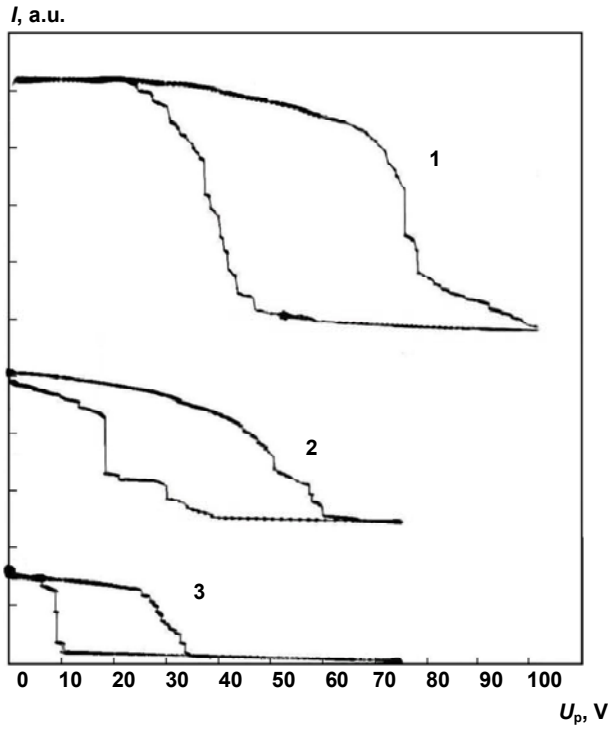

Fig. 6. Intensity of diffracted light on YIG domain vs voltage, applied to PZT at various external field: 1 – H=0 Oe; 2 – H=2 Oe; 3 – H=3,3 Oe

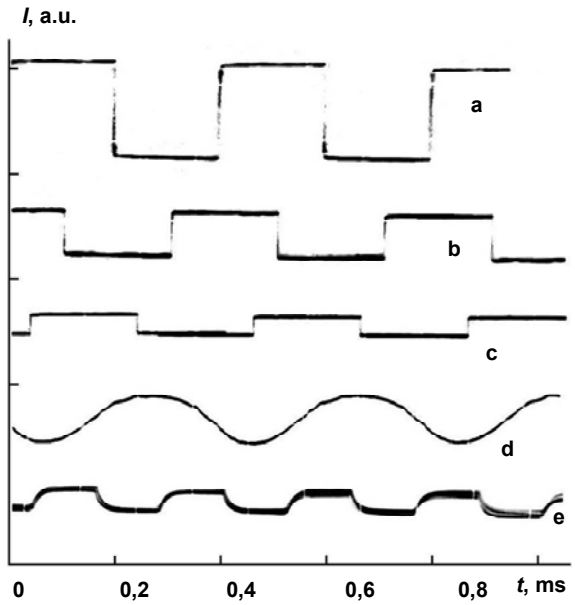

Fig. 7. Oscillograms of the diffraction intensity modulation by means of a.c. voltage, applied to piezoelement: a – U_p=54 V; b – U_p=64 V; c – U_p=74 V; d – U_p=54 V; e – f=3 kHz

The discrepancy between the direction of the uniaxial anisotropy in YIG film (111) and perpendicular direction to the plane is typical for such types of the films. In order to obtain the easy magnetization anisotropy axis perpendicular to the film plane at an arbitrary crystallographic orientation of this plane, it is necessary that the anisotropy constant $K_1 = C + \frac{3}{2}\sigma(\lambda_{100} - \lambda_{111})$, where C – is a phenomenological constant, σ – elastic stress, λ – magnetostriction constants along the respective axes. This requirement leads to high sensitivity of the direction of easy magnetization axis on composition heterogeneity, temperature changes, and applied mechanical stress. As a result, the magnetization in a film deviates from the exact perpendicular and parallel to the plane direction, which is also confirmed by a shape of magnetic hysteresis loops $M(H)$. The value of the uniaxial anisotropy energy being induced in the film with thickness h=10μm by means of elastic stresses do not exceeds ~10^{-4} erg/cm^3 because of the possible cracking of the film.

During theoretical calculations we used the stripe domain model with external static magnetic field H_0 lying in film plane and directed along $[1\bar{1}0]$ crystal axis. Normal to the surface is pointed along $[111]$, with $[11\bar{2}]$ direction completes the right-hand orthogonal basis. The domain walls are parallel to direction of applied magnetic field and perpendicular to sample surface. Such model is fully consistent with actual domain structure, observed in our experiment using magnetooptical methods in certain range of magnetic field values. The orientation of static magnetization vector $\vec{M}$ in each domain (further labeled using subscripts 1 and 2) is specified by the respective azimuth and polar angles (ϕ_i, θ_i) in spherical coordinate system whose polar axis coincides with sample normal and the azimuth angle is counted from $[11\bar{2}]$ direction. Mutual orientation of magnetization in adjacent domains is not specified and can be arbitrary. Assuming such stripe domain structure to be periodic in $[1\bar{1}2]$ direction, we can consider one period only and find the total free energy per unit volume [3]:

$$W = W_{an} + W_Z + W_{dd} + W_{dw}$$

that is a sum of W_{an} – crystal anisotropy energy (including cubic and uniaxial contributions) [11], W_Z – Zeeman energy; W_{dd} – magnetic dipole-dipole energy, that includes demagnetization energy for the net magnetization of the sample and demagnetization energy of poles on the walls of the domains, W_{dw} is the domain wall energy.

In result, we have derived expression for stripe domain structure free energy density:

$$\begin{aligned}\frac{W}{M_0} = {} & \nu_1 H_{cub}\left(\frac{\cos^4\theta_1}{4} + \frac{\sin^4\theta_1}{3} - \frac{\sqrt{2}\sin\theta_1\cos^3\theta_1\sin 3\theta_1}{3}\right) + \\ & + \nu_2 H_{cub}\left(\frac{\cos^4\theta_2}{4} + \frac{\sin^4\theta_2}{3} - \frac{\sqrt{2}\sin\theta_2\cos^3\theta_2\sin 3\theta_2}{3}\right) - \\ & - \frac{H_{U_1}}{2}\left(\nu_1\sin^2\theta_1 + \nu_2\sin^2\theta_2\right) - \frac{H_{U_2}}{4}\left(\nu_1\sin^4\theta_1 + \nu_2\sin^4\theta_2\right) - \\ & - H_0\left(\nu_1\cos\theta_1\sin\phi_1 + \nu_2\cos\theta_2\sin\phi_2\right) + \\ & + 2\pi N_\perp M_0\left(\nu_1\sin\theta_1 + \nu_2\sin\theta_2\right)^2 + \\ & + 2\pi N_{\parallel} M_0\left(\nu_1\cos\theta_1\sin\phi_1 + \nu_2\cos\theta_2\sin\phi_2\right)^2 + \\ & + 2\pi\nu_1\nu_2 N_d M_0\left(\cos\theta_1\cos\phi_1 + \cos\theta_2\cos\phi_2\right)^2 + \\ & + \frac{DM_0\left(\sin\theta_1 - \sin\theta_2\right)^2}{S\pi^2}\cdot\sum_{n=1}\frac{1-\cos 2\pi n\nu_1}{n^3} + \frac{2\gamma_{dw}}{M_0 D}.\end{aligned} \quad (1)$$

where $H_{cub} = \frac{K_{cub}}{M_0}$ - cubic anisotropy field (for YIG $K_{cub} < 0$ and H_{cub}=-45 Oe), $H_{U_1} = \frac{2K_{U_1}}{M_0}$, $H_{U_2} = \frac{4K_{U_2}}{M_0}$ - first and second order uniaxial anisotropy field, M_0 – saturation mag-

netization (M_0^{YIG} =140 Gs), γ_{dw} – specific wall energy [6,2], $N_\perp$ normalized to unity demagnetizing factor in perpendicular-to-plane direction ($N_\perp \approx 1$), $N_\parallel$ – in-plane demagnetizing factor in the direction parallel to H ($N_\parallel << 1$), $N_{dw} \approx S/(D+S)$ – domain walls demagnetizing factor [9], $\nu_i = d_i / D$ – volume parts of each domain (in all further calculation the domains are assumed to be equal, so $\nu_1 = \nu_1 = 1/2$).

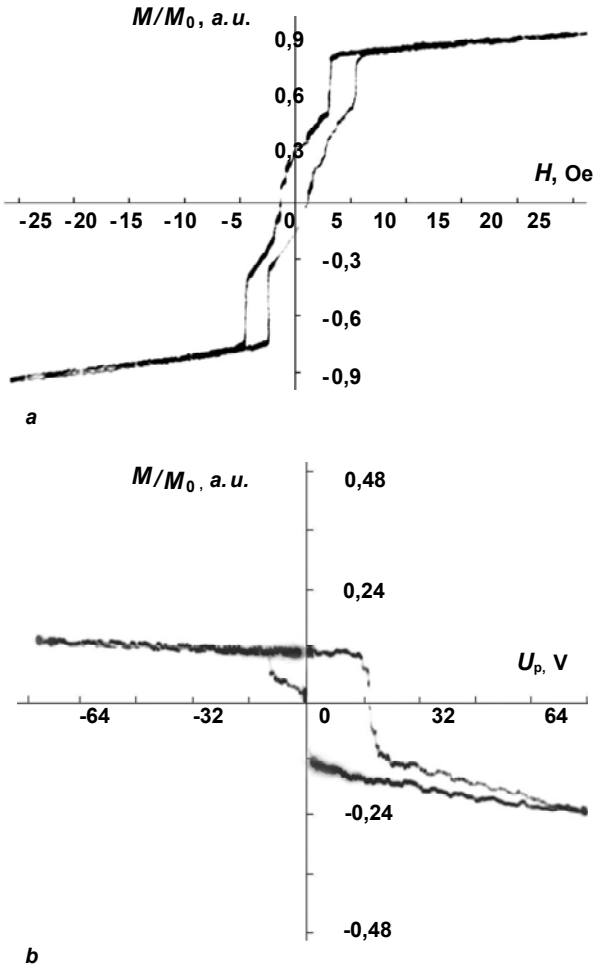

Fig. 8 . Hysteresis curves of YIG film in the field *H*, applied in the direction [110] (*a*) and under applied piezovoltage U_p (*b*)

The equilibrium state can be obtained by numerical minimizing W with respect to $\theta_1, \phi_1, \theta_2, \phi_2$ variables for given values of H_0 and H_{U_1}, H_{U_2}.

Obviously, the theory results are valid only when real domain structure corresponds to theoretical model. As we have found out during experiments, in magnetic field less then approximately 2 Oe, periodic stripe DS is transformed into labyrinth structure with the domains placed along three equivalent <110> directions in the film plane, according to [111] axis C_3 rotational symmetry. On the other side, when H_0 exceeds approximately 8 Oe, domains become substantially non-equal in width, with energy favorable one prevails. Thus, this theory is strictly applicable only for magnetic filed range of $2 < H_0 < 8$ Oe.

In the case of composite YIG-PZT structure, voltage-induced mechanical stress in YIG induce uniaxial anisotropy filed that can be calculated according to

$$H_{U_1}^E(V) = \frac{-3E}{1-\nu}\frac{\lambda_{111}}{M_S}\frac{d_{31}}{S}V \qquad (2)$$

where $E = 2 \cdot 10^{11}$ Pa is Young's modulus for YIG [10], $\nu = 0.29$ – Poisson's ratio (), λ_{111} is the magnetostriction constant [12], $d_{31} = -2.7 \cdot 10^{-10}$ m/V – PZT piezoelectric coefficient, V/S - is electric field strength, V – applied voltage, S – piezoelectric thickness.

Numerical minimizing of energy density (1) revealed the presence of three different local energy minima, we called them out-of-plane state (OOP, $\theta_1 \approx \pi/2, \theta_2 \approx -\pi/2$), in-plane state (IP, $\theta_1 \approx 0, \theta_2 \approx 0$) and canted state ($\theta_1 \approx \theta_c, \theta_2 \approx -\theta_c$, $0 < \theta_c < \pi/2$ and depends on H_0 and H_{U_1} values) respectively.

Investigation of phase diagram shows, that for positive uniaxial field domains magnetization is oriented predominantly along the surface normal (OOP state), while with decreasing H_{U_1} magnetization experience a first-order spin-flop phase transition [1] to canted configuration. In canted phase θ_c takes value of roughly 20^0 with perpendicular to surface component of magnetization $M_{1,2}^z = \left| M_0 \sin\theta_{1,2} \right|$ being equal to 48 Gs. Normal to film magnetization is of a special interest, because it is a component, which determines Faraday rotation and, thus, is detected in our magnetooptical experiments.

This phase transition is demonstrated on Fig.9, where the perpendicular to plane component of energy most favorable state is depicted as a function of applied voltage.

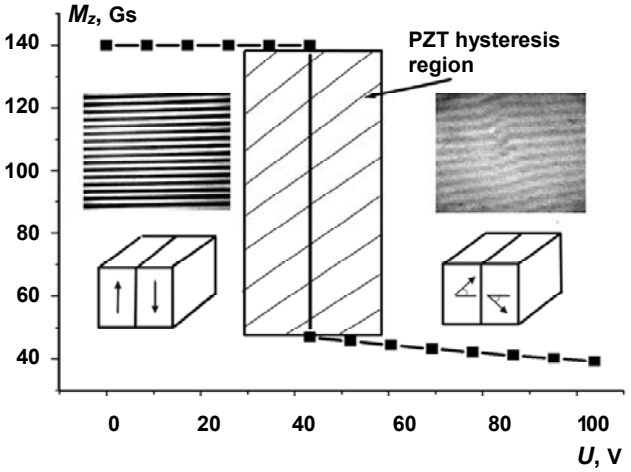

Fig. 9. Out-of-plane component of equilibrium magnetization vs. applied voltage at applied magnetic field H0=4Oe

Here $H_{U_1}^E(V)$ that was substituted in (1), had been calculated using (2) and actual experimental parameters.

In order to account for PZT hysteresys properties, we have expanded the phase transition point into finite-width region. Previous microwave experiments [12] put at our disposal directly measured $H_{U_1}^E(V)$ hysteresis curve, with average width of roughly 30 V. That value was straightly transferred onto Fig. 9.

Conclusions. Thus we have demonstrated the possibilities for control magnetization of YIG film and the intensity of light beam passed through the film by means of a sandwich structure, consists of ferrite-garnet film and piezoceramic PZT. This method is enough effective for energy saving and can be used in optoelectronics and spintronics [8] in spite of low-frequency range of its operation.

Thus, the electrically generated elastic stresses can shift magnetic state of the ferrite-garnet film sufficiently to control the characteristics of the light beam. Significant gains in efficiency of the described modulator can be achieved first of all by means of increasing magneto-optical efficiency and structural homogeneity of YIG film, optimization of treatment bias, and bandwidth of the optical beam. To test the above mentioned assumptions the diffraction experiments were performed with the magneto-optical Bi, Tm, Lu-containing ferrite-garnet films with $\phi_F \leq 1$deg/μm. A substantial increase (by two orders of magnitude) of the diffraction efficiency was observed and (particularly when resizing designs) increase in the frequency modulation. It is expected that composites consisting of piezoelectric and magneto-optical structures could find use in spintronic devices for electric and optic control of the nanosized integral elements.

1. *Bar'yakhtar V.G., Borodin V.A., Doroshev V.D.*, et al. Experimental and theoretical investigation of spin reorientation phase transitions in cubic ferromagnets and ferrimagnets in a magnetic field // Sov. Phys. JETP, vol. 47, No.2, (1978), p. 315–326. 2. *D'yachenko S.A., Kovalenko V.F., Tanygin B.N. and Tychko A.V.* Influence of the demagnetizing field on the structure of a Bloch wall in a (001) plate of a magnetically ordered cubic crystal // Phys. Solid State, Vol. 50, No. 1, pp. 32–42, 2008. 3. *Gurevich, A.G.; Melkov, G.A.;* Magnetization Oscillations and Waves; CRC Press: New York, NY, – 1996; pp. 147–336. 4. *Hasty T.E.* Ferromagnetic Resonance in Multidomain Thin Films // J. Appl. Phys,Vol. 35, No 5, p.1434 (1964). 5. *Hsu C.-J, Hockel J. L., and Carman G. P.* Magnetoelectric manipulation of domain wall configuration in thin film Ni/$[Pb(Mn_{1/3}Nb_{2/3})O_3]_{0.68}$-$[PbTiO_3]_{0.32}$ (001) heterostructure. Appl. Phys. Lett. 100, 092902. – 2012. 6. *Hubert A. and Schafer R.*, "Magnetic Domains", Springer-Verlag, Berlin 2009, 686 p. 1. *Kubota M., Tsukazaki A., Kagawa F.* Applied Physics Express 5. – 103002. – 2012. 8. *Parkes D.E., Cavill S.A., Hindmarch A.T., et al.* Magnetostrictive epitaxial thin films. Appl. Phys. Lett. 101, 072402. – 2012. 9. *Popov M.A., Zavislyak I.V.* Mechanism of Electric Frequency Tuning in Composite Resonators Based on Epitaxial Ferrite Films // Technical Physics Letters, 2012, Vol. 38, No. 9, pp. 865–868. 10. *Sohatsky V.* Electro-assisted magnetization switching in asymmetric spin valves. Solid State Phenomena (Trans Tech Publ.) – 2012 – V.190. – P.133–136. 11. *Zavislyak I.V. and Popov M.A.*, Microwave properties and applications of yttrium iron garnet (YIG) films: Current state of art and perspectives, in Yttrium: Compounds, Production and Applications, ed. by Bradley D. Volkerts (Nova Science Publishers, Inc., New York, 2011), p. 278. 10. *Яковлев Ю.М., Генделев С.Ш.* Монокристаллы ферритов в радиоэлектронике. М.: Сов. радио, 1975. 190 с.

Submitted on 10.07.12

Наукове видання

ВІСНИК

КИЇВСЬКОГО НАЦІОНАЛЬНОГО УНІВЕРСИТЕТУ ІМЕНІ ТАРАСА ШЕВЧЕНКА

РАДІОФІЗИКА ТА ЕЛЕКТРОНІКА

Випуск 18

Статті подано в авторській редакції

Оригінал-макет виготовлено Видавничо-поліграфічним центром "Київський університет"

Формат 60x84$^{1/16}$. Ум. друк. арк. 10,0. Наклад 300. Зам. № 212-6332.
Гарнітура Arial. Папір офсетний. Друк офсетний. Вид. № Рф2. Підписано до друку 18.01.13.

Видавець і виготовлювач
Видавничо-поліграфічний центр "Київський університет",
б-р Т. Шевченка, 14, м. Київ, 01601
☎ (38044) 239 32 22; (38044) 239 31 72; тел./факс (38044) 239 31 28
e-mail: vpc@univ.kiev.ua
http:vpc.univ.kiev.ua